Electronic Structure of Paramagnetic Transition Metal Complexes



Karrar Al-Ameed

Linacre College



A thesis submitted for the degree of

Doctor of Philosophy

DEPARTMENT OF CHEMISTRY

UNIVERSITY OF OXFORD

Trinity Term 2017

Electronic Structure of Paramagnetic Transition Metal Complexes

Karrar Al-Ameed, Linacre College

A Thesis Submitted for the Degree of Doctor of Philosophy
Department of Chemistry, University of Oxford
Trinity Term 2017

Abstract

This thesis presents a detailed study of a range of polynuclear paramagnetic transition metal complexes, using density functional theory (DFT) as a tool to probe their electronic properties. Four distinct projects are described in chapters 3-6, all of which are based on systems that have been synthesised in the laboratories of our collaborators, Professor Raphael Raptis at the Florida International University and Professor Yiannis Sanakis at the Democritus Institute in Athens. In Chapter 3, we address the question of redox-dependent spin transitions in triangular iron complexes. Experiments have shown that one-electron reduction of a pyrazolate-bridged Fe^{III}_3 cluster drives a transition from high- to low-spin configurations at all three metal centres. The corresponding carboxylate-bridged species, in contrast, remain high-spin in both redox states. The role of theory in this work was to investigate the origins of this cascade behaviour and the differences between carboxylate and pyrazolate systems. As a logical extension of this work, Chapter 4 turns to mixed-valence $[Fe_8]^{2-}$ clusters which contain six ferric and two ferrous centres ($Fe_6^{III}Fe^{II}_2$). Analysis of the energies of a range of broken-symmetry states suggests that inner-outer coupling interaction plays a dominant role in determining the ground state, favouring states where antiferromagnetic coupling is maximised. Following this, in Chapter 5, we discuss the site preferences in mixed Ni^{II}/Fe^{II} clusters. Experimental work by Raptopopolou, Sanakis and co-workers has yielded a range of nona-nuclear clusters with general formula Fe_xNi_{9-x}. The clusters have two distinct coordination sites – one 8-coordinate central position and 8 peripheral octahedral sites but X-ray crystallography is not able to distinguish the positions of Ni and Fe in the cluster. Mössbauer spectroscopy, however, suggests that the Fe centres preferentially occupy the central site while Ni goes to the peripheral positions. The distribution of metal ions

across sites of different coordination geometry is a fundamental problem in inorganic chemistry (the text-book example is the spinel family) and we show here that the ligand-field stabilisation energy available to Ni^{II} dominates the site distribution. Finally, in chapter 6 I discuss the magnetic coupling in a prismatic $Cu_6(\mu_3\text{-}OH)_2$ cluster made up of two $Cu_3(\mu_3\text{-}OH)$ triangles, bridged by pyrazolates and also a μ_6 fluoride ion. Similar clusters without the central fluoride have been studied before, and our aim here was to explore the role of the bridging fluoride in mediating magnetic exchange.

Three of these projects have been published in

1- Georgopouloua, A ,N ; Al-Ameed, K.; Boudalisa K, A ; Dimitrios F. Anagnostopoulosc, D, F; Psycharisa, V ; McGrady J, E; Sanakisa,Y; Raptopouloua, C, P., Site Preferences in Heterometallic Enneanuclear $[Fe_{9-x}Ni_x]$ Clusters, *Dalton Transactions* **2017** *46* (38), 12835-12844.

2- Govor, E. V.; Al-Ameed, K.; Chakraborty, I.; Coste, C. S.; Govor, O.; Sanakis, Y.; McGrady, J. E.; Raptis, R. G., A Redox-Induced Spin-State Cascade in a Mixed-Valent Fe_3(μ3-O) Triangle. *Angewandte Chemie International Edition* **2017**, *56* (2), 582-586.

3- Mathivathanan, L.; Al-Ameed, K.; Lazarou, K.; Travnicek, Z.; Sanakis, Y.; Herchel, R.; McGrady, J. E.; Raptis, R. G., A trigonal prismatic Cu-6-pyrazolato complex containing a μ_6-F ligand. *Dalton Transactions* **2015**, *44* (47), 20685-20691.

For my parents

Author's declaration

This thesis an account of work carried out by the author in the Department of Chemistry, University of Oxford, under supervision of Professor John E. McGrady. No part of this work has previously been submitted for a degree in this University or elsewhere. The work of other authors has been freely drawn and is duly acknowledged in the text. A list of references is given at the end of each chapter.

Karrar Al-Ameed

Oxford, 5th of October 2017

Acknowledgement

I would like express my gratitude to some special people who helped me to complete this work. However, it seems that these people cannot be properly acknowledged by merely few words. My supervisor Professor John E. McGrady comes at the top of the list. I must say how fortunate I was to work with such a great teacher, exemplary mentor and inspiring scientist. Thank you so much Professor, the past four years have been a wonderful experience!

My wonderful family, who have supported me ceaselessly and loved me unconditionally; I would like to express how blessed I am to have you in my life. I can never forget your love and encouragement. I am so grateful to have such wonderful parents. Also, I am extremely thankful to my beloved sister Raja Al-Ameed, for spending her hard-made savings on buying me my first laptop so that I could start my scientific journey in computational chemistry. My brother Hussein Al-Ameed; I was very privileged to have you on my side in this journey.

I also would like thank people who helped me to go through the big load of work presented in this dissertation. My colleagues James Lamb, Daniel Debrincat and Harry Morgan; I will always appreciate your help including proof reading of this work. Dr Vaida Arcisauskaite, Xiao Jin, and Andy Zeng, Mohammad AL-Nafee and Piao He; it was great working with you in the same team! I also I would like to thank to colleagues in Paton Group for many exciting coffee break conversations.

My second home, Linacre College; I would like to mention how lucky I was to belong to this amazing family. My wonderful friends there helped me to reduce the tremendous stress of the DPhil life. Particularly, I would like to thank my friends Dr. Nabanita Deb, Venus Tsang, Dr. Chelsea Robles, Beth Angris, Vladimer Olivero, Olga Tkachenko and Ashley Tsai as well as the *cool people* Dr Güneş Ünal, Daniel Debricant, Dr Neven Kraljevic, Ines Barreiros and Logan Hamilton. Oxford would never be a home without you!

I owe my sincere gratitude to Professor Muhsin Alibadi, for being a very inspiring teacher and a friend; my wonderful friends and colleagues back home, Dr Abbas Abo Nasria, Mr Laith Mahdi and Mr Hadi Al-Muhtaser; I would not be here without your support!

I would like to thank Dr. Jane Chanaa for being a wonderful advisor and tutor; Jackie Favarin at Linacre for all the help and advice; Emma Farrant for offering me accommodation close to the college library during my writing up year; and our

graduate studies administrator at Linacre Aga Borkowska for being so helpful and kind to me since the day I have applied to Oxford.

I also would like to express my gratitude to great people whom I have not had the chance to meet in person. Professor Peter Gill at the Austrialian National University, thanks a lot for enlightening distant communications since I have been an undergraduate student. I hope our paths will cross in the future. Dr Ekaterina Zueva at the Kazan State Technological University; many thanks for your fruitful scientific discussion regarding the spin Hamiltonian.

Dr Yannis Sanakis, many thanks for the scientific guidance regarding Mössbauer spectroscopy and your great Greek hospitality during my time in Democritos.

Finally, I would like to express my gratitude to my country and acknowledge The Higher Committee for Education Development (HCED) in Iraq for the financial support, which made this work possible.

.

Contents

1 Introduction 1

1.1 Magnetic Interactions 1

1.2 Polynuclear Compounds 2

1.3 References 9

2 A Brief Introduction to Computational Quantum Chemistry 12

2.1 Schrödinger Equation 12

2.2 Born–Oppenheimer Approximation 14

2.3 Hartree Product Wavefunctions 15

2.4 Slater Determinants 16

2.5 Hartree-Fock Theory 16

2.6 Basis Sets 20

2.6.1 Basis Function Types: Slater *vs.* Gaussian Orbital 21

2.7 The Self-consistent Field 23

2.8 Electron Correlation 24

2.9 Density Functional Theory 25

Density Functionals 27

2.9.1 Pure Density Functionals 28

2.9.2 Hybrid Density Functionals 30

2.9.3 Performance of OPBE Functional 31

2.10 Spin Contamination and Broken Symmetry States 32

2.11 The Coupling Between Paramagnetic Centres 34

2.12 Spin Hamiltonian 35

2.13 The Origin of the Exchange Interaction 37

2.14 Quantitative Models for The Exchange Interaction 38

2.14.1 Orthogonal Magnetic Orbitals Model (HTH) 38

2.14.2 The Kahn-Briat Model (KB) 40

2.14.3 DFT Broken Symmetry Models (DFT-BS) 41

2.15 References 44

3 A Redox-Induced Spin-State Cascade in a Mixed-Valent $Fe_3(\mu_3\text{-}O)$ Triangle 47

3.1 Introduction 48

3.1.1 Trinuclear Metal Complexes 48

3.1.2 Spin Crossover 51

3.2 Computational Details 53

3.3 Results and Discussion 56

3.3.1 Spin States 56

3.3.2 Geometrical Evidence 60

3.3.3 Energies and Functional Dependence 61

3.3.4 Analysis of the ^{57}Fe Mössbauer Spectroscopy 66

3.3.5 Infrared (IR) Spectroscopy 71

3.4 Conclusions 74

3.5 References 75

4 Electronic Structure of a Family of Octanuclear Iron-Oxo Clusters 79

4.1 Introduction 79

4.1.1 All ferric oxidation state, $[Fe_8]^0$ 81

4.1.2 One-electron mixed valence, $[Fe_8]^{1-}$ 83

4.1.3 Results: Electronic structure of the two-electron mixed valence, $[Fe_8]^{2-}$ 91

4.2 Conclusions 95

4.3 Computational Details 95

4.4 References 96

5 Analysis of Site Preferences in Heterometallic Enneanuclear [$Fe_{9-x}Ni_x$] Clusters..... 98

5.1 Introduction 99

5.1.1 Site Preferences of Transition Metal Ions 99

5.1.2 Homogenous and Heterogeneous Enneanuclear Clusters: a Summary of the Experimental Data. 101

5.2 Computational Details 104

5.3 Results and Discussion 106

5.3.1 Mössbauer Spectroscopy 106

5.3.2 Isodesmic Reaction Analysis 111

5.4 Conclusions 115

5.5 References 117

6 A Trigonal Prismatic Cu_6-pyrazolato Complex Containing a μ_6-F Ligand 120

6.1 Introduction to the Experimental Data 121

6.2 Computational Details 124

6.3 Discussion 125

6.4 Conclusions 129

6.5 Appendix: Spin Hamiltonian Code: 130

6.6 References 132

List of Figures

Figure 1.1: Schemic representation for (**a**) ferro- and (**b**) antiferromagnetic electronic configuration in a paramagnetic dimer. 2

Figure 1.2: Biologically important structures: (**a**) $Fe_4S_4(SCys)_4$ motif, where Cys refers to the amino acid, Cysteine; (**b**) Mn_4CaO_5 cubane in the oxygen evolving protein. 3

Figure 1.3: (**a**) $Mn_{12}O_{12}$ core of the first SMM complex. (**b**) Magnetic anistropy in a two-well diagram. 5

Figure 2.1: Components of the potential energy of a two-electron, two-nucleus system (following Szabo and Ostlund).[3] 13

Figure 2.2: Slater (dashed line) an Gaussian (solid line) functions 22

Figure 2.3: the main steps in an SCF loop 24

Figure 2.4: Potential energy diagram (PES) of hyrogen atom bond dissociation, calculated using the hybrid density functional B3LYP with 6-31G(d) basis sets. P represents Mulliken spin density on each atom. 34

Figure 2.5: the M-L-M exchange, (a) antiferromagnetic coupling in 180^{o} case. b) ferromagnetic coupling 90^{o} case. 38

Figure 2.6: Ground and triplet state wave function configuration of di-nuclear paramagnetic systems of S=1. 39

Figure 2.7: **(a)** Singlet and triplet spin state wavefunction components for paramagnetic centre with S=1/2 on each centre. (**b**) The relative energy of the three (ground state; GS, broken symmetry state; BS, high spin; HS) states. For such systems, BS here fall half way between the HS and the singlet. 42

Figure 3.1: structure of the oxo-bridged tri-iron complexes $[Fe_3(M_3\text{-}O)(LL)_6X_3]^z$: (**a**) LL = carboxylate and (**b**) LL = pyrazolate. The atoms' colour: red; oxygen, black; carbon, cyan; nitrogen; grey; a monodenate ligand X..... 48

Figure 3.2: the relationship between the observed isomer shift, Δ and the electron density at the nucleus, $P(0)$. The experimental isomer shift data is taken from reference [43], while we employed the model VWN-PW91/TZP to calculate electron density at the nucleus. 55

Figure 3.3: Possible configurations for the all-ferric spin state. (a) the antiferromagnetic (b) ferromagnetic states. The rows refer to the state of the three metal centres H means high spin while L means low spin. For example, the abbreviation HHL (High/High/Low) means two of the iron centres are high spin while the third ion is low spin. The fractional number under each structure refers to the M_S value. 57

FIGURE 3.4: POSSIBLE CONFIGURATIONS FOR THE MIXED VALENCE BROKEN SYMMETRY STATES: ADDING AN ALPHA (B) OR BETA(C) EXTRA ELECTRON GENERATES DIFFERENT MIXED VALENCE STATES FROM THE CORRESPONDING ALL-FERRIC ONES(A). THE FRACTIONAL NUMBER UNDER EACH STRUCTURE REFERS TO THE M_S VALUE..... 59

FIGURE 3.5: FUNCTIONAL DEPENDENCE SPIN CROSSOVER: THE RELATIVE ENERGIES OF THE HIGH AND LOW SPIN STATES OF THE ANTI-FERROMAGNETICALLY COUPLED STATES, OF THE ALL FERRIC (A) AND MIXED VALENCE (B) SPIN STATES. 62

FIGURE 3.6: (A) RELATIVE ENERGY OF ALL-FERRIC PYRAZOLATO COMPLEX $[Fe_3O(NCS)_3]^{3-}$ AGAINST NUMBER OF HIGH SPIN CENTRES OF THE FOURS SPIN-STATES (HHH;4/2, HHL,8/2, HLL; 4/2, LLL; 0/2). THE POINTS IN THE CURVE ARE CALCULATED USING GGA (BLYP OPBE), AND HYBRID/B3LYP FUNCTIONAL WITH 10%, 15% AND 20% OF HARTREE-FOCK EXCHANGE. (B) THE STRUCTURAL PARAMETERS AND THE SPIN CONFIGURATION ON EACH FE ION CALCULATED USING OPBE/TZP MODEL. (C) SCHEME OF BROKEN SYMMETRY STATES SHOWED THE DELOCALISATION OF THE ADDITIONAL ELECTRON ON Fe_2 DIMERS AND MULLIKAN SPIN DENSITIES ON EACH FE IONS GENERATED USING THE SAME MODEL. THE NUMBER BELOW THE X-AXIS REPRESENT THE M_S VALUES OF EACH SPIN STATE..... 63

FIGURE 3.7: RELATIVE ENERGY OF ALL-FERRIC CARBOXYLATE $[Fe_3O(OOCH)_6(NCS)_3]^{3-}$(AGAINST NUMBER OF HIGH SPIN CENTRES OF THE FOURS SPIN-STATES (HHH;4/2, HHL,8/2, HLL; 4/2, LLL; 0/2). THE POINTS IN THE CURVED CALCULATED USING GGA (BLYP AND OPBE), AND HYBRID/B3LYP FUNCTIONAL WITH 10%, 15% AND 20% OF HARTREE-FOCK EXCHANGE. THE NUMBER BELOW THE X-AXIS REPRESENT THE M_S VALUES OF EACH SPIN STATE. 65

FIGURE 3.8: SCHEMATIC REPRESENTATION OF MÖSSBAUER SPECTRUM FOR ATOM WITH NUCLEI SPIN $I = 3/2$, WHERE I, CORRESPONDS TO THE NUCLEAR SPIN, WHILE ΔE AND Δ REPRESENTS QUADRUPOLE SPLITTING, AND ISOMER SHIFT RESPECTIVELY..... 68

FIGURE 3.9: EXPERIMENTAL MÖSSBAUER SPECTRA AT 80 K: THE BLUE TO ALL FERRIC OXIDATION STATES WHILE THE RED PEAKS REFER TO MIXED-VALENT FORM; (**A**) $[Fe_3O(NCS)_3]^{\mathbf{2-/3-}}$, (**B**) $[Fe_3O(CN)_3]^{\mathbf{2-/3-}}$. 69

FIGURE 3.10: COMPUTED VIBRATIONAL SPECTRA AND THE SOME OF THEIR NORMAL MODES, OF C_{2V} TRI-IRON COMPLEXES: (**TOP**) $[Fe_3(M3{-}O)(OOCH)_6(NCS)_3]^{2-}$. (**BOTTOM**), $[Fe_3(M3{-}O)(NO_2{-}Pz)_6(NCS)_3]^{2-}$ ($[Fe_3O(NCS)_3]^{2-}$). 72

FIGURE 3.11: INFRARED SPECTRA OF $[Fe_3O(NCS)_3]^{z}$: ALL-FERRIC (Z = 2−, **BLUE**) AND MIXED VALENCE (Z = 3−, **RED**) SPECTRA: (**A**) THE COMPUTED SPECTRUM WITH DFT/OPBE THE SPECTRUM WITH DFT/OPBE CORRESPOND TO $S = 5/2$ AND $M_S = 0/2$ STATES RESPECTIVELY. **(B)** THE EXPERIMENTAL FTIR SPECTRUM. 73

FIGURE 4.1: STRUCTURE OF THE $[Fe_8(M3\text{-}O)_4(M\text{-}Pz)_{12}Cl_4]^{z}$ CLUSTER (LEFT) AND THE Fe_8O_4 CORE (RIGHT). 81

FIGURE 4.2: THE TWO TYPES OF COUPLING CONSTANTS 82

FIGURE 4.3: THE SPIN STATES USED TO CALCULATE THE EXCHANGE COUPLING CONSTANTS 83

FIGURE 4.4: EXAMPLE OF DOUBLE EXCHANGE MECHANISM: THE ELECTRON FROM Mn^{3+} SIMULTANEOUSLY REPLACED THE OXYGEN ELECTRON THAT TRANSFER TO THE LOW VALENCE CENTRE Mn^{4+}..... 84

FIGURE 4.5: FLOW DIAGRAM FOR SOME OF POSSIBLE SPIN STATES FOR $[Fe_8]^{1-}$: THE BLACK CIRCLES REPRESENT THE A-MAJORITY SPIN Fe^{III} AND THE WHITE CIRCLES B-MAJORITY Fe^{III} CENTRES..... 87

FIGURE 4.6: THE MAGNETIC MEASUREMENTS FOR $[Fe8]^{1-}$: (**A**) THE TEMPERATURE DEPENDENT. (**B**) THE FIELD DEPENDENT MAGNETISM. 90

FIGURE 4.7: SPIN STATE TREE DIAGRAM, THE BLACK CIRCLES REPRESENT SPIN 5-SPIN "UP" ELECTRONS, WHILE THE WHITE CIRCLES REPRESENT FIVE" DOWN" SPIN. 92

FIGURE 5.1: (A) SCHEMATIC REPRESENTATION OF THE ENNEA-NUCLEAR MOLECULAR CLUSTER (THE HYDROGENS ARE REMOVED FOR CLARITY), THE ATOMIC COLOURS ARE: GREEN; 6-COORDINATE METAL SITE, YELLOW; 8-COORDINATED METAL ION, RED; OXYGEN, BLUE; NITROGEN, GREY; CARBON. (B) SQUARE ANTIPRISM PYRAMIDAL METALLIC CORE. THE COORDINATION MODE OF $py_2CO_2^{2-}$ LIGAND, 12 OF THEM WITH 8 ACETATE LIGANDS SURROUNDING THE SQUARE ANTIPRISM PYRAMIDAL CORE TO MAKE THE STRUCTURE OF A. THE DASHED BONDS IMPLY WEEK LEGEND-METAL INTERACTIONS. 101

FIGURE 5.2: MÖSSBAUER SPECTRA OF 1-5 COMPOUNDS, THE BLACK COLOUR REFERS TO THE EXPERIMENTAL DATA WHILE THE RED AND BLUE COLOURED PEAKS CORRESPONDS TO THE THEORETICAL FITTED DATA, THE RED AND BLUE SIGNIFY 6- AND 8-COORDINATED FE RESPECTIVELY. THESE SPECTRA MEASURED BY SANAKIS ET AL AT DEMOKRITOS**.** 104

FIGURE 5.3: (LEFT) $FeNi_8$ CORE, THE BROWN AND BLUE COLOURED BALLS REPRESENTS NI (6-COORDINATE) AND FE (8-COORDINATE) IONS RESPECTIVELY, THE 4-FOLD AXIS GOES THROUGH THE DZ2 ORBITAL ON THE FE ION. (RIGHT) THE LIGAND FIELD SPLITTING PATTERN OF D ORBITAL ON THE CENTRAL 8-COORDINATE METAL ION. 109

FIGURE 5.4: RELATIVE ENERGIES DIAGRAMS. EACH OF THE POINTS ON THESE DIAGRAMS REPRESENTS THE FORMATION ENERGY OF $M@M_8 + 8M'@M'_8 \rightarrow 9M@M'_8$ REACTION, E.G THE $NiFe_8$ POINT IS THE ENERGY OF $Ni@Ni_8 + 8Fe@Fe_8 \rightarrow 9Ni@Fe_8$ REACTION. WHILE $Fe@Fe_8$ POINT REFERS TO THE HOMOGENOUS REACTION $Fe@Fe_8 + 8Fe@Fe_8 \rightarrow 9Fe@Fe_8$. NEGATIVE VALUES INDICATE THAT $M@M'_8$ IS MORE STABLE THAN THE STATISTICAL AVERAGE, WHILE POINTS ABOVE THE HORIZONTAL LINES INDICATE THAT $M@M'_8$ IS LESS. THE LINES COLOURS ARE: BLUE; NI/ZN, GREEN; NI/FE, RED; FE/ZN. 112

FIGURE 5.5: FORMATION REACTION ENERGIES OF $M@M_8 + 8M'@M'_8 \rightarrow 9M@M'_8$. NEGATIVE VALUES INDICATE THAT $M@M'_8$ IS MORE STABLE THAN THE STATISTICAL AVERAGE, WHILE POINTS ABOVE THE HORIZONTAL LINES INDICATE THAT $M@M'_8$ IS LESS. THE LINES COLOURS ARE: BLUE; NI/ZN, GREEN; NI/FE, RED; FE/ZN. 112

FIGURE 6.1: (A) MOLECULAR STRUCTURE OF $[Cu_6(OH)_2F]$. THE COLOURED BALLS ARE: COPPER; GREEN, NITROGEN; CYAN, OXYGEN; RED, FLOURIDE; PURPLE, CARBON; BLACK. (B) PRISMATIC Cu_6 CAGE. 121

FIGURE 6.2: THE MEASURED PLOTS OF THE TEMPERATURE-DEPENDENCE OF EFFECTIVE MAGNETIC MOMENTS: (**A**) $[Cu_6(OH)_2F]$ AND (**B**) $[Cu_6O_2]$. 123

FIGURE 6.3: EXCHANGE COUPLING CORRELATION SHOWING THE DEPENDENCE OF J_1 AND J_2 ON THE SEPARATION BETWEEN THE TWO O CENTRES FOR $[Cu_6(OH)_2F]$, AND THE CORRESPONDING SPECIES WHERE THE FLUORIDE ION HAS BEEN REMOVED ($[Cu_6(OH)_2]$). VERTICAL LINES SHOW THE OPTIMISED O–O SEPARATIONS WITH (5.14 Å) AND WITHOUT (4.48 Å) FLUORIDE ION. 126

FIGURE 6.4: MAGNETIC ORBITALS $dx2\text{-}y2$ OF THE METALS AND P ORBITALS OF THE OXYGEN ATOM. (A) AND (B) SHOW THE INTERACTION OF COPPER $dx2\text{-}y2$ ORBITAL WITH THE PX AND PY OF THE OXYGEN IN $[Cu_6O_2]$ AND $[Cu_6(OH)_6F]$ RESPECTIVELY, WHILE (C) AND (D) SHOWS THE CONTRIBUTIONS OF THE OXYGENIC PZ IN THE SAME INTERACTIONS. 127

FIGURE 6.5: (A) THE ENERGY LEVELS FOR SINGLE AND TWO COUPLED Cu^{II}_3 TRIANGLES. (B, C, D) THE COMPUTED MAGNETIC MOMENTS WITH THEIR CORRESPONDING EIGENVALUES SPECTRA. 129

FIGURE 6.6: THE MAIN STEPS OF THE SPIN HAMILTONIAN CODE. 132

List of Table

TABLE 3.1: SUMMARY OF EXPERIMENTAL M-L BOND LENGTHS (IN Å) BEFORE (ALL-FERRIC) AND AFTER (MIXED VALENCE) ONE-ELECTRON REDUCTION 51

TABLE 3.2: THE EXPERIMENTAL AND THEORETICAL STRUCTURAL PARAMETERS FOR TWO OXIDATION STATES, ALL-FERRIC AND MIXED-VALENT(MV), OF $[Fe_3O(NCS)_3]^z$ AND $[Fe_3O(CN)_3]^z$ COMPLEXES: THE COMPUTED SPIN STATE: ALL FERRIC; M_S = 5/2 AND MV;M_S = 0/2 FOR $[Fe_3O(NCS)_3]^z$, WHILE ALL FERRIC; M_S = 1/2 AND MV;M_S = 0/2, FOR $[Fe_3O(CN)_3]^z$ 60

TABLE 3.3: THE EXPERIMENTAL AND COMPUTED MÖSSBAUER PARAMETERS QUADRUPOLE SPLITTING, ΔEQ (MM/S), AND ISOMER SHIFT, Δ (MM/S), FOR THE ANTIFERROMAGNETIC STATES OF ALL-FERRIC AND MIXED-VALENCE OXIDATION STATES. 70

TABLE 4.1: RELATIVE ENERGIES AND MULLIKEN SPIN DENSITIES FOR SPIN STATES LISTED IN FIGURE 4.7 94

TABLE 5.1: THE COMPUTED MÖSSBAUER PARAMETERS: ISOMER SHIFT Δ, THE ELECTRIC FIELD GRADIENT COMPONENTS,(VXX, VZZ, VZZ), AND QUADRUPOLE SPLITTING (ΔE) FOR M'@M CLUSTERS, WHERE M' AND M REPRESENTS THE 8- AND 6-COORDINATED METALS RESPECTIVELY. THE MEASURED VALUES ARE PRESENTED BETWEEN THE PARENTHESIS. 106

TABLE 5.2: X-RAY FLUORESCENCE(XRF) AND MÖSSBAUER SPECTROSCOPY FOR **1-5** SAMPLES, THE FE/NI DETERMINED BY XRF. MÖSSBAUER PARAMETERS ISOMER SHIFT, QUADRUPOLE SPLITTING, ΔEQ AND THE HYPERFINE COUPLING CONSTANT $A_{(8)}/A_{(6)}$ REPRESENT THE AREA UNDER THE PEAK FOR 8-COORDINATES SITE. THE NUMBERS BETWEEN PARENTHESIS ARE THE ESTIMATED UNCERTAINTY OF THE LAST DIGIT. 110

List of Abbreviations

ADF	Amsterdam density functional
AF/F	antiferromagnetic/ferromagnetic
BO	Born-Oppenheimer
bpy	bipyridine
BS	broken symmetry
CAS	complete active space
CC	coupled cluster
CF	Coulson-Fisher
CI	configuration Interaction
COSMO	conductor-like screening model
Cys	cysteine
DFT	density functional theory
DZ	double zeta
EFG	electric field gradient
Et	ethyl
Fc	ferrocenium
GGA	generalised gradient approximation
GTO	Gaussian-type orbital
HDVV	Heisenberg, Dirac and Van Vleck
HF	Hartree-Fock
HOMO	highest occupied molecular orbital
HS	high spin
IR	infrared

KB	Kahn-Briat
KS	Kohn-Sham
LCAO	linear combination of atomic orbitals
LFSE	ligand field stabilisation energy
LS	low spin
LYP	Lee, Yang and Parr
Me	methyl
MO	molecular orbital
MP2	Møller–Plesset perturbation theory up to the second order
MV	mixed valence
NMO	natural magnetic orbital
OAc	acetate
OEC	oxygen evolving complex
pbym	2,2'-bipyrimidine
PES	potential energy surface
phen	1,10 phenanthroline
PPN	bis(triphenylphospine)iminium
py	pyridine
Pz	pyrazolate
SCO	spin crossover
SOMO	singly occupied molecular orbital
SQUID	superconducting quantum interference device
STO	Slater-type orbital
SV	split valence

SZ	single zeta
TFD	Thomas-Fermi-Dirac
TZ	triple zeta
TZ2P	triple zeta double polarised
TZP	triple zeta polarised
UHF	unrestricted Hartree-Fock
VDZ	valence double zeta
VWN	Vosko, Wilk and Nusair
XRF	X-ray fluorescence

1

1 Introduction

The central theme that links the four results chapters in this thesis is the presence of three or more transition metals that interact *via* super-exchange. What follows here is a very brief introduction to the general field. A detailed survey of the relevant literature to each of the individual topics is presented at the beginning of each of Chapters 3-6. Rapid advances in hardware and software engineering allow us to explore ever more sophisticated systems in quantum chemistry. Calculations can now be performed efficiently on a reasonable timescale for systems that were computationally inaccessible only a few years ago. Density functional theory has emerged as one of the most popular methods, providing a good trade off between computational cost and accuracy. All the calculations in this thesis are performed using the contemporary implementations of density functional theory.

1.1 Magnetic Interactions

The magnetic properties of chemical compounds can be broadly divided into two categories: *diamagnetic* and *paramagnetic*. Diamagnetic compounds have no net magnetic moment and are typically slightly repelled by a strong magnetic field. Paramagnetic compounds, on the other hand, are attracted to a magnetic field. Paramagnetic systems typically feature atoms or ions with *unpaired electrons* in their

outer shells (magnetic centres). In a compound with multiple paramagnetic (magnetic) centres (such as Fe^{II}, Cu^{II}, Ni^{II}), these centres can either be coupled ferromagnetically or antiferromagnetically. In ferromagnetic compounds, the magnetic centres have their magnetic dipole moment aligned in the same direction, while in antiferromagnetic compounds they are aligned opposite to each other.

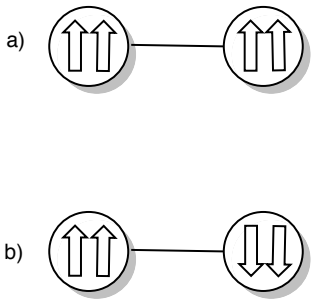


Figure 1.1: Schematic representation for (**a**) ferro- and (**b**) antiferromagnetic electronic configuration in a paramagnetic dimer.

1.2 Polynuclear Compounds

The properties of polynuclear paramagnetic transition metal complexes have been the focus of interest for decades due to their importance and applications in all aspects of life sciences. The biological importance of polynuclear complexes stems from their central role as active sites in metallobiomolecules.[1] For example, Fe-only enzymes that contain the cubane motif [4Fe-4S] (Figure 1.2a) are important in the redox chain reaction in nitrogenase while cubane shaped manganese-calcium clusters play a role in the oxygen evolving complex (OEC) responsible for water oxidation reactions in oxygenic photosynthesis (Figure 1.2b).[2] The OEC exists in all plants and algae and also in cyanobacteria, and its structure has inspired many researchers to work on mimicking manganese-calcium cubane.[3-8] Other examples include the Fe/(Mo, V, Fe)-based machineries that exist in nitrogen fixation[9] and purple acid

phosphatases[10]. Hetero-metallic Fe/Ni clusters are a particularly prominent sub-group, present in the active sites of several important proteins such as [NiFe] hydrogenases.[11-12]

a) b)

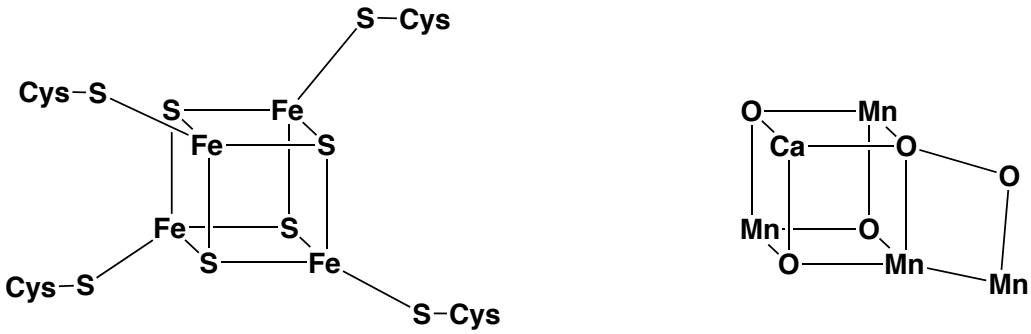


Figure 1.2: Biologically important structures: (**a**) $Fe_4S_4(SCys)_4$ motif, where Cys refers to the amino acid, Cysteine; (**b**) Mn_4CaO_5 cubane in the oxygen evolving protein.

Beyond their role in catalysis, some researchers have reported that iron-sulfur proteins can also act as magnetic bio-compasses that can help birds in navigation[13] by assembling inside a protein to form magnetic sensors (along with Cryptochromes that form a light activated spin pair) in the retina. Other researchers have argued that ferritin, the protein that stores iron as mineral iron oxides, is a potential candidate as a magnetic ion transfer in the cell membrane.[14-15]

Polynuclear clusters also have tremendous potential as building blocks for technical applications such as spintronic devices, molecular sensors and storage units. Much of this potential lies in their ability to co-exist in two or more distinct states, as for example in spin-crossover complexes.[16-17] Perhaps the most widely studied application comes in the field of single molecule magnets (SMMs). SMMs are molecules that show slow magnetic relaxation below a certain temperature known as the blocking temperature, although they share with bulk magnets the property that they

can be magnetised by an external field and can retain their magnetisation for a considerable amount of time after the applied field is removed. The manganese acetate complex $[Mn_{12}O_{12}(OOCCH_3)_{16}(H_2O)_4]$ (Figure 1.3a), is considered to be the archetype of single molecule magnets and shows remarkably slow relaxation even at very low temperatures (~ two months at ~2 K). The molecule features a cube of four Mn^{IV} connected via oxide bridges with a ring of eight peripheral Mn^{III} ions. The four core Mn^{IV} ions are coupled antiferromagnetically with the surrounding Mn^{III}, giving a ground state of $S = 10$ and zero-field splitting of $D = –0.46$ cm^{-1}. The zero-field splitting is an essential feature, imposing a barrier of 46 cm^{-1} between states of $M_S = \pm 10$ (Figure 1.3b). In the absence of an external field, the two M_S levels are equally populated but upon applying an external field along z, the $M_S = +S$ components will be lower and therefore more highly populated than $M_S = –S$. Relaxation occurs by re-populating $M_S = –S$ states but the barrier, $\Delta = |D|S^2 = 46$ cm^{-1}, is sufficient to retard this process such that the magnetism is retained. At first glance, it seems that a viable strategy to increase the barrier is to design a molecule with a higher ground-state S, and this has motivated a lot of synthetic chemists to build clusters with large number of paramagnetic metallic centres. However, a higher value of S in the ground state does not necessarily give a higher barrier because that value of D is also dependent on S, and in fact scales with $1/S^2$ [18-20]. Thus, a more important property is zero-field splitting, D, and its connection to structure.

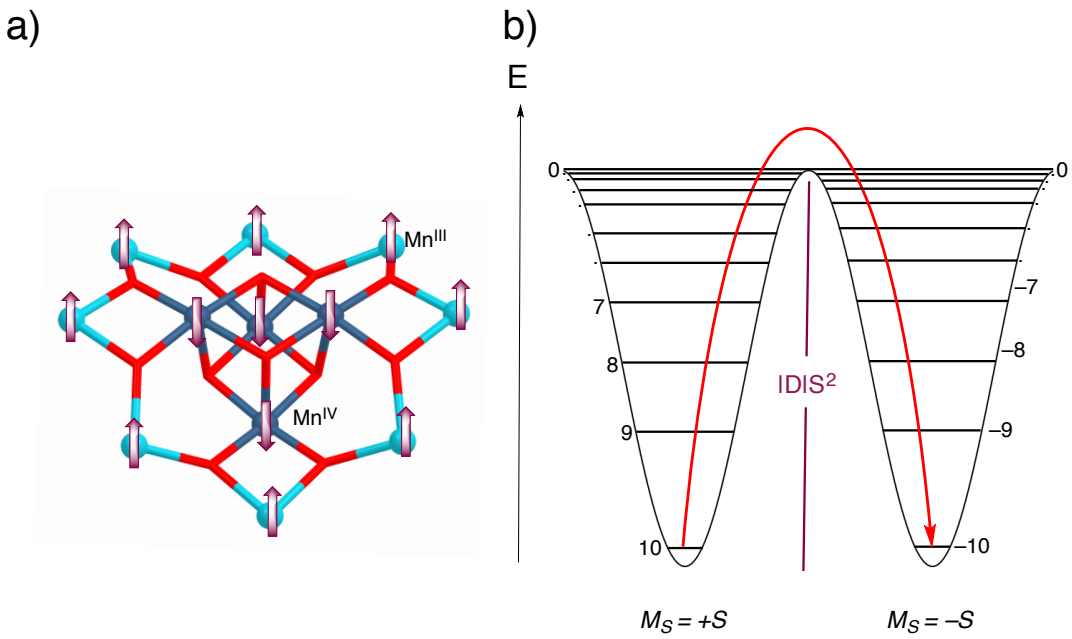


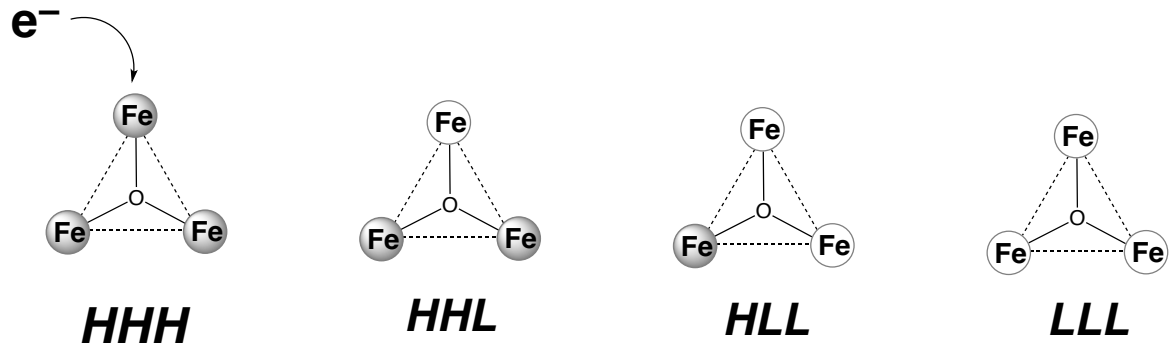
Figure 1.3: (**a**) $Mn_{12}O_{12}$ core of the first SMM complex. (**b**) Magnetic anisotropy in a two-well diagram.

Studies of electronic structure of these polynuclear compounds have been important contributors to the field and provide a greater understanding of the factors that control zero-field splitting parameters (D), thereby allowing synthetic chemists to engineer multinuclear complexes with high magnetic anisotropy. For example, distortions of triangular manganese(III) complexes,[21] imposed by shifting the central oxygen in Mn^{III}_3O motif ~0.3 Å above the M_3 plane and twisting the Mn^{III} coordination spheres relative to each other, results in changing ground spin state coupling from low spin antiferromagnetic to ferromagnetic with an $S = 6$. Altering the bridging anion is also an effective way of modifying the coupling and one of the common strategies to achieve ferromagnetic coupling between two metals is to replace O^{2-} bridges with N_2^{3-} bridge.[22]

Theoretical studies have been crucial to our understanding of the electronic structure of open-shell polynuclear clusters, and density functional theory in particular has been prominent as multi-configurational *ab initio* methods are only feasible for

relatively small systems. Chapter 2 presents a brief introduction to quantum chemistry, beginning with the fundamental concepts before moving to the basic *ab initio* approach, Hartree-Fock method. Density functional theory is then introduced and the chapter concludes with a summary of the broken symmetry methodologies that are particularly relevant to exchange-coupled systems.

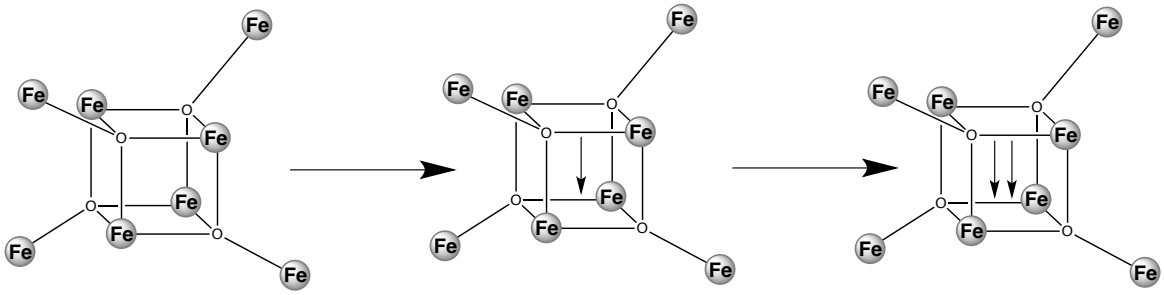
The four results chapters (3-6), describe four distinct problems related to the electronic structure of polynuclear compounds. All of these systems have been synthesised in the laboratories of our collaborators, Professor Raphael Raptis at the Florida International University and Professor Yiannis Sanakis at the Democritus Institute in Athens. In Chapter 3, we explore the electronic properties of triangular iron complexes. Our aim was to rationalise an unusual phenomenon: a one electron reduction process in a triangular all-ferric Fe^{III}_3 cluster drives a concerted transition from high-spin to low-spin configurations at all three metal centres (HHH→LLL). In marked contrast, a closely related carboxylate-bridged cluster remains high-spin at both redox levels.



The available experimental data (X-ray, Mössbauer and Infrared spectra) are all consistent with this interpretation. Our DFT results are, predictably, very dependent on the percentage of Hartree-Fock exchange in the functional – a higher percentage favours high-spin configurations. Notwithstanding this problem (a widely recognised

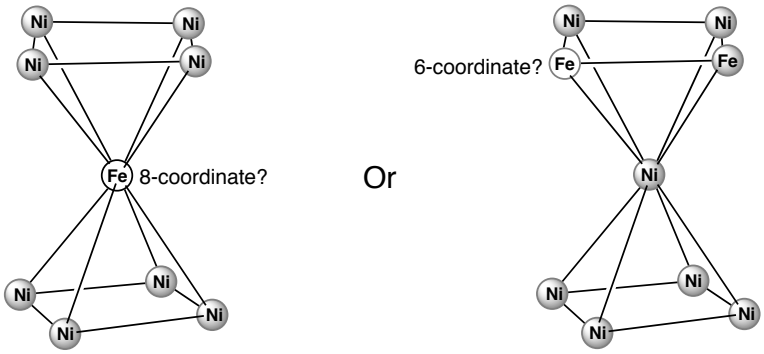
one in DFT), we can show that irrespective of the chosen functional, the intermediate states with mixed high- and low-spin centres are always unstable with respect to the all-high or all-low alternatives. Thus a transition at one centre will necessarily trigger a cascade wherein all three centres switch spin states. Furthermore, we were able to rationalise the reason behind this abrupt transition: in the mixed states steric strain accumulates at the high-spin sites, making further spin state transitions favourable. The work was published in *Angew. Chem. Int. Ed.*, **2017**.[23]

Chapter 4 then presents a detailed study of $[Fe_8]^z$ clusters, which are known in three oxidations states, z = 0, 1–, and 2–. The Fe_4O_4 cubane core shares many common features with magnetite, so we anticipate that this work may also shed light on the processes in the latter. The first two oxidation states have been studied previously in our group,[24-26] and this chapter extends the work to the dianionic cluster where Heisenberg exchange, double exchange and repulsions between the additional electrons all appear to play a role in determining the ground-state electronic structure.



In Chapter 5, we explore the site preference of the Fe^{II} and Ni^{II} ions in molecular clusters with generic formula Ni_xFe_{9-x}. Experimental work by Raptopopolou, Sanakis and co-workers has yielded a range of these clusters with widely varying x. There are two distinct coordination sites in these clusters - a single central 8-coordinate site and eight 6-coordinate sites around the periphery. Mössbauer spectroscopy suggests that

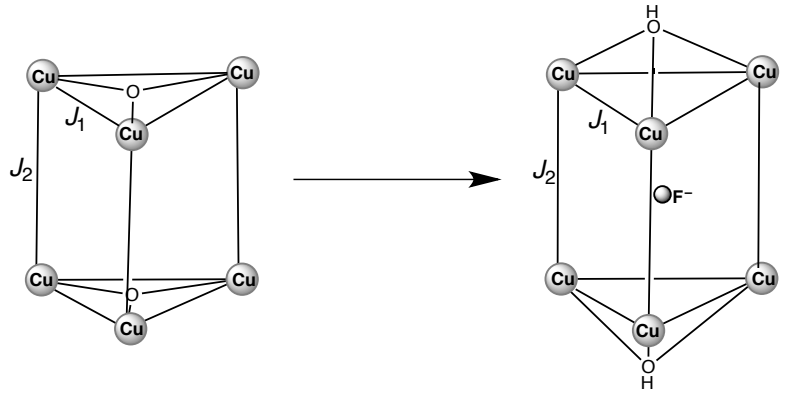
Fe preferentially occupies the central position, but X-ray data are not able to confirm this, as it is impossible to differentiate between Ni^{II} and Fe^{II} using this technique.



A direct analysis of different isomers with the same composition (e.g. $FeNi_8$ with Fe in the central and peripheral positions) has not been possible because of SCF convergence problems in low-symmetry isomers. However, a comparison of high-symmetry (D_4) structure with compositions $Fe@Fe_8$, $Fe@Ni_8$, $Ni@Fe_8$ and $Ni@Ni_8$ confirms that $Fe@Ni_8$ is more stable than a mixture of $Fe@Fe_8$ and $Ni@Ni_8$ while $Ni@Fe_8$ is less stable, consistent with the experimental observation. What this does not establish, however, is whether the distribution of metals over the two sites is driven by the preferences of Fe or the preferences of Ni. By replacing either Ni or Fe with Zn (with no ligand field stabilization energy), we show that the distribution of metals for the mixed Ni/Zn system is identical to that for Fe/Zn, while for the Fe/Zn system there is almost no site preference. From this we conclude that it is the Ni^{II} ion, with its strong ligand-field stabilization driven preference for octahedral coordination (i.e. the peripheral sites) that controls the distribution of ions. This work has been published in *Dalton Transactions* ***2017*** [27]

Finally, the work detailed in Chapter 6 has been published in *Dalton Transactions* **2015**,[28] Raptis and co-workers synthesised a Cu_6-cage containing an endohedral fluoride ion – this compound is very similar to a number of cages that the group have

studied previously[29], except for the presence of fluoride ion trapped inside the prismatic Cu_6-cage.



Our aim was to investigate the impact of the fluoride ion on the magnetic exchange interactions J_1 and J_2, within and between the copper triangles. The study concluded that while F^- ion has no effect on J_2, it does affect the values of J_1 by inflating the cluster and causing deviation of bond angles from their ideal values.

1.3 References

[1] C. S. Mullins and V. L. Pecoraro, *Coordination Chemistry Reviews* **2008**, *252*, 416-443.

[2] Y. Umena, K. Kawakami, J. R. Shen and N. Kamiya, *Nature* **2011**, *473*, 55-U65.

[3] L. Sun, *Science* **2015**, *348*, 635-636.

[4] U. Raucci, I. Ciofini, C. Adamo and N. Rega, *The Journal of Physical Chemistry Letters* **2016**, *7*, 5015-5021.

[5] C. H. Chen, C. X. Zhang, H. X. Dong and J. Q. Zhao, *Dalton Transactions* **2015**, *44*, 4431-4435.

[6] R. Chatterjee, S. Milikisiyants and K. V. Lakshmi, *Physical Chemistry Chemical Physics* **2012**, *14*, 7090-7097.

[7] J. Hogblom, P. H. Kenez, A. M. Styring, M. Abrahamsson, R. Lomoth, B. van Rotterdam, L. Sun, J. Park, J. Zheng, L. Hammarstrom, B. Akermark and S. Styring, *Journal of Inorganic Biochemistry* **2001**, *86*, 266-266.

[8] S. Styring, *Journal of Inorganic Biochemistry* **1999**, *74*, 53-53.

[9] Y. Hu and M. W. Ribbe, *Coordination Chemistry Reviews* **2011**, *255*, 1218-1224.

[10] G. Schenk, N. Mitic, G. R. Hanson and P. Comba, *Coordination Chemistry Reviews* **2013**, *257*, 473-482.

[11] Y. Montet, P. Amara, A. Volbeda, X. Vernede, E. C. Hatchikian, M. J. Field, M. Frey and J. C. FontecillaCamps, *Nature Structural Biology* **1997**, *4*, 523-526.

[12] A. Volbeda, M. H. Charon, C. Piras, E. C. Hatchikian, M. Frey and J. C. Fontecillacamps, *Nature* **1995**, *373*, 580-587.

[13] S. Y. Qin, H. Yin, C. L. Yang, Y. F. Dou, Z. M. Liu, P. Zhang, H. Yu, Y. L. Huang, J. Feng, J. F. Hao, J. Hao, L. Z. Deng, X. Y. Yan, X. L. Dong, Z. X. Zhao, T. J. Jiang, H. W. Wang, S. J. Luo and C. Xie, *Nature Materials* **2016**, *15*, 217-+.

[14] S. A. Stanley, J. Sauer, R. S. Kane, J. S. Dordick and J. M. Friedman, *Nature Medicine* **2015**, *21*, 92-98.

[15] M. A. Wheeler, C. J. Smith, M. Ottolini, B. S. Barker, A. M. Purohit, R. M. Grippo, R. P. Gaykema, A. J. Spano, M. P. Beenhakker, S. Kucenas, M. K. Patel, C. D. Deppmann and A. D. Guler, *Nature Neuroscience* **2016**, *19*, 756-761.

[16] O. Kahn, *Molecular magnetism*, VCH, New York, NY, **1993**, p. xvi, 380 p.

[17] G. Alcover-Fortuny, C. de Graaf and R. Caballol, *Physical Chemistry Chemical Physics* **2015**, *17*, 217-225.

[18] O. Waldmann, *Inorganic Chemistry* **2007**, *46*, 10035-10037.

[19] E. Ruiz, J. Cirera, J. Cano, S. Alvarez, C. Loose and J. Kortus, *Chemical Communications* **2008**, 52-54.

[20] F. Neese and D. A. Pantazis, *Faraday Discussions* **2011**, *148*, 229-238.

[21] T. C. Stamatatos, D. Foguet-Albiol, S.-C. Lee, C. C. Stoumpos, C. P. Raptopoulou, A. Terzis, W. Wernsdorfer, S. O. Hill, S. P. Perlepes and G. Christou, *Journal of the American Chemical Society* **2007**, *129*, 9484-9499.

[22] J. D. Rinehart, M. Fang, W. J. Evans and J. R. Long, *Journal of the American Chemical Society* **2011**, *133*, 14236-14239.

[23] E. V. Govor, K. Al-Ameed, I. Chakraborty, C. S. Coste, O. Govor, Y. Sanakis, J. E. McGrady and R. G. Raptis, *Angewandte Chemie International Edition* **2017**, *56*, 582-586.

[24] P. Baran, R. Boča, I. Chakraborty, J. Giapintzakis, R. Herchel, Q. Huang, J. E.McGrady, R. G. Raptis, Y. Sanakis and A. Simopoulos, *Inorganic Chemistry* **2008**, 47,645-655.

[25] E. M. Zueva, E. R. Ryabikh and S. A. Borshch, *Inorganic Chemistry* **2011**, *50*, 11143-11151.

[26] E. M. Zueva, R. Herchel, S. A. Borshch, E. V. Govor, W. M. C. Sameera, R. McDonald, J. Singleton, J. Krzystek, Z. Travnioek, Y. Sanakis, J. E. McGrady and R. G. Raptis, *Dalton Transactions* **2014**, *43*, 11269-11276.

[27] A. N. Georgopoulou, K. Al-Ameed, A. Boudalis, D. F. Anagnostopoulos, V. Psycharis, J. E. McGrady, Y. Sanakis and C. P. Raptopoulou, *Dalton Transactions* **2017**, *46*, 12835-12844.

[28] L. Mathivathanan, K. Al-Ameed, K. Lazarou, Z. Travnicek, Y. Sanakis, R. Herchel, J. E. McGrady and R. G. Raptis, *Dalton Transactions* **2015**, *44*, 20685-20691.

[29] E. M. Zueva, M. M. Petrova, R. Herchel, Z. Travnicek, R. G. Raptis, L. Mathivathanan and J. E. McGrady, *Dalton Transactions* **2009**, 5924-5932.

2

2 A Brief Introduction to Computational Quantum Chemistry

2.1 Schrödinger Equation

One can argue that quantum chemistry started with the discovery of the Schrödinger equation,[1] shortly after de Broglie proposed the wave-particle duality of electrons.[2] The non-relativistic form of the Schrödinger equation is a powerful tool for describing non-relativistic quantum mechanical systems. In its time-dependent form the Schrödinger describes the evolution of a quantum system over time:

$$i\hbar\frac{\partial}{\partial t}\Psi(t) = \hat{H}(t)\Psi(t) \qquad 2.1$$

However, if the Hamiltonian is itself independent of time, then

$$\Psi(\mathrm{t}) = \psi \mathrm{e}^{\frac{-\mathrm{iEt}}{\hbar}} \qquad 2.2$$

and the time-dependent equation reduces to its time-independent form

$$\hat{H}\psi = E\psi \qquad 2.3$$

where the wavefunction ψ is called a “stationary state”. The Hamiltonian operator $\hat{H}$ contains terms corresponding to all the contributions to the total energy of the system, kinetic ($\hat{T}$) and potential ($\hat{V}$).

$$\hat{H} = \hat{T} + \hat{\mathrm{V}} \qquad 2.4$$

For a system with M nuclei and N electrons, the two terms of the Hamiltonian can be expanded as follows (in atomic units), where the first and second terms represent the kinetic energy of the nuclei and electrons respectively.

$$\hat{T} = -\frac{1}{2}\sum_{A}^{M}\nabla_A^2 - \frac{1}{2}\sum_{i}^{N}\nabla_i^2 \qquad 2.5$$

$$\hat{V} = -\sum_{A}^{M}\sum_{i}^{N}\frac{Z_A}{|R_A - r_i|} + \sum_{A}^{M}\sum_{B>A}^{M}\frac{Z_A Z_B}{|R_A - R_B|} + \sum_{I}^{N}\sum_{j>i}^{N}\frac{1}{|r_i - r_j|} \qquad 2.6$$

The three components of the potential energy operator correspond to the nuclear-electron attraction, the nuclear-nuclear repulsion, and the electron-electron repulsion.

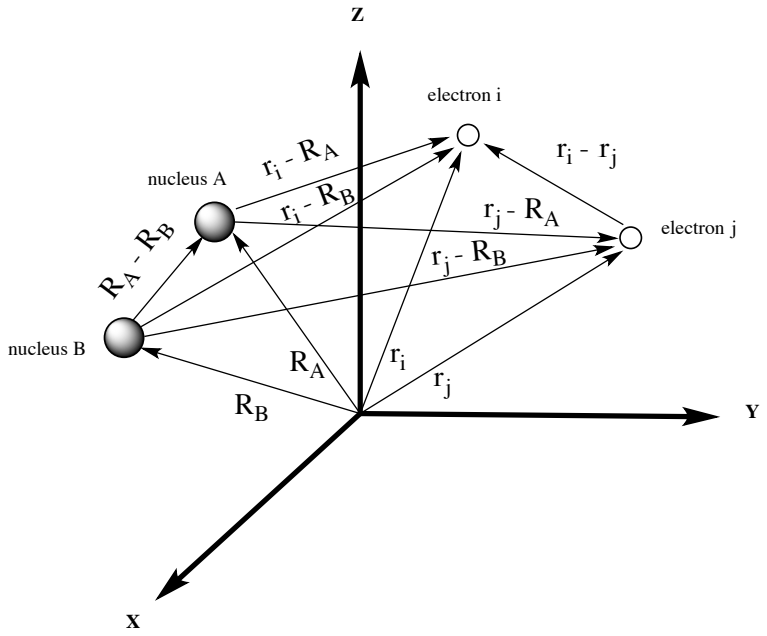


Figure 2.1: Components of the potential energy of a two-electron, two-nucleus system (following Szabo and Ostlund).[3]

In the two-nucleus two-electron system shown in Figure 2.1, expansion of the sums leads to an ten-term Hamiltonian:

$$\hat{H} = -\frac{1}{2}\nabla_A^2 - \frac{1}{2}\nabla_B^2 - \frac{1}{2}\nabla_i^2 - \frac{1}{2}\nabla_j^2 - \frac{Z_A}{|r_i - R_A|} - \frac{Z_A}{|r_j - R_A|} - \frac{Z_B}{|r_i - R_B|} - \frac{Z_B}{|r_j - R_B|} + \frac{Z_A Z_B}{|R_A - R_B|} + \frac{1}{|r_i - r_j|} \qquad 2.7$$

The Coulomb interaction between charged particles means that the Schrödinger equation can only be solved analytically for very simple systems – specifically those with only two interacting particles (*i.e.* the hydrogen and hydrogen-like systems). As a result, a number of approximations are typically applied to make solutions to the Schrödinger equation possible for more complex chemical systems.

2.2 Born–Oppenheimer Approximation

The Born-Oppenheimer (BO) approximation is perhaps the most important approximation made in electronic structure theory.[4] it states that because the nuclei have much larger masses than the electrons, one can consider the electrons to be moving in a constant electrostatic environment imposed by a fixed set of nuclei. In this approximation, the kinetic energy of the nuclei (the first two terms in the expansion for the two-nucleus two-electron system shown in the Equation 2. 7) is zero and the nuclear-nuclear repulsion (the 9th term) is constant and can be added at the end of the calculation to give the total energy. Removing these three terms leads to a simplified eigenvalue equation of the form.

$$\hat{H}_{elec}\Psi_{elec}(r_i; R_A) = E_{elec}(R_A)\Psi_{elec}(r_i; R_A) \qquad 2.\ 8$$

Where the notation $(r_i; R_A)$ signifies that the wavefunction depends parametrically on the nuclear coordinates. The constant nuclear-nuclear repulsion is added to the final electronic energy $E_{elec}(R_A)$ to recover the total energy for a fixed set of nuclear coordinates, E_{tot}.

$$E_{tot} = E_{elec} + \sum_{A}^{M}\sum_{B>A}^{M}\frac{Z_A Z_B}{|R_A - R_B|} \qquad 2.\ 9$$

A new wavefunction is defined when the system evolves to a new set of nuclear coordinates, and repeating the above calculations produces the potential energy surface(PES) which maps the total energy as a function of coordinates.

2.3 Hartree Product Wavefunctions

The BO approximation extends the exact solution of the Schrödinger equation to systems with an infinite number of (fixed) nuclei, but the restriction to a single electron remains: the interaction between the electrons renders the problem intractable.[5-7] In order to make progress, we can invoke the *orbital approximation*, which states that the complex multi-electron wavefunction can be written as a product of one-electron wavefunctions that describe the properties of each electron individually. In the absence of the electron-electron repulsion term in the Hamiltonian, these are exact eigenfunctions. The first work in this area was done by Hartree in 1928, who introduced the electron as an independent-particle that moves in the *average* electric field generated by the all electrons in the system.[8] The Hartree approximation states that total electronic wavefunction is a *product* of the orthonormal molecular orbitals, for a system with N electrons, the *Hartree product* is expressed as

$$\Psi_{HP} = \chi_1(\boldsymbol{x}_1)\chi_2(\boldsymbol{x}_2) \dots \chi_{N-1}(\boldsymbol{x}_{N-1})\chi_N(\boldsymbol{x}_N) \qquad 2.\ 10$$

where χ_i is a single electron wavefunction known as spin-orbital. Spin orbitals contain two components, the spatial part $\psi_i(\boldsymbol{r})$ and a spin component, α or β. The $\boldsymbol{x_i}$ in Equation 2. 10 therefore represent both the spatial coordinates of the particle, **r**, and its spin, s. The spin function is an eigenfunction of the operator $\hat{S}_z$, which has eigenvalues of $\hbar/2$ and $-\hbar/2$ for α and β spin respectively.

$$\chi_{\mathrm{i}} = \psi_{\mathrm{i}}(\mathbf{r})\alpha(\mathrm{s}) \text{ or } \psi_{\mathrm{i}}(\mathbf{r})\beta(\mathrm{s}) \qquad 2.\ 11$$

2.4 Slater Determinants

Whilst the Hartree product wavefunction provides a reasonable first approximation to the multi-electron wavefunction, it does not satisfy the Pauli exclusion principle which demands that the total wavefunction must be antisymmetric with respect to exchange of identical fermions (particles with half-integer spin). To overcome this problem, Fock, in 1930, modified the Hartree wavefunction[9] to impose antisymmetry by describing the wavefunction not as a single product, but rather as a linear combination of products with different signs. Subsequently, Slater[10] elegantly expressed this antisymmetric wavefunction by reformulating it as a determinant made up of molecular spin-orbitals. For a system with N electrons, the Slater wavefunction is:

$$\Psi_{SD} = \frac{1}{\sqrt{N!}} \begin{vmatrix} \chi_1(1) & \chi_2(1) & \cdots & \chi_N(1) \\ \chi_1(2) & \chi_2(2) & \dots & \chi_N(2) \\ \vdots & \vdots & \ddots & \vdots \\ \chi_1(N) & \chi_2(N) & \dots & \chi_N(N) \end{vmatrix} \qquad 2.12$$

Where the pre-factor is the normalization coefficient. In this expression, the columns represent the states (spin orbitals) while the rows identify each of the N particles. If two particles occupy the same orbital, two columns of the determinant will be identical and the determinant will be zero; such states therefore do not exist, as demanded by the Pauli principle.

2.5 Hartree-Fock Theory

The operation of the Born-Oppenheimer Hamiltonian on an appropriately antisymmetrised wavefunction of the Slater type, provides the basis of the Hartree-Fock (HF) method which is central to computational quantum chemistry. Although Hartree-Fock theory is not used (at least in its pure form) in this thesis, the machinery

involved is also used in density functional theory (DFT). It is therefore useful to develop Hartree-Fock theory first as a precursor to DFT.

With a Slater determinant constructed from a given set of orbitals, χ_i, the Hartree-Fock eigenvalues for the *i* electrons can be expressed as

$$\boldsymbol{F}_i^{HF}\chi_i = \epsilon_i\chi_i \qquad 2.\ 13$$

where ϵ_i is the eigenvalue of χ_i molecular orbital and $\boldsymbol{F}_i^{HF}$ is the Fock operator

$$\boldsymbol{F}_i^{HF} = -\frac{1}{2}\nabla_i^2 - \sum_{A}^{Nuclei}\frac{Z_A}{|R_A - r|} + v^{HF}(i) \qquad 2.\ 14$$

The Fock operator includes the kinetic energy term and also the interaction of the electron with each of the nuclei. The final term, v^{HF}, represents the average field due to the other electrons in the system. Roothan later proposed that the one-electron wavefunctions (χ_i above) could be expanded in terms of a linear combination of atomic basis functions, ϕ. The nature of these basis functions will be discussed in section 2.6

$$\chi_i = \sum_{\lambda} C_{\lambda_i}\phi_\lambda \qquad 2.\ 15$$

Minimising the total energy defined in Equation 2. 3 with respect to the coefficients leads to the Hartree-Fock-Roothaan equations in matrix form:

$$\mathbf{FC} = \mathbf{SC}\boldsymbol{\epsilon} \qquad 2.\ 16$$

where $\mathbf{C}$ is a λ x λ matrix containing the coefficients of the molecular orbitals. Non-trivial solutions of these equations are found when

$$\begin{vmatrix} F_{11} - ES_{11} & F_{12} - ES_{12} & \dots & F_{1N} - ES_{1N} \\ F_{21} - ES_{21} & F_{22} - ES_{22} & \dots & F_{2N} - ES_{2N} \\ \vdots & \vdots & \ddots & \vdots \\ F_{N1} - ES_{N1} & F_{N2} - ES_{N2} & \dots & F_{NN} - ES_{NN} \end{vmatrix} = 0 \qquad 2.\ 17$$

so diagonalization of this matrix yields the energies and coefficients of the molecular orbitals as the eigenvalues and eigenfunctions, respectively.

The elements of the overlap matrix, **S**, lie in the range $0 \leq S_{\mu\nu} \leq 1$. $S_{\mu\nu}$ is unity for the diagonal element (with a normalised basis) and less than one for off-diagonal elements.

$$S_{\mu\nu} = \int dr_i \, \phi_\mu(i)\phi_\nu(i) = \langle \mu | \nu \rangle \qquad 2.18$$

F is the Fock matrix, which can in turn be separated into two matrices, one containing the one-electron terms, $\boldsymbol{H}$, and the other the two-electron terms, the electron-electron repulsions, $\boldsymbol{G}$.

$$\boldsymbol{F} = \boldsymbol{H} + \boldsymbol{G} \qquad 2.19$$

The one-electron matrix $\boldsymbol{H}_{\boldsymbol{\mu\nu}}^{\boldsymbol{core}}$ contains both the kinetic energy term $\boldsymbol{T}_{\boldsymbol{\mu\nu}}$ and nuclear-electron attraction $\boldsymbol{V}_{\boldsymbol{\mu\nu}}$ elements**.** In Dirac notation, these take the form:

$$\boldsymbol{T}_{\boldsymbol{\mu\nu}} = \left\langle \mu \left| -\frac{1}{2}\nabla^2 \right| \nu \right\rangle \qquad 2.20$$

$$\boldsymbol{V}_{\boldsymbol{\mu\nu}} = \sum_{A}^{nuclei} \left\langle \mu \left| \frac{Z_A}{|R_A - r|} \right| \nu \right\rangle \qquad 2.21$$

The elements of the $\boldsymbol{G}$ matrix can be expressed as

$$\begin{aligned} \boldsymbol{G}_{\boldsymbol{\mu\nu}} &= \sum_{i}^{N/2} \sum_{\lambda\sigma} C_{\lambda_i} C_{\sigma i}^{*} \left[2(\mu\nu|\sigma\lambda) - (\mu\lambda|\sigma\nu) \right] \\ &= \sum_{\lambda\sigma} P_{\lambda\sigma} \left[(\mu\nu|\sigma\lambda) - \frac{1}{2}(\mu\lambda|\sigma\nu) \right] \end{aligned} \qquad 2.22$$

where the density matrix, **P** has been introduced. **P** is a product of coefficients, summed only over the occupied orbitals (of which there are N/2), and was first introduced by von Neumann[11] and Landau[12] independently, as a convenient way of collecting information about the spatial properties of the occupied orbitals.

$$P_{\lambda\sigma} = \sum_{i}^{occupied} C_{\lambda_i} C^*_{\sigma i} \qquad 2.\ 23$$

The so-called chemists notation is used for the two-electron integrals:

$$(\mu\nu|\lambda\sigma) = \int\int \phi_\mu(1)\,\phi_\nu(1)\frac{1}{r_{12}}\phi_\lambda(2)\,\phi_\sigma(2)\,dr_1 dr_2 \qquad 2.\ 24$$

The complete Fock matrix elements are therefore:

$$F_{\mu\nu} = \langle\mu|\hat{h}|\nu\rangle + \sum_{\lambda\sigma} P_{\lambda\sigma}\left[(\mu\nu|\lambda\sigma) - \frac{1}{2}(\mu\lambda|\nu\sigma)\right] \qquad 2.\ 25$$

Where the Dirac notation $\langle\mu|\hat{h}|\nu\rangle$ is used here to compact the traditional integral form $\int \phi_\mu(\hat{h}\phi_\nu)dr$. $\hat{h}$ represents the sum of the one electron operators, the kinetic and the potential energies.

Following diagonalization of the secular matrix to get the eigenvalues, the total Hartree-Fock energy can be expressed as:

$$E_{HF} = \sum_i \langle\chi_i|\hat{h}_i|\chi_i\rangle + \frac{1}{2}\sum_{i,j}\left[(\chi_i\chi_i|\chi_j\chi_j) - (\chi_i\chi_j|\chi_j\chi_i)\right] \qquad 2.\ 26$$

$$= \sum_i \langle\chi_i|\hat{h}_i|\chi_i\rangle + \frac{1}{2}\sum_{i,j}[J - K] \qquad 2.\ 27$$

The electron-electron repulsions terms separate into two distinct types. The coulomb repulsion term, *J*, represents the classical repulsion between the probability density of electron 1 in χ_i and electron 2 in χ_j.

$$(\chi_i\chi_i|\chi_j\chi_j) = \int\int \chi_i(1)\,\chi_i(1)\frac{1}{r_{12}}\chi_j(2)\,\chi_j(2)dr_1 dr_2 \qquad 2.\ 28$$

The second term, the exchange integral, *K*, has no classical analogue.

$$(\chi_i\chi_j|\chi_j\chi_i) = \int\int \chi_i(1)\,\chi_j(1)\frac{1}{r_{12}}\chi_j(2)\,\chi_i(2)dr_1 dr_2 \qquad 2.\ 29$$

The exchange term is purely quantum mechanical, and is a result of the Pauli principle requirement (which in turn enforces the use of an antisymmetric Slater determinant). The exchange term is non-zero only when electrons have the same spin and because it enters the energy expression with a negative sign, its effect is to reduce the repulsion between parallel-spin electrons, creating what is known as the Fermi hole. The exchange integral plays a particularly important role in cancelling so-called self-interaction. The summation of the Coloumb terms over all *i,j* includes the repulsion of an electron by itself, a clearly non-physical interaction. However, when $i = j$, $J = K$, and therefore the exchange terms cancels exactly the spurious Coulomb term. In density functional theory this cancellation is not necessarily exact, leading to the so-called self-interaction error.

2.6 Basis Sets

Up to this point, we have noted that the orbitals can in principle be expanded in terms of a basis set, ϕ_λ.

$$\chi_i = \sum_\lambda C_{\lambda_i} \phi_\lambda$$

The Hartree-Fock limit is reached with an infinitely large basis set, but in practice this is clearly impractical. Instead, finite basis sets are used, involving a trade-off between accuracy and time: a bigger basis set means higher accuracy and *vice versa*. The computational effort of evaluating the two electron integrals in *ab initio* theories increases as N^4, where N is number of basis functions. Therefore, the common practice is to use the smallest possible basis set compatible with acceptable accuracy.

The efforts of the basis sets developers therefore focus on developing finite basis sets that can approach the basis set limit as closely as possible.[13-14]

2.6.1 Basis Function Types: Slater *vs.* Gaussian Orbital

In molecular electronic structure calculations, there are two commonly used types of basis function: Slater-type Orbitals (STO) and Gaussian-type orbitals (GTO). STOs are in principle a good choice because they have the same form as the hydrogenic solutions of the Schrödinger equation, with an exponential dependence on *r*.

$$\phi_{\zeta,n,l,m}(r,\theta,\phi) = NY_{l,m}(\theta,\phi)r^{n-1}e^{-\zeta r} \qquad 2.30$$

N and $Y_{l,m}$ are normalization factors and spherical harmonic functions respectively. Whereas n,l,m are the atomic quantum numbers. Gaussian type orbitals (GTOs), first introduced as an alternative to STOs by Boys in 1950[15], have a different mathematical expression where the exponent contains r^2 instead of r:

$$\phi_{\zeta,n,l,m}(r,\theta,\phi) = NY_{l,m}(\theta,\phi)r^{n-1}e^{-\zeta r^2} \qquad 2.31$$

A single GTO is therefore a poorer match to an atomic orbital than the corresponding STO: it has zero slope at the nucleus while an STO has a more relatistic “cusp”, and the GTO decays more rapidly to zero at large distances from the nucleus than an equivalent STO. In order to allow a GTO basis set to approach the same accuracy as an STO equivalent, a linear combination of a number of GTOs is typically used to model a single STO. However, GTOs have one significant advantage over STOs in that the product of two GTOs is another GTO located at some point between the two original orbitals. This Gaussian product theorem has profound implications, because it makes the calculation of the two-electron integrals in the Fock matrix tractable. The introduction of GTOs was therefore pivotal to the development of *ab initio* methods based on Hartree-Fock theory, where these two-electron integrals are needed. In

density functional theory, the explicit computation of these integrals is avoided through the introduction of the exchange-correlation potential, and so GTOs have no obvious advantage over the STO alternative. Codes like Gaussian, which were developed to perform *ab initio* calculations, have retained Gaussian basis functions for density functional theory but some codes developed specifically for DFT adopt STOs instead. This is the case with the ADF code, which is the primary tool used in this thesis. The discussion of basis set types below therefore refers primarily to STOs, although similar principles apply for GTOs.

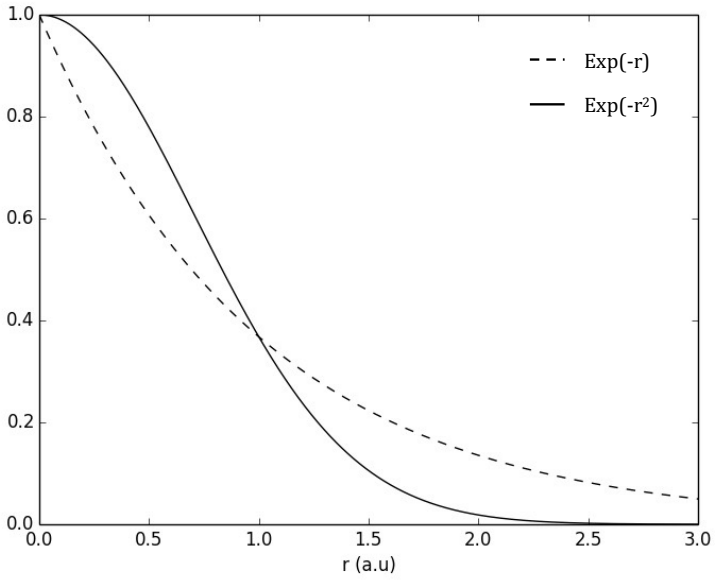


Figure 2.2: Slater (dashed line) an Gaussian (solid line) functions

A minimal or *Single Zeta (*SZ*)* basis set employs a single s-function to represent the 1s orbital of hydrogen and helium and five functions for a fist-row atom: two s-functions (for 1s and 2s orbitals) one set of p-function (p_x, p_y, p_z). *Double and Triple Zeta (DZ)* basis sets provide two and three basis functions for each atomic orbital, which provides greater flexibility and therefore a better description of bonding. In *Split valence* (SV) *or valence double zeta* (VDZ) basis sets only the basis functions for the valence orbitals are split (for example, 2s and 2p for the carbon). Adding higher

angular momentum functions allows for orbital polarization. For example, to polarise a valence orbital with angular momentum l requires a basis function with angular momentum $l + 1$: p functions polarise s orbital, d functions polarise p, etc. In ADF, polarised basis sets are identified by the P letter at the end of their name, for example DZP stands for *double zeta polarized* basis sets. Similarly, *triple zeta polarised* is denoted TZP and double polarised basis sets TZ2P.

2.7 The Self-consistent Field

The solution of the Hartree-Fock-Roothaan equations yields the coefficients of the individual orbitals as the eigenfunctions of the secular matrix (Equation 2. 17). However these same coefficients were required earlier in the process, in order to calculate the elements of the Fock matrix – specifically the components of G in Equation 2. 19. To escape from this circular problem, we adopt an iterative process known as the self-consistent field approach summarised in Figure 2.3.

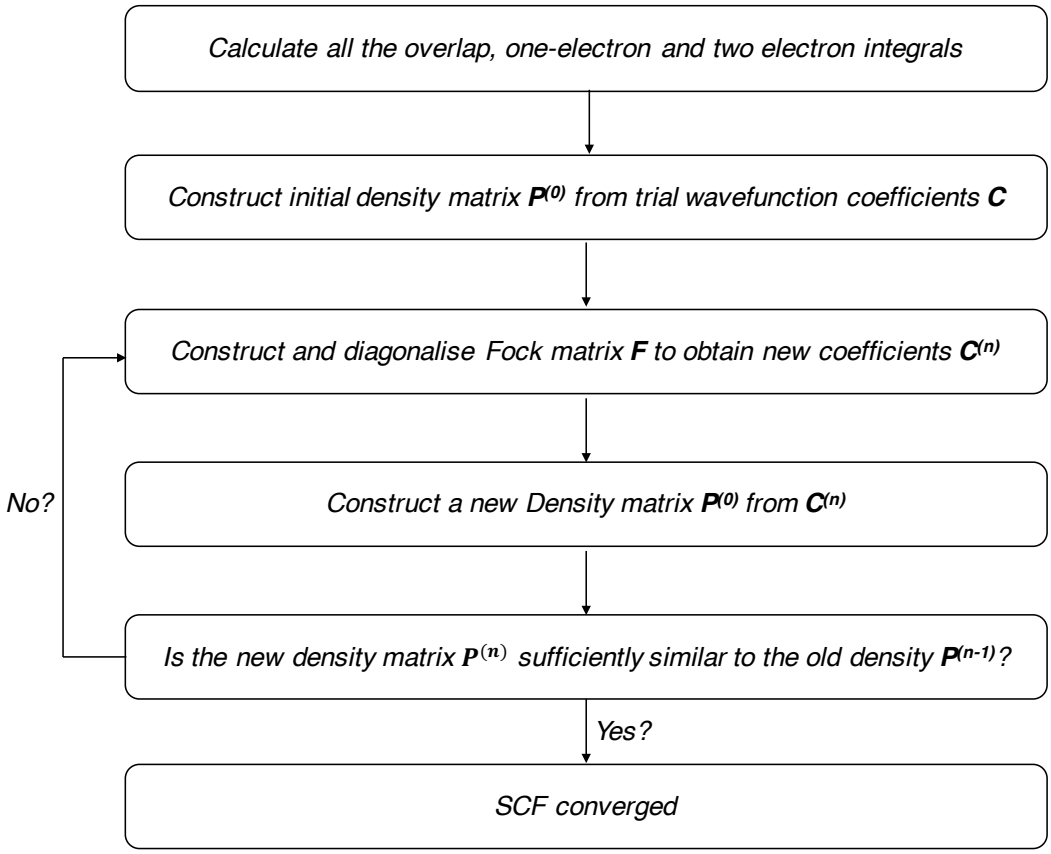


Figure 2.3: the main steps in an SCF loop

The essence of the approach is to make a suitable guess at the coefficients and hence to the density matrix, and use that to compute a first approximation to the Fock matrix. This can then be diagonalised to give an improved density matrix (the eigenfunctions) and the process continued iteratively until successive cycles yield density matrices that are identical to within a pre-defined error. This self-consistent approach is central to most electronic structure methods, including density functional theory that will be used in most of this thesis.

2.8 Electron Correlation

The interaction between electrons in the HF method is based on the interaction of one electron with the average field due to the others rather than their instantaneous positions. Put another way, if we describe the wavefunction of He as $1s^2$, the

implication of this is that the spatial wavefunction is the same for both electrons. The most probable outcome of an experiment that located both electrons simultaneously would therefore place the two electrons in exactly the same place, a clearly non-physical situation. In reality, situations where the two electrons are very close to each other will be avoided, and so the HF scheme overestimates the repulsion by about 1%. The magnitude of this correlation is defined as the difference between the exact and HF energies of the system.

$$E_{corr} = E_{exact} - E_{HF} \qquad 2.32$$

This kind of correlation is known as *coulomb correlation* and, unlike the exchange correlation discussed earlier, is most important for electrons in the same orbital (and therefore necessarily of opposite spin). Electron correlation can be further classified into two categories: *Dynamic* and *non-dynamic (static)*. Dynamic correlation is related to the motion of one electron relative to the other, normally between electrons in the same spatial orbital as in the He ground state described above. Static correlation, in contrast, relates to the inadequacy of single-determinant methods in describing the states arising from multiple degenerate configurations. For example, the H_2 molecule near the dissociation limit has two degenerate electronic configurations ($|\uparrow \ldots \downarrow\rangle + |\downarrow \ldots \uparrow\rangle$), and so two Slater determinants are required to describe the ground state. Static correlation is one of the main motivations to develop post-HF techniques such as Configuration Interaction (CI), Coupled Cluster (CC) and Complete Active Space (CAS) methodologies

2.9 Density Functional Theory

Density functional theory, DFT, is the most common electronic structure method used in modern-day quantum chemistry, certainly for inorganic systems. The density

depends only on 3 spatial coordinates regardless of the number of electrons while an N-electron wavefunction depends on 3N variables, so making the density the fundamental variable rather than the wavefunction has obvious advantages. In 1965 Hohenberg and Kohn established that the energy of the ground state of a system is a unique functional of its electron density ρ[16]. *i.e* the ground state density can be used to construct the Hamiltonian operator where the ground state energy of the system can be determined.

$$\rho_o = \{N, Z_A, R_A\} \rightarrow \widehat{H} \rightarrow \Psi_o \rightarrow E_o \qquad 2.33$$

The total energy can be divided into three functional components, each of which is a functional of ρ.

$$E[\rho] = E_{Ne}[\rho] + T[\rho] + E_{ee}[\rho] \qquad 2.34$$

$$\boldsymbol{F^{HK}}[\rho] = T[\rho] + E_{ee}[\rho] \qquad 2.35$$

$\boldsymbol{F^{HK}}$ is the holy grail of density functional theory, knowing this functional means that Schrodinger equation can be solved exactly for all kind of systems. Unfortunately, despite extensive efforts over the past 50 years, the exact functional that describes the relationship between energy and density is yet to be discovered. Early attempts to describe all the components of the energy using only the electron density were frustrated by difficulties in the exact computation of the kinetic energy term, but Kohn and Sham[24] then suggesting using a set of "fictional" orbitals to construct the density, and then using the orbitals themselves to calculate the troublesome kinetic energy terms. By introducing a set of one-electron Kohn-Sham orbitals, the same self-consistent machinery applied in Hartree-Fock theory can be used, leading to a set pseudoeigenvalue equation:[14]

$$\boldsymbol{F}_i^{KS}\chi_i = \epsilon_i\chi_i \qquad 2.\ 36$$

The Kohn-Sham one-electron operator $\boldsymbol{F}_i^{KS}$ is very similar in structure to the one-electron Fock operator $\boldsymbol{F}_i^{HF}$ used in HF theory, except the potential v_{XC} replaces the exact Fock exchange potential v^{F30}.

$$\boldsymbol{F}_i^{KS} = -\frac{1}{2}\nabla_i^2 - \sum_k^{nuclei} \frac{Z_k}{|\boldsymbol{r}_i - \boldsymbol{r}_k|} + \int \frac{\rho(\boldsymbol{r}')}{|\boldsymbol{r}_i - \boldsymbol{r}_k|} d\boldsymbol{r}' + v_{XC} \qquad 2.\ 37$$

This Kohn-Sham approach paved the way for modern density functional theory, where the focus is now on developing the functional form of v_{XC} , which describes the non-coulomb parts of the electron-electron repulsion term but also a correction to the kinetic energy to account for the fact that the Kohn-Sham approach introduces fictitious orbitals. The potential v_{XC} is the functional derivative of E_{XC} with respect to density.

$$v_{XC} = \frac{\delta E_{XC}}{\delta \rho} \qquad 2.\ 38$$

Density Functionals

The energy of any chemical system can be partitioned into five basic components

$$E = E_T + E_V + E_J + E_X + E_C \qquad 2.\ 39$$

corresponding to the kinetic, electron-nuclei attraction, electron-electron repulsion, exchange, and correlation energies respectively. As noted above, the kinetic energy term is computed using the Kohn-Sham orbitals, from which the density can be generated. The interaction of the electron density with the static nuclei can be computed rather trivially:

$$E_V = -\sum_a^m Z_a \int \frac{\rho(\boldsymbol{r})}{|\boldsymbol{r} - \boldsymbol{R}_a|} d\boldsymbol{r} \qquad 2.40$$

as can the classical coulomb interaction of a charge cloud with itself:

$$E_J = \frac{1}{2} \int \int \frac{\rho(\boldsymbol{r}_1)\rho(\boldsymbol{r}_2)}{|\boldsymbol{r}_1 - r_2|} d\boldsymbol{r}_1 d\boldsymbol{r}_2 \qquad 2.41$$

What remains are the exchange and correlation terms, whose functional form is not known. The exchange part is the larger of these, and any approximate expression for it must fulfill two roles: (1) reduce the repulsion between parallel spin electrons and (2) cancel the spurious self-repulsion that is present in Equation 2. 41.[17] Finding a functional with the appropriate mathematical form to achieve this across a range of bond types remains the holy grail of density functional theory. There are several approaches to this problem but in this thesis, I will use two distinct classes: pure gradient-corrected functionals (GGAs) and hybrid functionals.

2.9.1 Pure Density Functionals

In 1927, only a year after the birth of Schrodinger equation, Thomas and Fermi proposed[18] that the total energy could be calculated approximately using only the electron density (only 40 years later did Hohenberg and Kohn show that this was in principle exact and not merely an approximation). They proposed that the total energy could be expressed in the following way

$$E^{TF} = E_T^{TF27} + E_V + E_J \qquad 2.42$$

where the exchange and correlation components are neglected entirely. The kinetic energy was evaluated using the so-called 'jellium' model, or uniform electron gas, an

ideal system of N electrons uniformly distributed in a box along with positive charges to neutralise the system.

$$E_T^{TF27} = \frac{3}{10}(3\pi^2)^{2/3} \int \rho_\alpha^{\frac{5}{3}}(\boldsymbol{r})\, d\boldsymbol{r} \qquad 2.43$$

However, the energy calculated is significantly lower than the exact kinetic energy.

In 1930, based on the same jellium model, Dirac proposed a functional form for the exchange term and later introduced an empirical constant α (which is typically close to $\frac{2}{3}$) leading to the earliest $X\alpha$ approximation to exchange.

$$E_X^{D30} = -\frac{9\alpha}{8}\left(\frac{3}{\pi}\right)^{1/3} \int \rho_\alpha^{\frac{4}{3}}(\boldsymbol{r})\, d\boldsymbol{r} \qquad 2.44$$

The total energy for this Thomas-Fermi-Dirac(TFD) model based purely on density is:

$$E^{TFD} = E_T^{TF27} + E_V + E_J + E_X^{D30} \qquad 2.45$$

The energy calculated using the TF and TFD models suffered from substantial errors that made them essentially useless for accurate calculations. In 1951, Slater proposed that the approximate Dirac exchange functional (DFT based) could be used in place of the exchange term in the Fock operator, leading to a substantial reduction in the computational expense.

$$E^{HFS} = E_T^{H30} + E_V + E_J + E_X^{D30} \qquad 2.46$$

The Dirac exchange functional E_X^{D30} underestimates the exchange energy compared to E_X^{F30}, which means that the exact cancellation of the self-interaction error that is a feature of HF theory is no longer exact. A correlation functional can also be developed based on the properties of the uniform electron gas, as implemented by Vosko, Wilk and Nusair (VWN) in 1980[19].

$$E^{LDA} = E_T^{H30} + E_V + E_J + E_X^{D30} + E_C^{VWN} \qquad 2.47$$

The density functionals developed so far depend only on the density at a given point, but improvement can be made, particularly in molecular systems, by also taking into account the gradient of the density (the so-called Generalised Gradient Approximation or GGA). One of the most popular GGA models is the BLYP functional which incorporates gradient corrections to the exchange functional developed by Beck in 1988[20] and to the correlation part by Lee, Yang and Parr (LYP)[21]

$$E^{BLYP} = E_T^{H30} + E_V + E_J + E_X^{B88} + E_C^{LYP} \qquad 2.48$$

This theory gives a generally good description of many chemical and physical properties but fails in some cases, for example in the calculation of isomerization energies and the barrier heights. [17]

2.9.2 Hybrid Density Functionals

To improve the accuracy of XC functionals in KS methods, Beck suggested mixing a fraction of the exact HF exchange functional E_X^{F30} (wavefunction based) into the DFT exchange functional E_X^{B88}. Specifically, he proposed a hybrid model with three empirical parameters a_0, a_X and a_C which control the amount of exchange for each functional. The earliest hybrid model, B3PW91, is:

$$E^{B3PW91} = E_T^{H28} + E_V + E_J + (1 - a_0)E_X^{D30} + a_0 E_X^{F30} + a_x \Delta E_X^{B88} + E_C^{VWN} + a_c \Delta E_C^{PW91} \qquad 2.49$$

with optimised value for these parameters are: a_0= 0.20, a_X= 0.72, a_C= 0.81 (the number 3 in B3PW91 recognises the presence of three parameters). Later , Stephen *et al*[22] replaced the PW91 correlation functional with LYP to generate the B3LYP functional which has become the most popular hybrid method by far due to its

remarkable accuracy cross a wide range of chemical problems. The B3LYP XC functional energy expressed as

$$E_{XC}^{B3LYP} = (1 - a_0)E_X^{D30} + a_0 E_X^{F30} + a_x \Delta E_X^{B88} + (1 - a_c)E_C^{VWN} + a_c E_C^{LYP} \qquad 1.50$$

The three parameters have the same value as in B3PW91. B3LYP contains 20% of HF exchange (a_0= 0.2) but the most accurate value may differ in specific situations. For example in the context of spin crossover complexes that are of interest in Chapter 3, Reiher has argued[23] that setting the amount of HF exchange to 15% ($a_0 = 0.15$) produces better agreement with experiment, particularly for the first row transition metal complexes. This different parameterization is implemented in his B3LYP* functional. There are now many different hybrid functionals that contain different percentages of HF exchange such as "half-and-half" functionals (BHandH AND BHandHLYP) proposed by Becke that contains 50% of this exchange.[24] It is worth noting here that hybrid functionals require the computation of the exact Hartree-Fock exchange, and therefore of the two-electron integrals noted previously. Therefore GTO basis sets regain their significant advantage. Hybrid functionals were only relatively recently introduced into the ADF code, where the use of STO basis functions still makes them very expensive in computational terms.

2.9.3 Performance of OPBE Functional

When it comes to the spin states that are of primary interest in this thesis, functionals can be broadly separated into two categories: those that typically favour high spin states and those that stabilise low spin configurations.[25] Functional such as LDA,[19] BLYP[20-21] and PBE[26] typically fall in the second group while hybrid DFT functionals, particularly those with a large fraction of HF exchange, tend to favour high-spin states.

Some authors [27-28] have argued that the OPBE functional is one of the best GGA functionals available to handle such spin states, and this functional is used extensively in this thesis. The OPBE functional consists of the optimised exchange term "OPTX" developed by Handy[29] and the PBE correlation, PBEc.[26] Handy's group later developed OLYP in pursuit of higher accuracy by replace the correlation part by LYP.[21] Swart has shown, in an extensive series of studies on iron complexes, that the performance of OPBE is better than OLYP in predicting the right spin states.[30]

2.10 Spin Contamination and Broken Symmetry States

Throughout this thesis I will be concerned with paramagnetic systems, and so a brief discussion of issues particular to unrestricted methods (HF or DFT) is warranted. In an unrestricted Hartree-Fock (UHF) wavefunction, the excess of spin α over spin βelectrons in a single determinant is defined; by convention, the number of α electrons (N_α) is always greater than or equal to the number of β electrons (N_β). A single determinant is an eigenfunction of the $\hat{S}_z$ operator (its eigenvalue is $M_S\hbar$) but not necessarily of S^2, whose exact value is $S(S+1)$. In an unrestricted ansatz, the expectation value of S^2 is

$$\langle S^2 \rangle = \langle \phi_i | S^2 | \phi_j \rangle = \langle S^2 \rangle_{exact} + N_\beta - \sum_{i \in \alpha}^{N} \sum_{j \in \beta}^{N} \langle \phi_i | \phi_j \rangle^2 \qquad 2.51$$

N_β is the number of spin-β electrons in the whole system that are not paired with spin-α electrons in spatially similar orbitals. For example, in a system with a net total of 1 unpaired electron made up of 2 spin-α electrons localised entirely on one atom and 1 spin-β electron localised entirely on another,

$$\langle S^2 \rangle = \frac{3}{4} + 1 = 1.75$$

The spin contamination is the deviation of $\langle S^2 \rangle$ from its exact value given by $S(S+1)$. A common example of the effects of spin contamination of unrestricted single-determinant wavefunctions is the dissociation of the H_2 molecule. Single-determinant methods such as HF theory are adequate near equilibrium separation, and an unrestricted starting guess converges to a fully restricted solution (*i.e.* one in which the spin α and spin-β orbitals are spatially identical). Beyond the Coulson-Fisher (CF) point[31], the point at which the two curves in Figure 2.4 corresponding to restricted and unrestricted wavefunctions, diverge, a single determinant description is inadequate, and the electrons localise on opposite ends of the molecule in a so-called broken symmetry (BS) states. BS solution is closer to real singlet, except the later has zero spin after CF point.

The divergence of the red and green curves beyond the Coulson-Fischer point stems from the way that bond dissociation is described in the two methods: UB3LYP describe the bond breaking as homolytic ($2H^{\cdot}$) while RB3LYP over-estimates the ionic contributions (H^+H^-). At large separations, the BS and triplet configurations become degenerate as they differ only in the spin alignment of two increasingly weakly interacting electrons. At 3 Å, $\langle S^2 \rangle = \langle S^2 \rangle_{exact} + N_\beta = 0 + 1 = 1$ and the Mulliken spin densities (ρ) approach 1.0. Whilst the dissociation of H_2 is of limited interest, the majority of the systems studied in this thesis fall into the exchange-coupled category, where BS solutions are the norm. H_2 near its dissociation limit is therefore a useful simple model for much of what is described later.

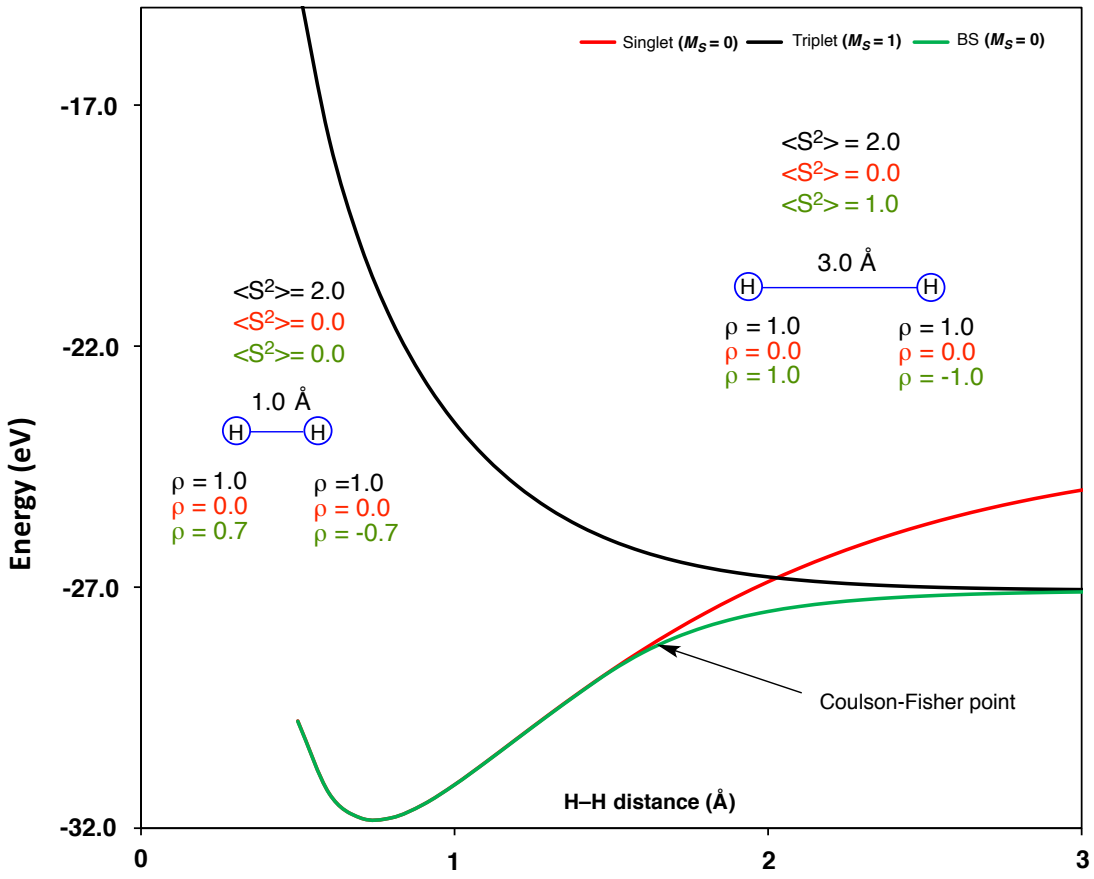


Figure 2.4: Potential energy diagram (PES) of hyrogen atom bond dissociation, calculated using the hybrid density functional B3LYP with 6-31G(d) basis sets. ρ represents Mulliken spin density on each atom.

2.11 The Coupling Between Paramagnetic Centres

The preceding discussion of H_2 near its dissociation limit serves as a useful introduction to the chemistry of exchange coupled systems, where two or more metal ions are held in close proximity by bridging ligands, but the electrons remain, to a first approximation, localised on a single centre. The interaction between the metal ions that leads to the observed magnetic properties is then term 'exchange coupling', and its study can be traced back to the original work of Guha[32] on copper(II)diacetate monohydrate. Guha argued that the temperature-dependent magnetic susceptibility,

and in particular the fact that it drops to zero at low temperature, cannot be explained in terms of isolated Cu^{II} centres with spin quantum number S=1/2. A subsequent EPR study published by Bleaney[33] suggested that the ground state was in fact a singlet due to antiferromagnetic coupling between Cu pairs in the systems. Later,[34] the same author introduced the idea of an exchange coupling constant J, between the two paramagnetic copper ions employing Van Vleck's equation. Remarkably, all this came before the structure of the complex was known, but a subsequent X-ray crystallographic study proved that the copper compound does actually exist in isolated pairs of $[Cu_2(OAc)_4(H_2O)_2]$. The precise nature of the interaction between the two Cu(II) pairs has been hotly debated, with various authors favouring direct interactions where orbitals on the metal centres overlap (Heisenberg[35]) or indirect interactions mediated by acetate ligands (Kramers[36]). Anderson[37] described the interaction of two paramagnetic centres through a bridging ligand as 'superexchange', as distinct from direct exchange. All the coupling constants discussed in this thesis are of the superexchange type.

2.12 Spin Hamiltonian

Heisenberg, Dirac and Van Vleck have developed a spin Hamiltonian, known as the HDVV Hamiltonian to account for these interactions. Various forms of the HDVV Hamiltonian are used in the literature, varying in the sign of *J* and the presence or otherwise of a factor of 2. In the first two formulae, negative and positive valued of *J* refer to antiferromagnetic and ferromagnetic coupling, respectively. In the third version (Equation 2. 54), in contrast, negative and positive *J* imply ferro- and antiferromagnetic

coupling respectively. The existence of three versions can result in confusion when interpreting the signs and absolute values of coupling constants in the literature.

$$\widehat{H}^{HDVV} = -\sum_{i>j} J_{ij}\hat{S}_I\hat{S}_J \qquad 2.52$$

$$\widehat{H}^{HDVV} = -2\sum_{i>j} J_{ij}\hat{S}_I\hat{S}_J \qquad 2.53$$

$$\widehat{H}^{HDVV} = +\sum_{i>j} J_{ij}\hat{S}_I\hat{S}_J \qquad 2.54$$

An arbitrary spin Hamiltonian can be built up by considering all possible combinations of the spin pairs. If the values of *J* are known, operation of this Hamiltonian on a basis constructed from pairs of spin functions then generates the HDVV Hamiltonian matrix, diagonalization of which generates the eigenvalues and eigenfunctions. Finally, the eigenvalues can be used to reconstruct the magnetic functions that are accessible to experiment through the van Vleck equation.

$$M = \frac{N\sum_{N=1}^{\infty} -\frac{\delta E_n}{\delta H}\exp(-\frac{\mathrm{E_n}}{kT})}{\sum_{N=1}^{\infty}\exp(-\frac{\mathrm{E_n}}{kT})} \qquad 2.55$$

The parameters *k* and N are Boltzmann constant and Avogadro's number respectively. Van Vleck proposed to simplify the formula by considering a Taylor expansion of the energy, the expansion includes only first and second order Zeeman coefficients. The final version of the expression becomes

$$M = \frac{NH\sum_{N=1}^{\infty}[\frac{(E_n^1)^2}{\delta H} - 2\mathrm{E_n^2}]\exp(-\frac{\mathrm{E_n^0}}{kT})}{\sum_{N=1}^{\infty}\exp[-\frac{\mathrm{E_n^0}}{kT}]} \qquad 2.56$$

The magnetic susceptibility, χ, is the first dervitative of the above expression relative to the magnetic field, then one can easily calculate χ by the following:

$$\chi = \frac{\delta M}{\delta H} \qquad 2.57$$

In experimental studies, the magnetic exchange coupling parameters *J* are typically treated as variables, determined by fitting to the available susceptibility data. This process can, however, be problematic because the high number of distinct coupling pathways may lead to multiple solutions that give fits of equal quality. An alternative strategy discussed later in this chapter is to use theoretical techniques (DFT in our case) to make an *ab initio* estimate of the exchange coupling constants, and then, if required, use these values to guide the fitting algorithm.

2.13 The Origin of the Exchange Interaction

Solving the spin Hamiltonian provides a quantitative and qualitative description of the magnetic coupling, but it gives no information about its origin. Early attempts to explain the coupling interaction between two paramagnetic metals identified two classes; (1) ”direct exchange”, proposed by Heisenberg[38], which describes the interaction between the metals in which the distance between them is roughly the sum of their covalent (van der Waals) radii, and (2) “superexchange”, proposed by Kramers[36], where the interaction involves a bridging ligand (L). At a qualitative level, the Goodenough-Kanamori [39-41] rules are often used to rationalise and predict the sign and magnitude of the exchange coupling. For example in the 180^{o} case (Figure 2.5a), the M-L-M orbital overlap will be maximised and the simultaneous partial electron donation of spin density from the ligand to the adjacent two metals enforces the spin moments the metals sites to be aligned oppositely (antiferromagnetically). In the 90^{o} case (Figure 2.5b), in contrast, two different orbitals on the ligand interact covalently with the two metal orbitals, leading to dominant ferromagnetic exchange.

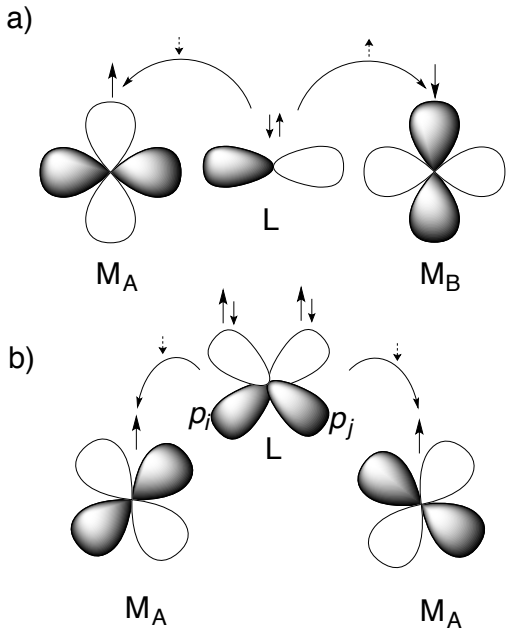


Figure 2.5: the M-L-M exchange, (a) antiferromagnetic coupling in 180° case. b) ferromagnetic coupling 90° case.

2.14 Quantitative Models for the Exchange Interaction

2.14.1 Orthogonal Magnetic Orbitals Model (HTH)

One of the earliest attempt to explain the exchange coupling phenomenon on a quantitative basis was proposed by Anderson in 1950,[37] who introduced the concept of orthogonal localised molecular orbitals, ϕ_i and ϕ_j. For the simplest case of two paramagnetic centres with one unpaired electron localised on each of the two orbitals, *J* is simply the difference in energy between the singlet and triplet states. Anderson proposed the following expression for the value of *J*:

$$E_S - E_T = J = 2K_{ij} - \frac{4t^2}{U} \qquad 2.58$$

where K_{ij} is a two electron exchange integral which is intrinsically positive, and so favours a ferromagnetic state (*i.e* a triplet). The antiferromagnetic contribution comes

from a so-called transfer term (t) related to the degree of delocalisation of the spins, which is resisted by the U term which reflects the energetic cost of pairing two electrons in the same orbital.

Hay, Thibeault, and Hoffmann (HTH) later used the idea of orthogonal orbitals to deal with the centrosymmetric bimetallic systems such as M_a-X-M_b with one unpaired electron on each one, connected via diamagnetic bridging atom(s) ($[Cu^{II}(OAc)_4]_2$, for example). Each of the d orbitals (d_a and d_b) of the two metal centres is occupied by one unpaired electron. The linear combination of the metallic d orbitals with the ligand orbital produces two molecular orbitals ϕ_1 and ϕ_2. The electronic configurations that arise from this model are summarised in Figure 2.6. The ground state can be described as a linear combination of S1 and S2

$$\psi_S = c_1\psi_1 + c_2\psi_2 \qquad 2.59$$

while the energy of the triplet state can be determined unambiguously from either of the single determinant wavefunctions, $\psi_{T,1+}$ or $\psi_{T,1-}$.

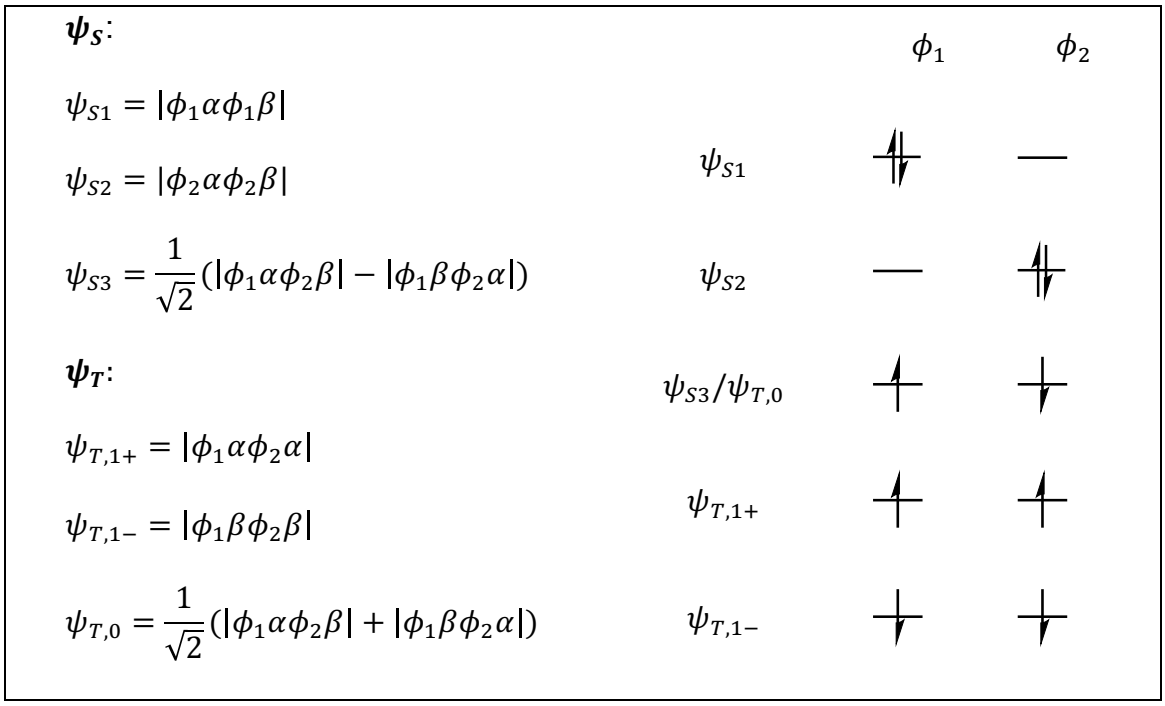


Figure 2.6: Ground and triplet state wave function configuration of di-nuclear paramagnetic systems of S=1.

In the limit of strong interactions, the singlet-triplet separation can be expressed as:

$$E_S - E_T = -J_{12} + \frac{1}{2}(J_{11} - J_{22}) - \frac{(\epsilon_1 - \epsilon_2)^2}{2K_{12}} \quad \text{2. 60}$$

where ϵ_1 and ϵ_2 represents the eigenvalues of the molecular orbitals ϕ_1 and ϕ_2. The two-electron integrals in this equation J_{ij} and K_{ij} are the Coulombic and exchange integrals respectively. Expressed in terms of the localised component orbitals ϕ_a and $\phi_b$where $\phi_a = \frac{1}{\sqrt{2}}(\phi_1 + \phi_2)$ and $\phi_b = \frac{1}{\sqrt{2}}(\phi_1 - \phi_2)$, the energy expression reduces to a form very similar to that proposed by Anderson.

$$E_S - E_T = J = 2K_{ab} - \frac{(\epsilon_1 - \epsilon_2)^2}{J_{aa} - J_{ab}} \quad \text{2. 61}$$

The HTH model shows that the exchange coupling *J* is dependent on the energy difference between singly occupied orbitals (SOMOs) ϕ_1 and ϕ_2. Unfortunately, the HTH model is a simple one and it is difficult to extend to more complex systems with more than one unpaired electron on each metal or to heterometallic and polymetallic systems.

2.14.2 The Kahn-Briat Model (KB)

This model, also known as the valence bond approach, takes as its basis the natural magnetic orbitals (NMOs), for M-X-M systems, where a and b are orbitals belonging to the Ma-X and Mb-X fragments. Assuming the interaction between the two metals is weak, a wavefunction of the Heitler-London form can be used:

$$\Psi = \frac{1}{\sqrt{2(1 \pm S^2)}}[\chi_a(1)\chi_b(2) \pm \chi_a(1)\chi_b(1)] \quad \text{2. 62}$$

The negative and positive signs in the wavefunction relate to the single and triplet states respectively. The difference between the eigenvalues of these states is then given by the following expression.

$$E_S - E_T = J = J_F + J_{AF} \approx 2K_{ab} + 4h_{ab}S_{ab} \quad \text{2. 63}$$

where the parameters K and h represent the exchange and one-electron integrals while S_{ab} represents the overlap term. As the SOMOs approach orthogonality, S_{ab} vanishes and the ferromagnetic term dominates ($J = 2K_{ab}$).

2.14.3 DFT Broken Symmetry Models (DFT-BS)

I noted above that values of *J* can, in principle, be extracted by fitting to measured magnetic susceptibilities. Unrestricted electronic structure approximations such as unrestricted Hartree-Fock (UHF) and density functional theory (UDFT) provide an alternative means of estimating the separation between the states that emerge from a Heisenberg spin ladder. For polymetallic open shell systems, the antiferromagnetically coupled solution that emerges from UHF or UDFT calculations has electrons localised on different metal centres, much like H_2 at its dissociation limit, and is called a broken-symmetry (BS) solution. In 1981, Noodleman developed the first successful model to extract *J* from BS-DFT solutions of polymetallic systems.[42] To illustrate the process, consider an M_a-X-M_b system with one unpaired electron on each metal atom, occupying orbitals ϕ_a and ϕ_b. The wavefunctions to describe the two spin states singlet and triplet are:

$$\psi_S = \frac{1}{\sqrt{2}}(|\phi_a\alpha\phi_b\beta| - |\phi_a\beta\phi_b\alpha|) \quad \text{2. 64}$$

$$\psi_{T,1-} = |\phi_a\alpha\phi_b\alpha|; \psi_{T,1-} = |\phi_a\alpha\phi_b\alpha| \quad \text{2. 65}$$

$$\psi_{T,0} = \frac{1}{\sqrt{2}}(|\phi_a\alpha\phi_b\beta| + |\phi_a\beta\phi_b\alpha|) \quad \text{2. 66}$$

As shown earlier in Figure 2.6, while the energy of the triplet state $|\uparrow\uparrow\rangle$ can be computed using a single determinant $|\uparrow\uparrow\rangle$, the singlet ψ_S can only be represented with two determinants, $|\downarrow\uparrow\rangle - |\uparrow\downarrow\rangle$. The broken symmetry wavefunction

$$\psi_{BS} = |\phi_a \alpha \phi_b \beta| \qquad 2.67$$

only represents one of these two components, either, $|\uparrow\downarrow\rangle$ or $|\downarrow\uparrow\rangle$, and is called "broken symmetry" because the electronic symmetry of the system is lower ('broken') than the nuclear symmetry.

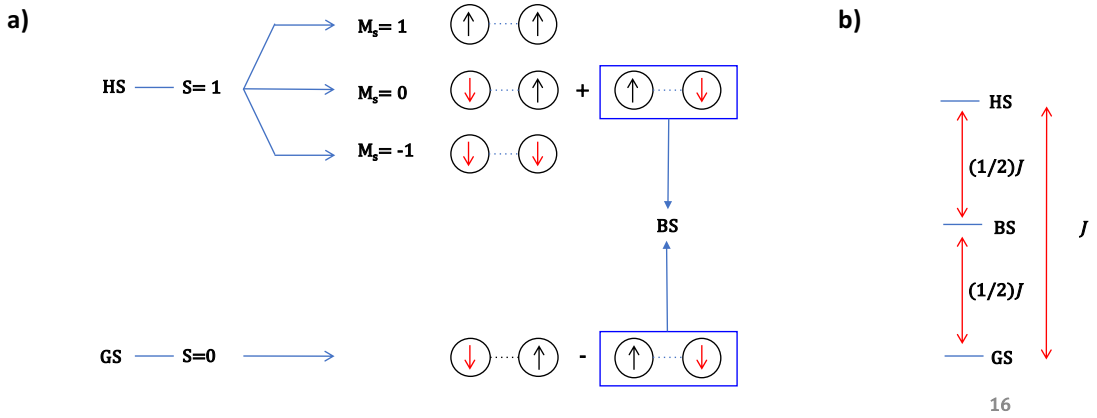


Figure 2.7: **(a)** Singlet and triplet spin state wavefunction components for paramagnetic centre with S=1/2 on each centre. (**b**) The relative energy of the three (ground state; GS, broken symmetry state; BS, high spin; HS) states. For such systems, BS here fall half way between the HS and the singlet.

Qualitatively, the broken-symmetry configuration contributes to both the singlet, ψ_S, and also the triplet, $\psi_{T,0}$, and so ψ_{BS} can be represented by a linear combination of the pure spin states ψ_S and $\psi_{T,0}$.

$$\psi_{BS} = \frac{1}{\sqrt{2}}(\psi_S + \psi_{T,0}) \qquad 2.68$$

Therefore, the energy of the broken-symmetry state falls exactly midway between the pure singlet and triplet states and so the coupling constant, *J*, will be twice the gap between the broken symmetry and triplet states

$$J = 2(E_{BS} - E_T) \qquad 2.69$$

Approaches to calculating *J* in more complex systems follow the same principle of computing single-determinant configurations and then projecting out the energy of the

true singlet which is intrinsially inaccessible to a single-determinant method. This leads to the generalised expression for arbitrary spins,

$$J = \frac{E_{BS} - E_{HS}}{2S_a.S_b} \qquad 2.70$$

where S_a and S_b are the spin quantum numbers on the metal a and b. This formula developed by Ginsberg[43] along with Noodleman and Davidson.[44] This simple expression has been used for different systems with remarkable accuracy,[45-49] particularly in cases of strong orbital localization where the overlap between the two paramagnetic centres M_a and M_b, (S_{ab}~0) is weak.

In cases of strong overlap (S_{ab}~1) and therefore greater delocalisation of the magnetic orbitals, the broken-symmetry state converges on the true singlet. In such circumstance Ruiz has proposed[50] an 'unprojected' approach which yields smaller values of J for a given energy separation.

$$J = \frac{E_{BS} - E_{HS}}{2S_a.S_B + S_b} \qquad 2.71$$

Yamaguchi and co-workers[51] have proposed a third formula which uses the expectation values of $\langle S^2 \rangle = S(S+1)$ for each spin state to weight the computed energy separation.

$$J = \frac{E_{BS} - E_{HS}}{\langle S^2 \rangle_{HS} - \langle S^2 \rangle_{LS}} \qquad 2.72$$

The Yamaguchi formula also results in smaller *J* than the projected expression, and it has been used for many organic radicals using UHF and post-HF methods such as Møller–Plesset perturbation theory (MP2).

2.15 References

[1] E. Schrödinger, *Annalen der Physik* **1926**, *79*, 361-376.

[2] L. de Broglie, *Annalen der Physik* **1925**, *3*, 22.

[3] A. Szabo and N. S. Ostund, *Modern Quantum Chemistry*, Dover Publications, Inc, New York, **1996**, p.

[4] M. Born and J. R. Oppenheimer, *Annalen der Physik* **1927**, *84*, 457.

[5] E. A. Hylleraas, *Zeitschrift für Physik* **1928**, *48*, 469.

[6] E. A. Hylleraas, *Zeitschrift für Physik* **1929**, *54*, 347.

[7] E. A. Hylleraas, *Zeitschrift für Physik* **1930**, *65*, 209.

[8] D. R. Hartree, *Mathematical Proceedings of the Cambridge Philosophical Society* **1928**, *24*, 89-110.

[9] V. Fock, *Zeitschrift für Physik* **1930**, *61*, 126.

[10] J. C. Slater, *Physical Review* **1930**, *35*, 210-211.

[11] J. von Neumann, *Nachrichten von der Gesellschaft der Wissenschaften zu Göttingen, Mathematisch-Physikalische Klasse* **1927**, *1927*, 245–272.

[12] L. Landau, *Zeitschrift für Physik* **1927**, *45*, 430-441.

[13] F. Jensen, *Introduction to Computational Chemistry, 2nd Edition*, John Wiley & Sons Ltd., West Sussex, **2007**, p. 620.

[14] C. J. Cramer, *Essentials of Computational Chemistry: Theories and Models, 2nd Edition*, John Wiley & Sons Ltd., West Sussex, **2004**, p. 618.

[15] S. F. Boys, *Proceedings of the Royal Society of London. Series A. Mathematical and Physical Sciences* **1950**, *200*, 542.

[16] P. Hohenberg and W. Kohn, *Physical Review* **1964**, *136*, B864--B871.

[17] P. M. W. Gill in *Density Functional Theory (DFT), Hartree–Fock (HF), and the Self-consistent Field*, John Wiley & Sons, Ltd, **2002**.

[18] L. H. Thomas, *Mathematical Proceedings of the Cambridge Philosophical Society* **1927**, *23*, 542-548.

[19] S. H. Vosko, L. Wilk and M. Nusair, *Canadian Journal of Physics* **1980**, *58*, 1200-1211.

[20] A. D. Becke, *Physical Review A* **1988**, *38*, 3098-3100.

[21] C. Lee, W. Yang and R. G. Parr, *Physical Review B* **1988**, *37*, 785-789.

[22] P. J. Stephens, F. J. Devlin, C. F. Chabalowski and M. J. Frisch, *The Journal of Physical Chemistry* **1994**, *98*, 11623-11627.

[23] M. Reiher, O. Salomon and B. Artur Hess, *Theoretical Chemistry Accounts* **2001**, *107*, 48-55.

[24] A. D. Becke, *Journal of Chemical Physics* **1993**, *98*, 1372-1377.

[25] M. Swart, A. W. Ehlers and K. Lammertsma *Molecular Physics* **2004**, *102*, 2467-2474.

[26] J. P. Perdew, K. Burke and M. Ernzerhof, *Physical Review Letters* **1996**, *77*, 3865-3868.

[27] M. Swart, *Journal of Chemical Theory and Computation* **2008**, *4*, 2057-2066.

[28] M. Swart, *International Journal of Quantum Chemistry* **2013**, *113*, 2-7.

[29] N. C. Handy and A. J. Cohen, *Molecular Physics* **2001**, *99*, 403-412.

[30] M. Swart, A. R. Groenhof, A. W. Ehlers and K. Lammertsma, *The Journal of Physical Chemistry A* **2004**, *108*, 5479-5483.

[31] C. A. Coulson and I. Fischer, *The London, Edinburgh, and Dublin Philosophical Magazine and Journal of Science* **1949**, *40*, 386-393.

[32] B. C. Guha, *Proceedings of the Royal Society (London)* **1951**, *A206*, 353.

[33] B. Bleaney and K. D. Bowers, *Proceedings of the Royal Society of London. Series A, Mathematical and Physical Sciences* **1952**, *214*, 451-465.

[34] B. Bleaney, *Reviews of Modern Physics* **1953**, *25*, 161-162.

[35] W. Heisenberg, *Zeitschrift für Physik* **1928**, *49*, 619-636.

[36] H. A. Kramers, *Physical Chemistry Chemical Physics* **1934**, *1*, 182.

[37] P. W. Anderson, *Physical Review* **1950**, *79*, 350-356.

[38] W. Heisenberg, *Zeitschrift für Physik* **1926**, *38*, 411-426.

[39] J. B. Goodenough, *Physical Review* **1955**, *100*, 564-573.

[40] J. B. Goodenough, *Journal of Physics and Chemistry of Solids* **1958**, *6*, 287-297.

[41] J. Kanamori, *Journal of Physics and Chemistry of Solids* **1959**, *10*, 87-98.

[42] L. Noodleman, *The Journal of Chemical Physics* **1981**, *74*, 5737-5743.

[43] A. P. Ginsberg, *Journal of the American Chemical Society* **1980**, *102*, 111-117.

[44] L. Noodleman and E. R. Davidson, *Chemical Physics* **1986**, *109*, 131-143.

[45] S. Yamanaka, T. Kawakami, H. Nagao and K. Yamaguchi, *Chemical Physics Letters* **1994**, *231*, 25-33.

[46] K. Yamaguchi, H. Fukui and T. Fueno, *Chemistry Letters* **1986**, *15*, 625-628.

[47] L. Noodleman and E. J. Baerends, *Journal of the American Chemical Society* **1984**, *106*, 2316-2327.

[48] J. M. Mouesca, L. Noodleman and D. A. Case, *Inorganic Chemistry* **1994**, *33*, 4819-4830.

[49] I. Rudra, Q. Wu and T. Van Voorhis, *The Journal of Chemical Physics* **2006**, *124*, 024103.

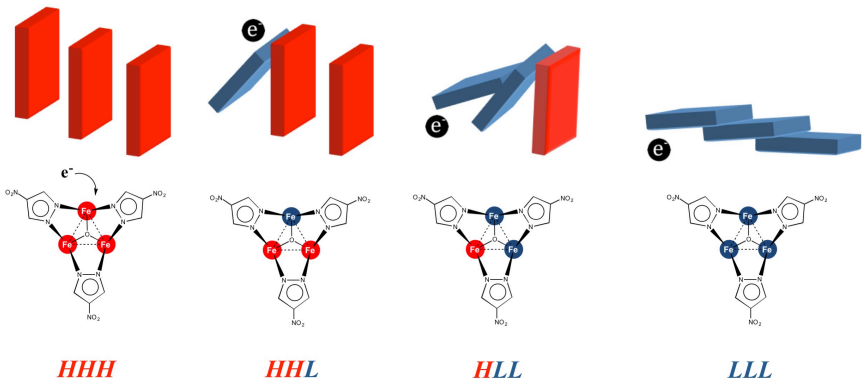
[50] E. Ruiz, A. Rodríguez-Fortea, J. Cano, S. Alvarez and P. Alemany, *Journal of Computational Chemistry* **2003**, *24*, 982-989.

[51] M. Shoji, K. Koizumi, Y. Kitagawa, T. Kawakami, S. Yamanaka, M. Okumura and K. Yamaguchi, *Chemical Physics Letters* **2006**, *432*, 343-347.

3

3 A Redox-Induced Spin-State Cascade in a Mixed-Valent $Fe_3(\mu_3\text{-}O)$ Triangle

In this chapter, we discuss the redox-dependent electronic structure of oxo-bridged iron triangular clusters, $[Fe_3(\mu_3\text{-}O)(LL)_6X_3]^{3+/2+}$, where LL= pyrazolato (Pz) and either X= CN^- or NCS^-. The NCS-terminated molecule shows remarkable redox-dependent magnetic behavior, wherein all three iron centres switch from high spin to low spin configurations in response to one-electron reduction ($[Fe_3]^{9+} \rightarrow [Fe_3]^{8+}$). These systems were synthesised by Professor Raphael Raptis (Florida International University), and the Mössbauer spectra were measured by Dr Yiannis Sanakis at the Demokritus Institute, Athens. The work was published in Angew. Chem. Int. Ed., ***2017****, 56, 582-586.*[1]



3.1 Introduction

3.1.1 Trinuclear Metal Complexes

Trinuclear metallic compounds with the general formula $[M_3(\mu_3\text{-}O)(LL)_6X_3]^z$ are a diverse family, known for much of the first transition series. The three metals are linked via a tris-oxo-bridge and six bidentate (LL = pyrazolato or carboxylate) ligands. The monodenate ligand, X, completes the approximately octahedral coordination sphere around each metal, lying *trans* to the M-O bond.

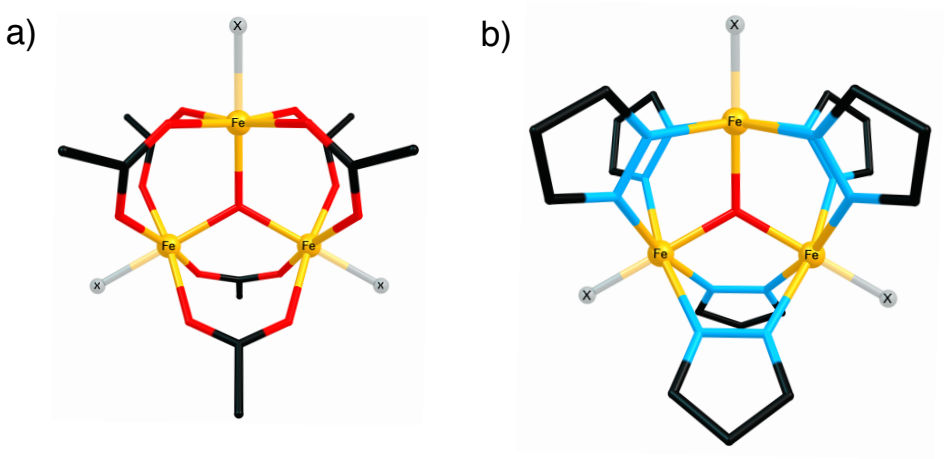


Figure 3.1: structure of the oxo-bridged tri-iron complexes $[Fe_3(\mu_3\text{-}O)(LL)_6X_3]^z$: (**a**) LL = carboxylate and (**b**) LL = pyrazolate. The atoms' colour: red; oxygen, black; carbon, cyan; nitrogen; grey; a monodenate ligand X.

These compounds have in fact been known since the nineteenth century, when the Cr^{III} clusters were first synthesised but wrongly formulated as $Cr_2(OOCH_3)_3.Cr(OH)_3$, with the three metals linked by two oxygens instead of one.[2] Independently, Weinland[3-4] and Werner[5] showed that there are six equivalent carboxylates in the complex sphere and suggested the metals were linked by two hydroxyl groups and six carboxylates. It was the physicist, Welo, who first argued that the three metals must be linked by one central oxide, because the strong antiferromagnetic interaction between the metals is inconsistent with hydroxyl bridged Cr^{III}.[6-7] This formulation was

not widely accepted by the chemistry community until Orgel pointed out that if OH^- ligands were present, they should be readily replaced by halides.[8] Five years later, Welo's proposal was confirmed by the newly discovered X-ray crystallography technique.[9] Fe^{III} and Mn^{III} also tend to favour octahedral coordination, and a review of the earlier literature by Handbuch[2] revealed that isostructural clusters of these metals had, in fact, already been synthesised but not formulated correctly.

Following these original discoveries, the chemistry of the $M_3(\mu_3\text{-}O)$ motif has been developed extensively, and they have been used as starting materials for the synthesis of higher nuclearity molecules[10-12] and as catalysts for oxidation reactions.[13-14] They have also been discovered in nature, for example in pillar formations in caves.[15] Their physical properties, most notably their magnetism, have also served as important models for exchange coupling. For example, the strong antiferromagnetic coupling noted by Welo leads to an $S = 1/2$ ground state for the all-ferric carboxylate clusters, $[Fe_3(\mu_3\text{-}O)(OOCR)_6X_3]$.[16-18] In the context of this work, the properties of the one-electron reduced carboxylate clusters are particularly relevant: at low temperatures, the extra electron is localised on one of the three irons, while at high temperatures, it becomes delocalised over all three centres.[16-21] For example, Sato *et al* reported the temperature-dependent crystallography of $[Fe_3(\mu_3\text{-}O)(OOCH_2X)_6(H_2O)_3]$, X= H, Cl, and Br, showing that one of the three M-O distances was noticeably longer at low temperatures, supporting a localised $Fe^{II}Fe^{III}Fe^{III}$ description.[18] Most importantly, however, the metal centres remain in high-spin configurations across the entire temperature range.

In this chapter, we discuss the properties of a new class of oxo-bridged iron triangles, where bridging pyrazolato ligands replace the traditional carboxylate groups

(Figure 3.1). The chemistry of the pyrazolate-bridged systems has been developed extensively by Raptis and co-workers over the past decade,[22-24] with M= Co^{3+} and Fe^{3}. In structural terms, the N–N bridge of the pyrazolate has a smaller bite angle than the OCO of the carboxylate analogue, making the Fe-Fe distances somewhat shorter. Nevertheless, the dimensions of the Fe_3O core are similar: Fe…Fe and Fe-O distances are within the range of ~1.8-2.0 and ~3.2-3.3 in both complexes. The MN_4 moiety in the pyrazolato complex is also somewhat more planar than the MO_4 analogue in the carboxylate complex. The key difference between the ligands is that the pyrazolate induces a slightly stronger ligand field, and so gives access to low-spin configurations. In the case of the CN capped pyrazolato complex, $[Fe_3(\mu_3\text{-}O)(NO_2\text{-}Pz)_6(CN)_3]^z$ ($[Fe_3O(CN)_3]^z$), crystallographic data (Table 3.1) suggests that the mixed valence state (z = 3–) is low spin. X-ray data are not available for the all-ferric analogue (z = 2–) but Mössbauer data (to be introduced in section 3.3.4) suggests that it is also low spin. The CN complex therefore, represents a complete contrast from the carboxylate, where the high spin configuration dominates in both oxidation states. The initial motivation for this project was the structural and spectroscopic evidence from our collaborators (Raptis, Sanakis) which suggested that whilst the all-ferric compound $[Fe_3(\mu_3\text{-}O)(NO_2\text{-}Pz)_6(NCS)_3]^2$ ($[Fe_3O(NCS)_3]^2$) contains three high-spin Fe^{II} centres (like the carboxylate analogue), one-electron reduction ($[Fe_3O(NCS)_3]^{3-}$) causes all three to switch to low-spin (like the cyanide analogue). If true, this would constitute the first example of a one-electron redox process causing spin crossover in multiple centres.

Table 3.1: Summary of experimental M-L bond lengths (in Å) before (all-ferric) and after (mixed valence) one-electron reduction

	Bond	Fe_3^{III} (all ferric)	$Fe^{II}Fe_2^{III}$ (mixed valence)
$[Fe_3O(NCS)_3]^z$	Fe–O	1.88	1.77
	Fe–NCS	1.98	1.94
	Fe–N(Pz)	2.15	1.97
$[Fe_3O(CN)_3]^z$	Fe–O	–	1.75
	Fe–NCS	–	1.98
	Fe–N(Pz)	–	1.93

3.1.2 Spin Crossover

Spin crossover (SCO) was first identified by Cambi and coworkers in the early 1930s as a result of their work on Fe^{III} compounds, where they noted that different spin states were present at different temperatures.[25-26] SCO is the process whereby the spin state changes from high spin (HS) to low spin (LS) in response to changes in physical conditions such as pressure or temperature. The change in spin state is typically accompanied by dramatic changes in bond lengths and angles.[27] In principle, spin crossover is possible for first row transition metal ions with d^4, d^5, d^6 and d^7 configurations, although the phenomenon is most common for d^6, especially for Fe^{II} complexes.[28] In the solid state, it is possible that all metals undergo spin crossover in a very narrow temperature range, giving a so-called “abrupt” transition. Alternatively, a two-step crossover is possible, where a mixed high/low-spin state (HL) is stable for a range of temperatures, as, for example in $[Fe(bt)(NCX)_2]_2(bpym)$ pbym = 2,2'-bipyrimidine,bt = 2,2'-bi-2-thiazoline, X = S or Se. Multi-step spin crossover of this type

was first explored by Bolvin, Kahn and co-workers,[29] who argued that an intermediate HL state is only stable if its energy is lower than the average of the two extremes, high/high (HH) and low/low (LL) spin configurations. More recently, Borshch and co-workers [30] studied a series of bi-nuclear Fe^{II} complexes, and argued that a multi-step spin transition is indeed found in cases where the HL energy fall below the average HH/LL energy. They also showed that ligand strain plays a dominant role in controlling the energy of the intermediate HL states:[31-33] if the HS to LS crossover on one of the centres changes the ligand coordination geometry on the neighbouring centre such that it favours the HS configuration (*i.e.* it weakens the ligand field) then the HL intermediate will be stabilised.

A variety of spectroscopic tools have been used to study SCO phenomena. Changes in ligand-metal (M–L) bond lengths are an obvious consequence of the spin transitions, due to a change in d orbital (t_{2g} and e_g) occupation and this also leads to measurable changes in magnetic properties. Infrared spectroscopy can also be used as an indicator of spin transitions as the metal-ligand stretching vibration in the low spin state is typically blue shifted by ~(250 – 500) cm^{-1}. It is, however, often difficult to detect these stretches. In some instances, internal ligand vibrations are also a good indicator of changes in spin state at the metal atom, as in the classic system $Fe(phen)_2(NCS)_2$[28, 34] where the N–C bond stretches in the NCS ligand shift from 2060 cm^{-1} and 2070 cm^{-1} for HS to ~(2100 – 2110) cm^{-1} when crossover to LS occurs. ^{57}Fe Mössbauer spectroscopy has become one of the most powerful techniques to study spin crossover in iron chemistry since its discovery in 1958,[35] because different states exhibit unique Mössbauer parameters (isomer shift δ, quadrupole splitting, ΔE_Q). Mössbauer spectroscopy is now a standard technique used to study the

electronic structure of iron containing compounds such as proteins, biologically important inorganic molecules and metalloprotein reaction mechanisms.[36]

Redox events are well known to influence spin state, as for example in cobalt chemistry where one electron oxidation of Co^{II} to Co^{III} typically drives a transition to LS and is responsible for very slow electron transfer kinetics.[37] Less well understood, however, is the effect of one-electron redox chemistry on polymetallic array of metals: does the redox event change the spin state of only one centre, or can more complex concerted effects take place? The experimental data for $[Fe_3O(NCS)_3]^{2-}$ suggests the latter, and the role of theory is to first to validate the spectroscopic assignments, and then to establish why one-electron reduction causes a concerted spin crossover cascade rather than affecting only a single centre. The new data also presents an important opportunity to benchmark the performance of different functionals in the context of spin crossover.

3.2 Computational Details

The calculations employed the Amsterdam Density Functional (ADF 2013.01) package which uses Slater type basis functions to expand the Kohn-Sham orbitals.[38-39] The geometry optimizations are started from experimental coordinates, and the pure OPBE functional was used with polarised double-zeta (DZP) quality basis sets for the main group atoms and polarised triple zeta (TZP) for the irons. The frozen core approximation was chosen to reduce the cost of the calculations. The calculations have been carried out for two oxidation states, and for every oxidation state we have a choice of four coupled states (high/low-spin antiferromagnetic/ferromagnetic). Spin contamination and Mulliken spin density are routinely monitored to validate assignments of spin state.

After we have obtained the optimised geometry, Mössbauer parameters (quadrupole splitting and isomer shift) are calculated using the conductor-like screening model (COSMO) solvation model. COSMO was developed by Klamt and Schüürmann by introducing an accurate algorithm to describe the dielectric screening in a range of solvents using conductor screening as starting point.[40] Single point calculations were performed using the VWN-PW91 functional which combined the local density description of exchange with Vosko, Wilk and Nusair's correlation functional[41] and Perdew-Wang's[42] generalised gradient correlation functional with all-electron polarised triple-zeta basis sets for all the elements (the change of functional is necessary to allow direct comparison with Noodlemans' published correlation between the experiment and theory). The use of all-electron basis sets for the Mössbauer studies is vital because the isomer shift is a sensitive function of the s-electron density at the nucleus so the core electrons are very important.

The density functional calculations yield the electron density at the nucleus, $\rho(0)$, as the key variable. This density is linearly related to the isomer shift through equation 3.1 where α and C are empirical parameters obtained through regression analysis using standard compounds. The need for a regression analysis of this type means that the absolute computed chemical shift is rather unreliable (it is sensitive to the quality of the test set used to perform the analysis) but the *relative* values (*i.e.* the redox-induced shift) are more robust.

$$\delta = \alpha\rho(0) + C \qquad 3.1$$

The equation above relates experimental shift, δ to computed density at the nucleus $\rho(0)$. The slope value, α has been calculated using the experimental data from ref [43]

and comparison with computed values leads to a best-fit parameter of $\alpha = -0.3707$ and intercept with y-axis $C = 4385.6$ (Figure 3.2).

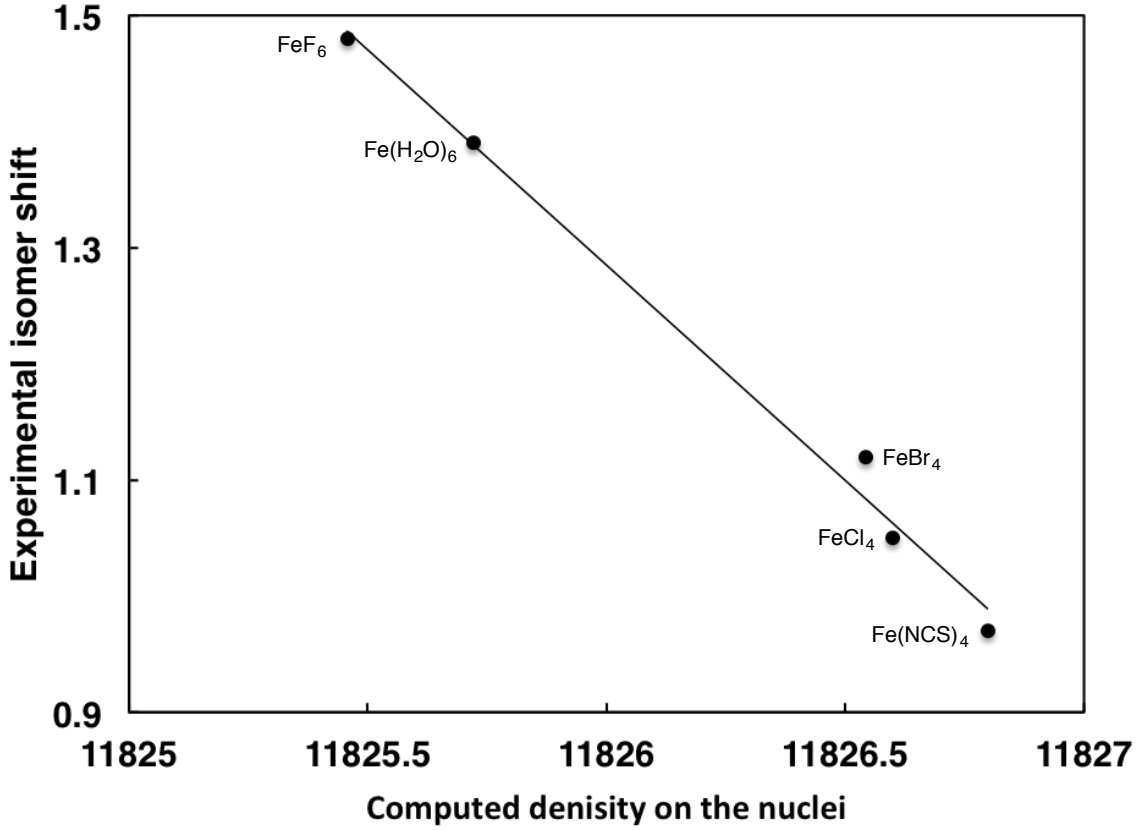


Figure 3.2: the relationship between the observed isomer shift, δ and the electron density at the nucleus, $\rho(0)$. The experimental isomer shift data is taken from reference [43], while we employed the model VWN-PW91/TZP to calculate electron density at the nucleus.

The quadrupole splitting is defined by

$$\Delta E_Q = \frac{eQV_{ZZ}(1+\eta^2/3)^{1/2}}{2} \qquad 3.2$$

$$\eta = \left|\frac{V_{xx} - V_{yy}}{V_{zz}}\right| \qquad 3.3$$

where $V_{zz} > V_{yy} > V_{xx}$ and $V_{zz} + V_{yy} + V_{xx} = 0$, therefore, $0 < \eta < 1$. It is clear from Equation 3.2 that if a nucleus has a nuclear quadrupole moment Q it will interact with the Electric field Gradient (EFG), V, generated by the electron density at the nucleus,

the magnitude of the interaction depending on the symmetry of the electric field around the nucleus (determined by V_{zz} and η, the asymmetry parameter).

3.3 Results and Discussion

3.3.1 Spin States

Before discussing the results in detail, we need to consider the possible spin states that can be accessed using a single-determinant methodology such as broken-symmetry DFT. For the all-ferric, all-high-spin case, exchange coupling between three centres with $S = 5/2$ leads to a total of $(2S+1)^3 = 216$ distinct configurations spanning multiplicities from 1/2 to 15/2, of which only the ferromagnetic case ($S = 15/2$) can be accurately described by a single determinant (the $M_S = +15/2$ component of $S = 15/2$ is given by $\left|\frac{15}{2};\frac{15}{2}\right\rangle$ ($\left|\frac{5}{2},\frac{5}{2},\frac{5}{2}\right\rangle$ is the uncoupled representation). However, if we restrict attention to states with maximum local spin multiplicity (*i.e.* $S = 5/2$ at each iron centre, in accord with Hund's rules), we can also define an antiferromagnetic "broken-symmetry" state with $M_S = 5/2$: ($\left|\frac{5}{2},\frac{5}{2},-\frac{5}{2}\right\rangle$). This broken-symmetry configuration does not represent a pure spin state, but is a close approximation, in energetic terms, to the antiferromagnetic ground state. In Figure 3.3, The antiferro- (AF) and ferromagnetic (F), coupled states (columns a and b, respectively) of the all-high-spin configuration (HHH) are shown in the top row. At the opposite end of the spectrum, the LLL configuration also gives rise to ferromagnetic and antiferromagnetic coupled states with $M_S = 3/2$ ($\left|\frac{1}{2},\frac{1}{2},\frac{1}{2}\right\rangle$) and 1/2 ($\left|\frac{1}{2},\frac{1}{2},-\frac{1}{2}\right\rangle$).

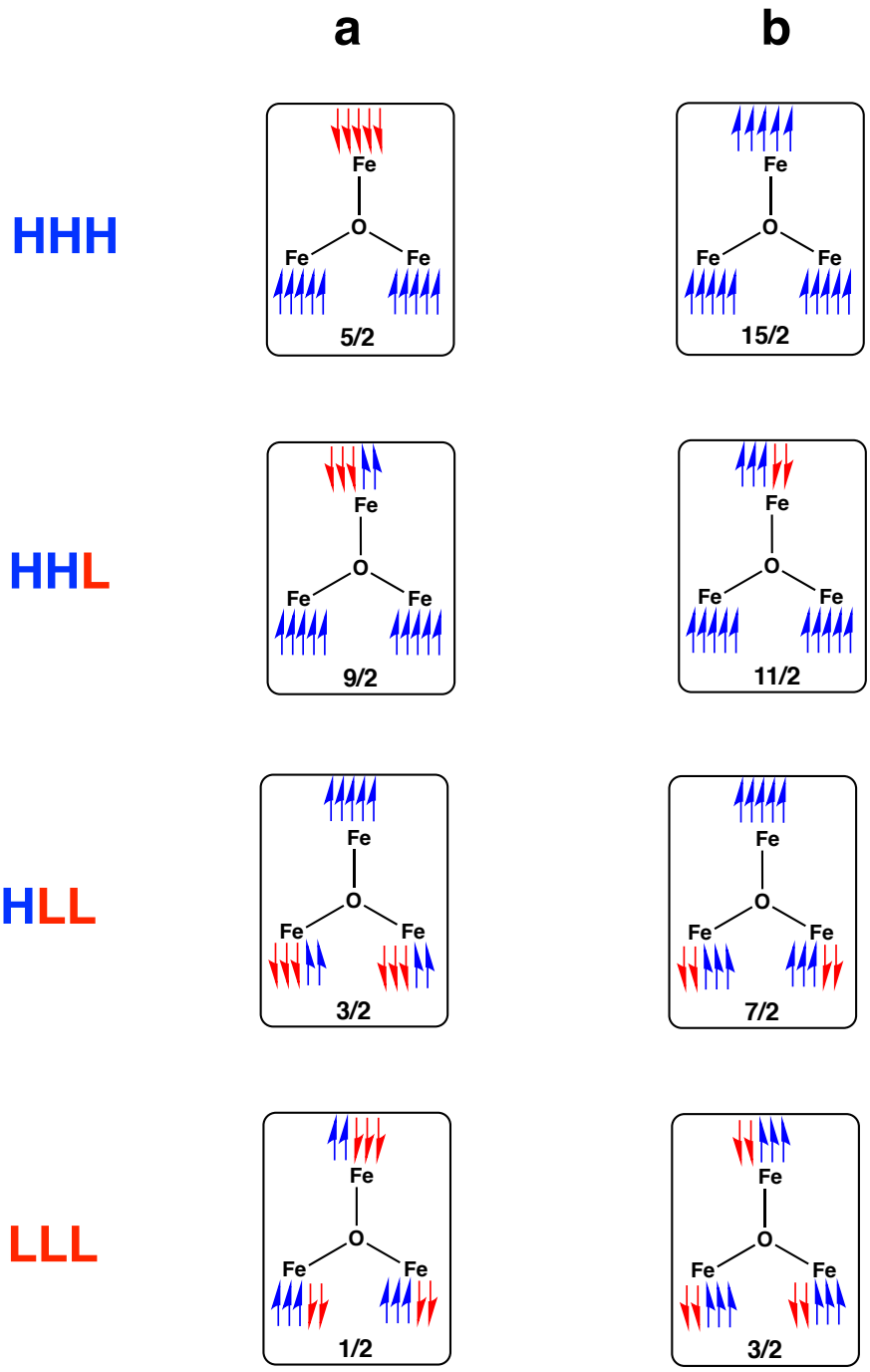


Figure 3.3: Possible configurations for the all-ferric spin state. (**a**) the antiferromagnetic (**b**) ferromagnetic states. The rows refer to the state of the three metal centres H means high spin while L means low spin. For example, the abbreviation HHL (High/High/Low) means two of the iron centres are high spin while the third ion is low spin. The fractional number under each structure refers to the M_S value.

Similarly, we can define F and AF coupled states for the intermediate HHL configuration with M_S = 11/2 and 9/2, respectively, and HLL, with M_S = 7/2 and 3/2, respectively. Each of the states identified in Figure 3.3

has a local configuration of either S = 5/2 or 1/2 at each iron centre, and should, therefore, be possible to locate.

This does indeed prove to be the case, and in every possible local combination, the antiferromagnetically coupled state proves to be substantially more stable than the ferromagnetic alternative (e.g for the states in Figure 3.3, our calculations using OPBE/TZP show that HHHa;5/2 (–519.25 eV) much lower than HHHb;15/2 (–518.68 eV), while LLLa;1/2 lower than LLLb;3/2 by ~0.3 eV). This is consistent with the well-established tendency for oxo-bridges to mediate strong antiferromagnetic coupling, but means in this case that we can safely ignore the ferromagnetic states as candidates for the ground states.

Moving to the mixed-valent states, we need to add an extra electron to the AF coupled states shown in column a of Figure 3.3 (column a of Figure 3.4). All possible combinations are shown in Figure 3.4. For the antiferromagnetic HHH coupled all-ferric state (with M_S = 5/2), an extra electron could in principle be added with spin α, in which case it must go to the Fe centre with spin β density (Figure 3.4, top left, HHHb), generating a configuration with M_S = 6/2. Alternatively, an extra electron with spin-β must go onto one of the two Fe centres which carry majority-spin (α) density, generating a configuration with M_S = 4/2. Similarly, for the other AF states of the all-ferric system (shown in column a of Figure 3.4), addition of a spin-α or spin-β electron generates states with different overall multiplicity. In all cases, we find that column c Figure 3.4, where the additional (spin-β) electron is delocalised over both Fe centres with majority-spin density is the most stable – this is an example of the double-exchange phenomenon, where an itinerant electron stabilises a local ferromagnetic coupling between the centres over which it can delocalise.

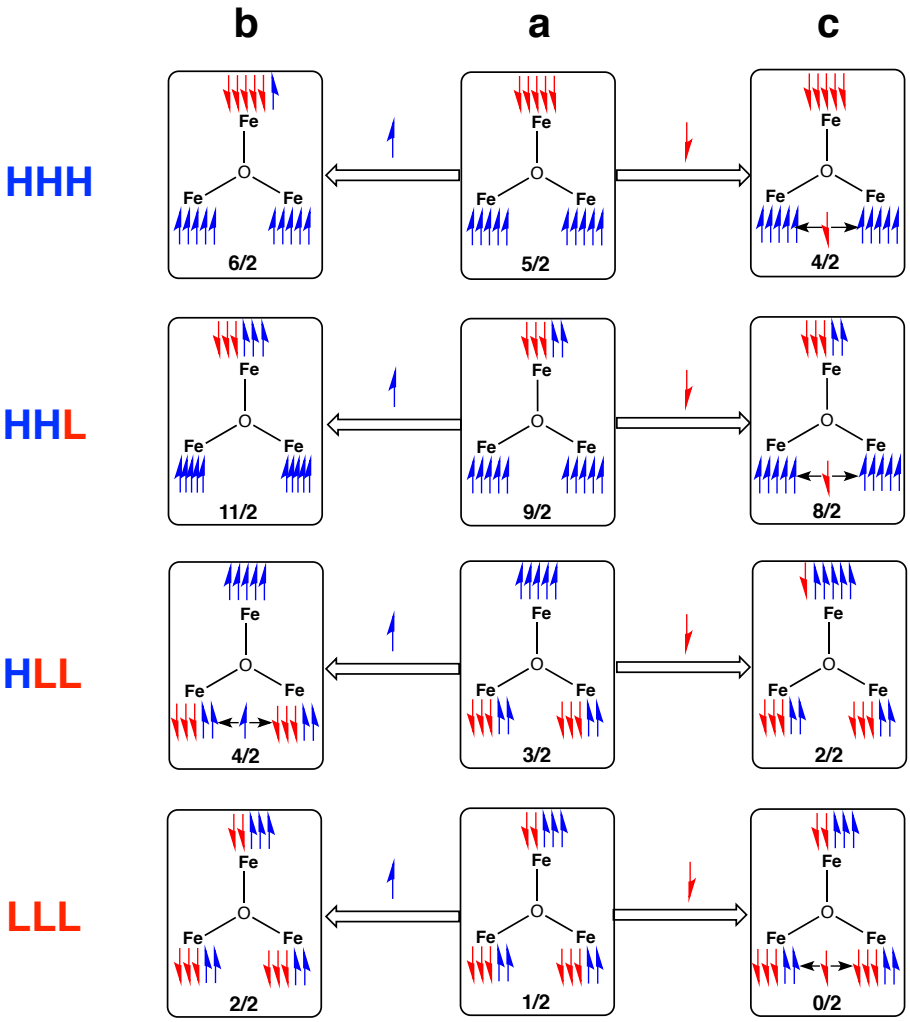


Figure 3.4: Possible configurations for the mixed valence broken symmetry states: adding an α (b) or β (c) extra electron generates different mixed valence states from the corresponding all-ferric ones(a). The fractional number under each structure refers to the M_S value.

We note that it is, in principle, possible that strong double exchange could stabilise the completely F state (column a of Figure 3.3) over the AF alternative: we have tested this possibility and the fully F configuration (S = 14/2 for the HHH case) remains substantially higher in energy. In the following discussion of all-ferric configurations, we focus on the AF coupled states shown in the column a of Figure 3.3 while for the mixed-valence states, we focus on the three, (HHH;**4/2**, HHL;**8/2**, LLL;**0/2**) states in column a and HLL;**4/2** state in column b of Figure 3.4, where the extra electron is added such that it reduces the total spin of the system.

3.3.2 Geometrical Evidence

Table 3.3 shows the optimised structural parameters for the M_S = 5/2 state (HHH configuration) for the all-ferric case and the S = 0/2 state (LLL configuration) for the mixed-valence case. These are compared to the crystallographic data for the all ferric $[Fe_3O(NCS)_3]^{2-}$ and the mixed valence $[Fe_3O(NCS)_3]^{2-}$ (crystallised in $[Fe_3O(NCS)_3][NEt_3H]_2$ and $[Fe_3O(NCS)_3][PPh_4][CoCp_2]$ respectively) that were shown in the introduction to this chapter.

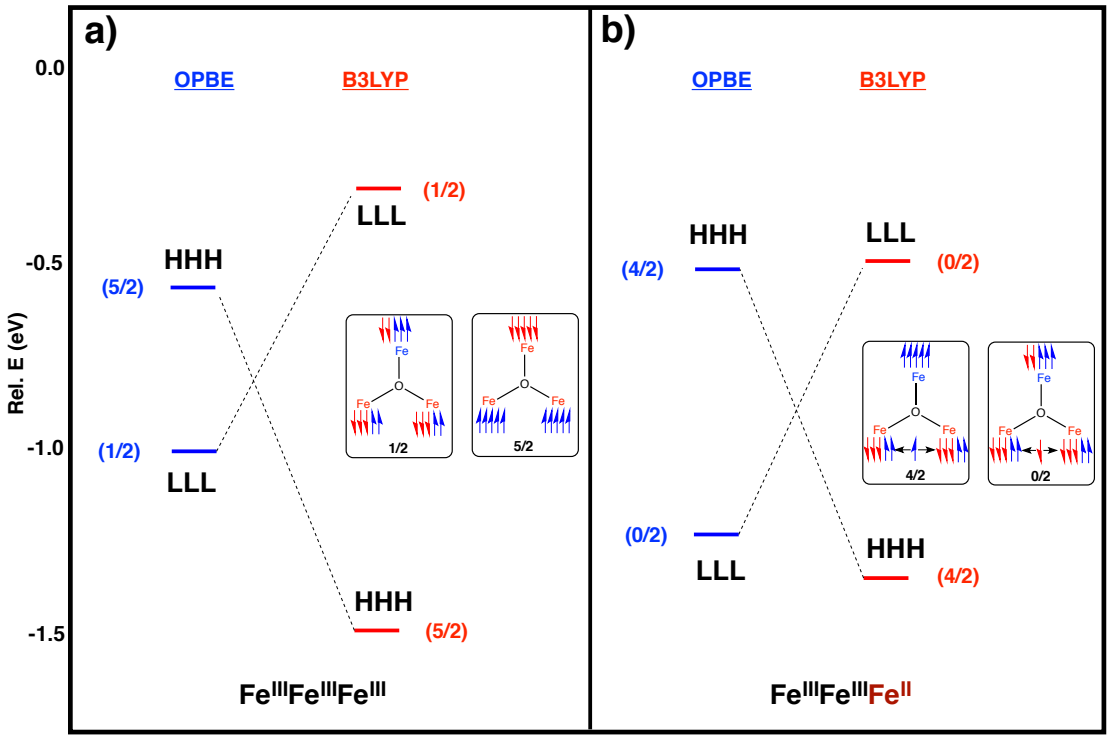
Table 3.2: The experimental and theoretical structural parameters for two oxidation states, all-ferric and mixed-valent(MV), of $[Fe_3O(NCS)_3]^z$ and $[Fe_3O(CN)_3]^z$ complexes: The computed spin state: all ferric; M_S = 5/2 and MV;M_S = 0/2 for $[Fe_3O(NCS)_3]^z$, while all ferric; M_S = 1/2 and MV;M_S = 0/2, for $[Fe_3O(CN)_3]^z$.

	Bond	**Tool**	**Fe_3^{III} (all ferric)**	**$Fe^{II}Fe_2^{III}$ (MV)**
$[Fe_3O(NCS)_3]^z$	Fe–O	X-ray	1.88	1.77
		B3LYP	1.90	1.78
		OPBE	1.90	1.75
	Fe–NCS	X-ray	1.98	1.94
		B3LYP	1.99	1.95
		OPBE	2.00	1.93
	Fe–N(Pz)	X-ray	2.15	1.97
		B3LYP	2.18	1.94
		OPBE	2.18	1.94
$[Fe_3O(CN)_3]^z$	Fe–O	X-ray	–	1.75
		B3LYP	1.78	1.79
		OPBE	1.96	1.76
	Fe–NCS	X-ray	–	1.98
		B3LYP	1.96	1.98
		OPBE	1.90	1.91
	Fe–N(Pz)	X-ray	–	1.93
		B3LYP	1.99	2.00
		OPBE	1.94	1.95

For the all-ferric case, the optimised bond lengths for the HHH M_S = 5/2 state are in excellent agreement with the X-ray data for $[Fe_3O(NCS)_3][NEt_3H]_2$: the Fe–O and Fe–NCS bond lengths are ~1.90 and ~2.0 Å, respectively while the Fe–N(Pz) bond lengths are longer at ~ 2.12 Å, similar to those reported in the Br and Cl capped analogues[22,24] The X-ray data for the mixed-valent anion in $[Fe_3O(NCS)_3][PPh_4][CoCp_2]_2$, in contrast, are a much better match to the M_S = 0/2 state of the LLL configuration (Figure 3.4, bottom right). The Fe–O and Fe-NCS bond lengths are both contracted significantly (~1.78 and ~1.95 Å, respectively), as are the Fe–N(Pz) bonds. For the purposes of calibration, we have also computed the structural parameters for the CN-capped analogue, where the mixed-valence M_S = 0/2 (LLL) state is again an excellent match to the X-ray data, in this case available only for the mixed-valence state.

3.3.3 Energies and Functional Dependence

Whilst the all-ferric HHH (M_S = 5/2) and mixed-valence LLL (M_S = 0/2) states appear to show good agreement with the X-ray data for the di- and trianionic clusters ions, respectively, it is not clear that these are necessarily computed to be the most stable spin states of the system. To illustrate this point, Figure 3.5(a) shows the relative energies of all-ferric HHH M_S = 5/2, and LLL M_S = 1/2 states computed with two different DFT functionals OPBE and B3LYP, both of which have been used extensively by various authors in the spin crossover literature (*ca.* section 2.12).


a)
b)
OPBE
B3LYP
OPBE
B3LYP
0.0
-0.5
-1.0
-1.5
Rel. E (eV)
HHH
(5/2)
LLL
(1/2)
(1/2)
LLL
HHH
(5/2)
1/2
5/2
Fe
O
Fe
Fe
Fe

extensive debate for many years, with various claims being made for gradient-corrected, hybrid and even double hybrid functionals.[39, 45, 47, 49-52]

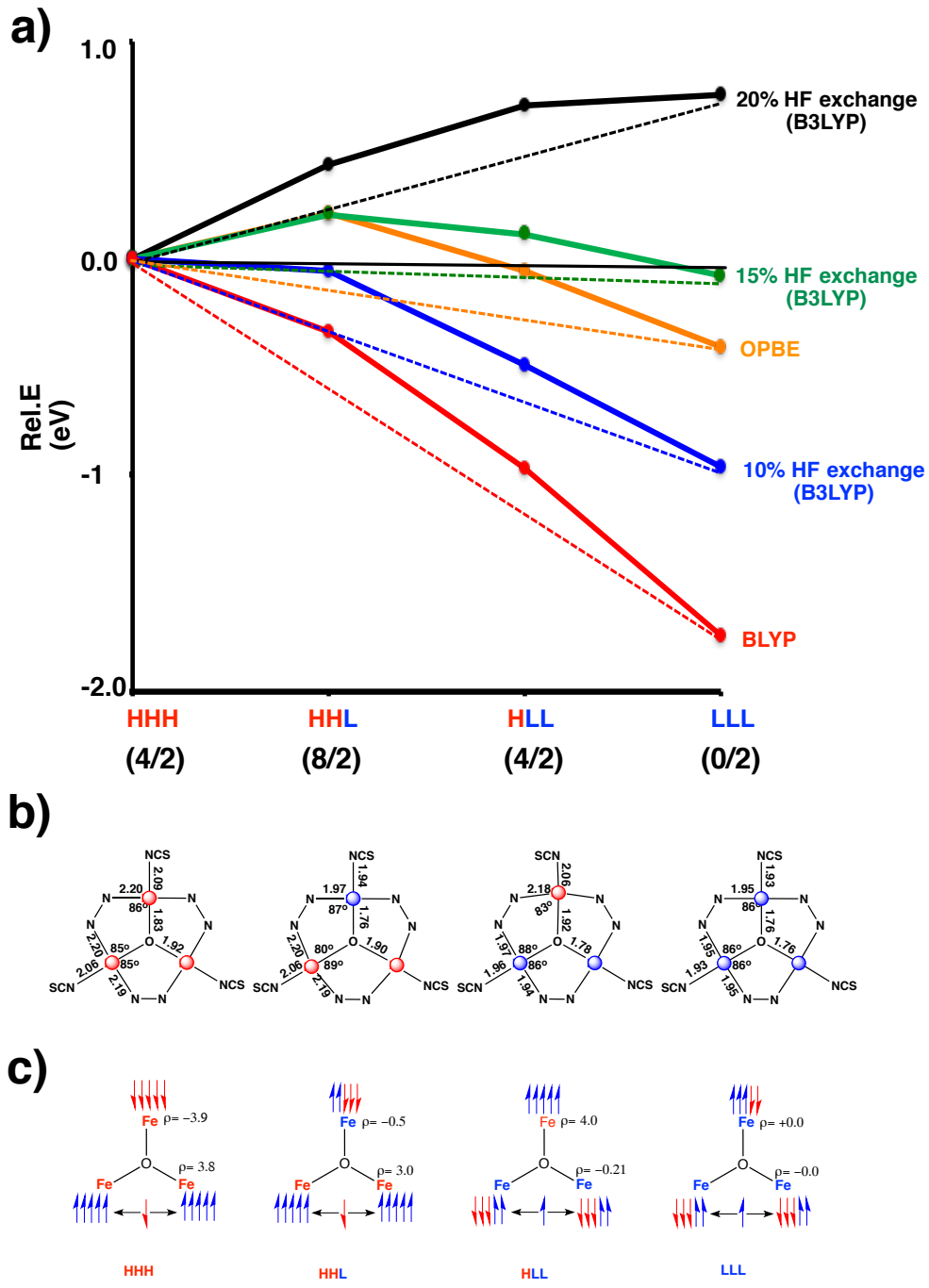


Figure 3.6: (a) Relative energy of all-ferric pyrazolato complex $[Fe_3O(NCS)_3]^{3-}$ against number of high spin centres of the fours spin-states (HHH;4/2, HHL,8/2, HLL; 4/2, LLL; 0/2). The points in the curve are calculated using GGA (BLYP OPBE), and hybrid/B3LYP functional with 10%, 15% and 20% of Hartree-Fock exchange. (b) The structural parameters and the spin configuration on each Fe ion calculated using OPBE/TZP model. (c) scheme of broken symmetry states showed the delocalisation of the additional electron on Fe_2 dimers and Mulliken spin densities on each Fe ions generated using the same model. The number below the x-axis represent the M_S values of each spin state.

In order to explore this phenomenon in more detail, we have computed the energies of the HHH and LLL configurations for the mixed-valent species, and also the intermediate HHL and HLL cases, using a range of functionals based on the BLYP family, along with the OPBE functional used so far with different amounts of Hartree-Fock exchange (Figure 3.6a). In the figure, the x-axis corresponds to an increasing number of locally low-spin metal ions, from HHH on the left to LLL on the right.

The B3LYP functional contains a 20% admixture of Hartree-Fock exchange and the black line reflects the energies shown in Figure 3.6a, with the HHH configuration (for left) below the LLL case (for right). As the amount of Hartree-Fock exchange is reduced to 15%, 10%, and 0% (BLYP), the LLL configuration is progressively stabilised, such that it becomes the ground state (consistent with experiment) for functionals with less than ~17%. Reiher has previously recommended 15% for spin crossover cases in his B3LYP* functional,[53] which falls just below this threshold. The corresponding data for the carboxylate analogues is shown in Figure 3.7, where the HHH configuration proves to be the most stable, regardless of functional. The greater tendency to adapt HS configuration for the carboxylate is consistent with the available experimental data, where no evidence for a spin crossover has been reported.

Despite the strong functional dependence of the relative energies of the HHH and LLL spin states Figure 3.6a, one critical point is true for all functionals: the intermediate HHL and HLL configurations always lie above the trendline joining the HHH and LLL limits.

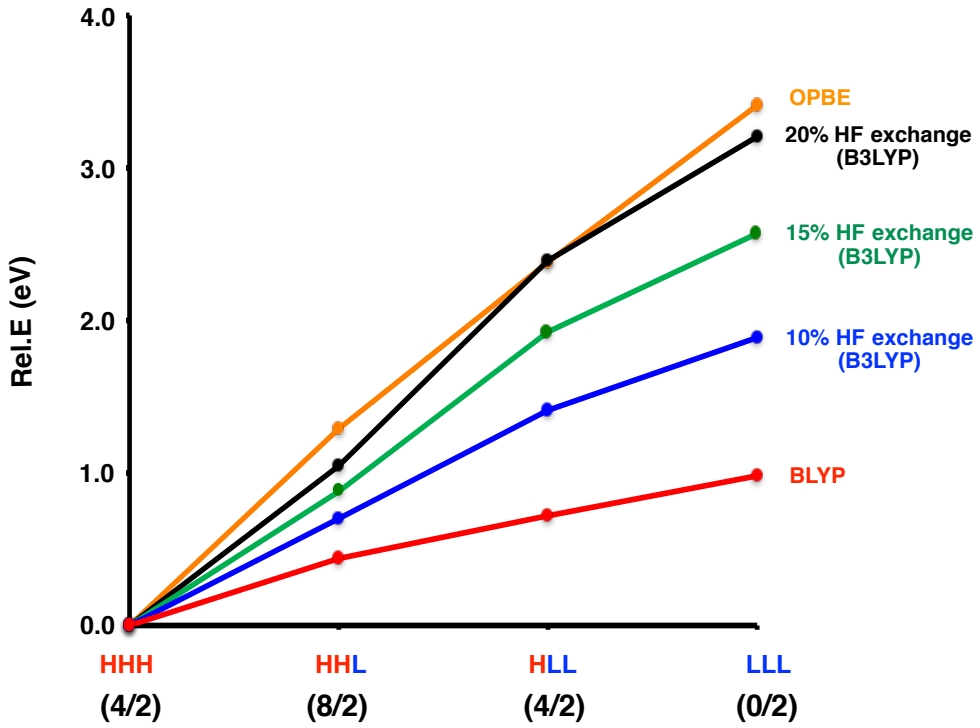


Figure 3.7: Relative energy of all-ferric carboxylate $[Fe_3O(OOCH)_6(NCS)_3]^{3-}$(against number of high spin centres of the fours spin-states (HHH;4/2, HHL,8/2, HLL; 4/2, LLL; 0/2). The points in the curved calculated using GGA (BLYP and OPBE), and HYBRID/B3LYP functional with 10%, 15% and 20% of Hartree-Fock exchange. The number below the x-axis represent the M_S values of each spin state.

In thermodynamic terms, this means that these intermediate states are intrinsically unstable with respect to decomposition to a mixture of the HHH and LLL states. This observation immediately rationalises the cascade nature of the redox event, where all three centres undergo simultaneous spin crossover rather than only one. To understand how the SCO propagates from one centre to another, we can return to the arguments made by Borshch and co-workers regarding ligand strain. In Figure 3.6b, both HHH and LLL configurations have uniform M-L bond lengths (shorter in the latter) and, most importantly, the N-Fe-N angles are all close to 90°. In contrast, in the two intermediates states, the geometrical environments around the LS centres is as symmetric as those in LLL, but the coordination sphere of the HS centres are noticeably distorted, with acute O-Fe-N angles in the range of 81° – 83°. The greater distortion of the HS centres is a result of the lack of ligand field stabilization, which

leads to a more flexible coordination environment. At low-spin centres, in contrast, the ligand-field stabilisation is substantial, imposing on almost-perfect octahedral environment, consequently and therefore less flexible coordination around the metal.

3.3.4 Analysis of the ^{57}Fe Mössbauer Spectroscopy

The discussion presented so far has been guided by a comparison with the crystallographic data for both the all-ferric and the mixed-valent species. It is important to note, however, that the crystal structure of $[Fe_3O(NCS)_3][PPh_4][CoCp_2]_2$ was obtained only after the majority of this work had been completed. At the outset, only spectroscopic data (Mössbauer, IR) were available to support the assertion of a LLL configuration for the mixed-valent species, and so much of our effort was dedicated to analysing these spectroscopic signatures and proving that they were indeed evidence for the spin crossover. These studies became relatively less important when definitive structural evidence became available, but nevertheless the results are summarised in the following section.

^{57}Fe Mössbauer spectroscopy is a standard technique used to study the electronic structure of iron-containing compounds, including proteins, and biologically important inorganic molecules.[36] In the context of spin crossover, Mössbauer spectroscopy is very useful because the characteristic spectrum is very sensitive to slight changes in the electron density around the resonant nucleus. The Mössbauer signal gives information about both the oxidation state and the symmetry of the coordination environment. Mössbauer spectroscopy will also be an important tool in our discussion of enneanuclear $Fe_{9-x}Ni_x$ clusters to be presented in Chapter 5, so a brief description of the physical process will be presented here before we discuss the results.

A schematic Mössbauer spectrum is shown in Figure 3.8, where the y-axis represents the transmitted γ-ray intensity while the x-axis corresponds to the γ-source speed in units of mm/s. Unless the source and absorber are identical, the peaks are shifted from the origin at 0 mm/s. The peak shift is defined the isomer shift (δ), the position of the barycentre of the doublet along the x axis. The isomer shift originates from s electron density at the nuclei, and any changes in the s-electron density at the nuclei of the sample, due to an electrostatic disturbance by the surrounding valence electrons or the bonded ligands, leads to small differences between the source and the absorbed nucleus. This in turn produces a positive or negative shift from the center of the spectrum. The isomer shift gives useful information about the electronic environment. For example, Fe^{II} ions typically have a larger isomer shift than Fe^{III} ions, simply because the number of electrons that screen the γ radiation in Fe^{II} is larger.

The two peaks in a Mössbauer spectrum appear as doublets, the separation of which is called the Quadrupole Splitting (ΔE_Q). This is determined by the occupancy of the d orbitals and also by the identity and arrangement of ligands around the metal. The origin of the quadrupole splitting lies in the angular momentum quantum number of the nucleus, I . If I is larger than 1/2 , (2I+1) substates split in the presence of an electric field on the nucleus. Figure 3.8 shows an example of nuclei with I = 3/2 (e.g ^{57}Fe or ^{119}Sn) when the excited state splits into two sublevels (m_I = ±1/2 and m_I = ±3/2). A typical spectrum for an isolated Fe nucleus consists of a pair of peaks arising from the transition from the I = 1/2 ground state of the nucleus to the m_I = +1/2 and m_I = +3/2 components of the I = 3/2 excited state.

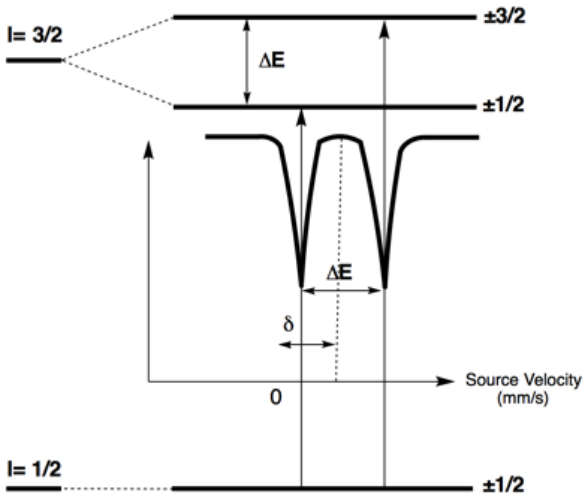


Figure 3.8: schematic representation of Mössbauer spectrum for atom with nuclei spin *I* = 3/2, where *I*, corresponds to the nuclear spin, while $\boldsymbol{\Delta E}$ and $\boldsymbol{\delta}$ represents quadrupole splitting, and isomer shift respectively

The high energy of the γ-rays results in very high resolution (typically 1:10^{12}) allowing for the detection of very small changes. Mössbauer spectroscopy has been widely used to study the electronic and magnetic properties of trinuclear compounds[54-56] such as the all-ferric $[Fe_3^{III}O(OOCR)_3X_3]$ species, where all the three irons have identical electronic environments. More importantly in the present context, ^{57}Fe Mössbauer spectroscopy is used extensively to explore the nature of electron trapping/detrapping in tri-iron mixed valence triangles, as distinguishing between Fe^{II} and Fe^{III} is very straightforward.[21, 57] For example, in clusters of the general type $[Fe_3^{III}O(OOCR)_3X_3]$, the low temperature (10 K) spectrum features two doublets with very different isomer shifts and quadrupole splittings, corresponding to Fe^{III} ($\delta \sim 0.4 - 0.55$ mm/s, $\Delta E_Q \sim 0.97 - 1.2$ mm/s and Fe^{II} ($\rho \sim 1.0 - 1.3$ mm/s , $\Delta E_Q \sim 1.6 - 2.8$ mm/s). At higher temperatures, the two doublets merge, giving a single doublet with parameters corresponding to the average of the two ($\rho \sim 0.5 - 0.7$ mm/s $\Delta E_Q \sim 0.2 - 1.0$ mm/s). At these elevated temperatures, electron hopping between the three metal centres is faster than the typical Mössbauer timescale of ~10^{-7} s.

The measured Mössbauer spectra of all-ferric $[Fe_3O(NCS)_3]^{2-}$ and mixed-valent $[Fe_3O(NCS)_3]^{3-}$ are shown in Figure 3.9 (blue and red, respectively). The corresponding parameters are collected in Table 3.2, alongside the DFT-computed values. There is clearly a distinct shift in both the isomer shift and the quadrupole splitting upon reduction (blue to red), but no evidence for splitting of the peaks that would suggest localisation.

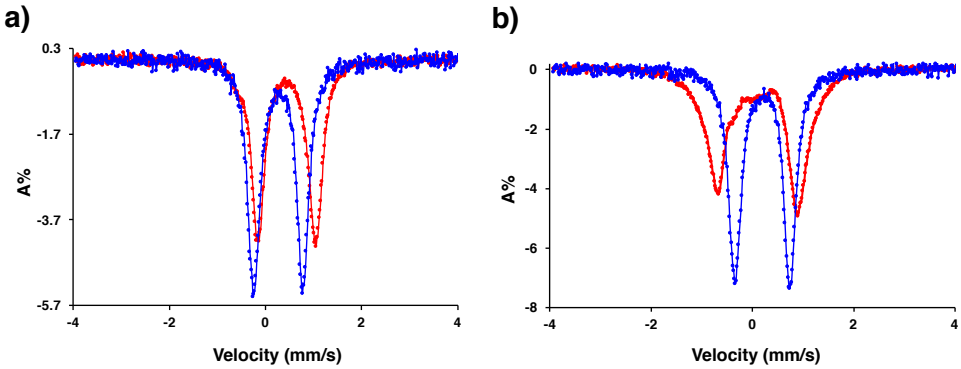


Figure 3.9: Experimental Mössbauer spectra at 80 K: the blue to all ferric oxidation states while the red peaks refer to mixed-valent form; (**a**) $[Fe_3O(NCS)_3]^{2-/3-}$, (**b**) $[Fe_3O(CN)_3]^{2-/3-}$.

The corresponding spectra are also shown for the CN^- capped species. Whilst the spectra of the CN^- and NCS^- species are superficially similar, there are some conspicuous differences. In the NCS^- case the isomer shift moves to lower values upon reduction (0.443 to 0.271) while in the CN^- case, the opposite is true (0.108 to 0.199), although the differences are small. More obviously, while the quadrupole splitting is approximately constant for the two oxidation states of the NCS^- system, it is substantially larger in the reduced CN^- complex.

In Table 3.3, the computed Mössbauer parameters are presented for spin states of both the HHH and LLL configurations. For the all-ferric cases, M_S = 5/2 and 1/2 these correspond to HHH and LLL, respectively. For the mixed-valent cases, the HHH configuration has M_S = 4/2 while the LLL configuration has 0/2. The absolute value of

the computed isomer shift is of limited value because it depends critically on the intercept of the calibration curve described in the methodology section (and experimentally, on the value for the reference, bulk iron). Thus we focus on changes in the isomer shift rather than the absolute values. The quadrupole shift, in contrast, is not dependent on any reference, and so a more direct correspondence between experiment and theory can be anticipated.

Table 3.3: the experimental and computed Mössbauer parameters quadrupole splitting, ΔE_Q (mm/s), and isomer shift, δ (mm/s), for the antiferromagnetic states of all-ferric and mixed-valence oxidation states.

		All ferric			Mixed-valent		
		M_S	δ	ΔE_Q	M_S	δ	ΔE_Q
$[Fe_3O(CN)_3]$	**Exp.**	**-**	**0.108**	**1.610**	**-**	**0.199**	**1.087**
	Calc.	1/2	0.680	1.946	0/2	0.733	1.215
		5/2	1.072	0.652	4/2	1.218	2.087
$[Fe_3O(NCS)_3]$	**Exp.**	**-**	**0.443**	**1.193**	**-**	**0.271**	**1.023**
	Calc.	1/2	0.758	1.987	0/2	0.812	0.975
		5/2	1.163	1.174	4/2	1.289	1.894

If we look first at the CN^- data we see that the key experimental trends are replicated only if the LLL configuration is the ground state for both oxidation states (1/2 or 0/2): the isomer shift is larger in the reduced from and the quadrupole splitting significantly smaller. In the corresponding data for the HHH configurations, ΔE becomes dramatically larger in the reduced species, entirely inconsistent with experiment. Turning to the NCS-capped species, the computed parameters show very similar patterns to those for the CN-capped analogues: if no change in spin state occurs, we would therefore predict a marginal increase in both the isomer shift and in the quadrupole splitting which is not what is observed experiemntally. Only if there is a switch from HHH to LLL upon reduction can we replicate the experimentally observed decrease in both parameters (δ goes from 1.163 mm/s (M_S = 5/2) to 0.812

mm/s (M_S = 0/2), ΔE_Q from 1.174 mm/s to 0.975 mm/s). In summary, then, we conclude that the Mössbauer spectra are consistent only with a transition from HHH to LLL configurations upon one-electron reduction, as was confimred later by X-ray crystallography.

3.3.5 Infrared (IR) Spectroscopy

IR spectroscopy is one of the most commonly used techniques in chemistry because different functional groups vibrate at characteristic frequencies. Many studies of transition metal complexes focus on the far-IR region, where metal-ligand stretches and bends are typically found. Changes in the characteristic frequencies of the ligands can also be influenced by the oxidation state of the metal (most famously in the CO stretch of carbonyls, but in this case the N-C stretch of the NCS ligand is a useful fingerprint). In order to establish the key features of the spectrum, we first present a comparison between the computed vibrational spectra of the all-ferric carboxylate and pyrazolate complexes, $[Fe_3(\mu_3\text{–}O)(OOCH)_6(NCS)_3]^{2-}$ (Figure 3.10 bottom) and , $[Fe_3(\mu_3\text{–}O)(NO_2\text{–}Pz)_6(NCS)_3]^{2-}$ ($[Fe_3O(NCS)_3]^2$) (Figure 3.10 top). The peaks that appears in the 800-2000 cm^{-1} window correspond to the vibrational modes of OCO and pyrazolato fragments. The symmetric OCO stretching, for example, appears at 1370 cm^{-1}, and the position of this peak is useful for tracking changes in oxidation state in these complexes.[2, 58] The vibrational frequencies for M_3OX_3 units appear around 400 cm^{-1}, the most significant of which is the doubly degenerate Fe–O asymmetric stretch, labelled 1c/2c and 1p/2p in the carboxylate and pyrazolate spectra, respectively. The two components are degenerate only in the limit of perfect D_{3h} symmetry, and the splitting of the band is diagnostic of reduction in symmetry caused by electron localisation.[16]

The most useful peaks in the present context are, however, the very intense N-C vibrational modes that appear around 2000 cm^{-1} (labelled 6c and 8p, respectively). In D_{3h} symmetry there are two modes, the totally symmetric a_1' and doubly degenerate e', but only the latter is active in the infrared.

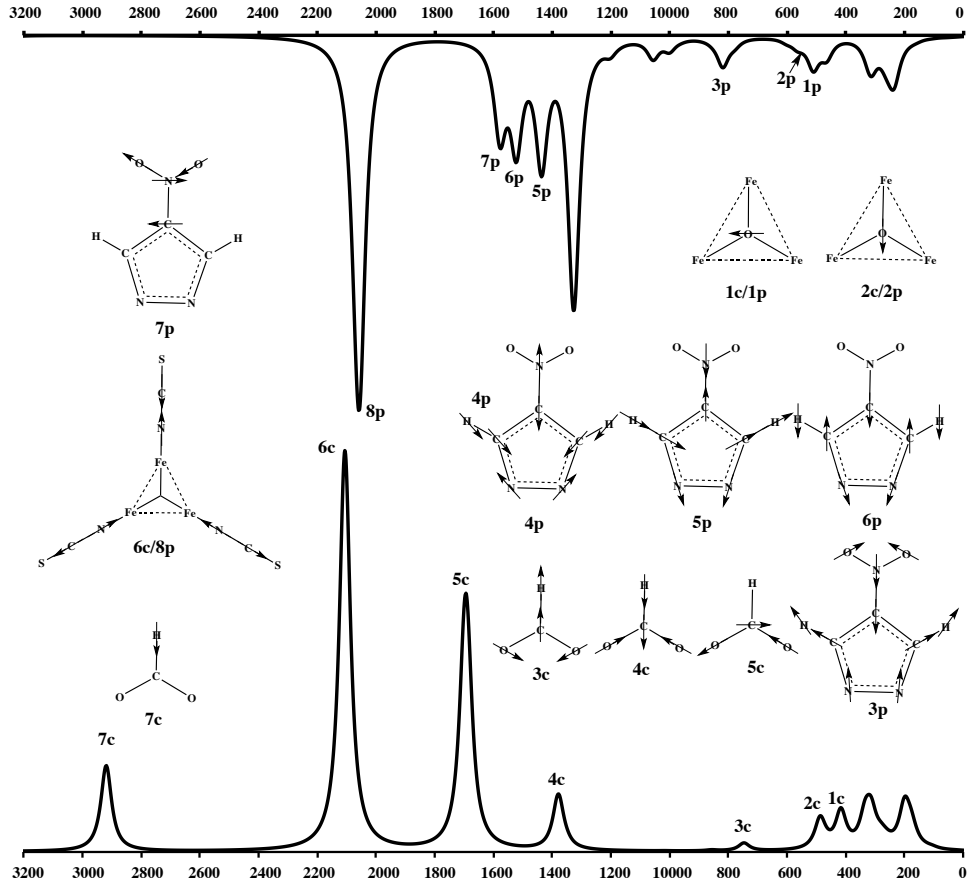


Figure 3.10: Computed vibrational spectra and the some of their normal modes, of C_{2V} tri-iron complexes: (**bottom**) $[Fe_3(\mu_3\text{–}O)(OOCH)_6(NCS)_3]^{2-}$. (**top**), $[Fe_3(\mu_3\text{–}O)(NO_2\text{–}Pz)_6(NCS)_3]^{2-}$ ($[Fe_3O(NCS)_3]^{2-}$).

Figure 3.11 shows the experimental vibrational spectrum of $[Fe_3O(NCS)_3]^z$, in the both the all ferric (z = 2–, blue) and mixed-valence (z = 3–, red) states, in the range 450 – 3500 cm^{-1}. The computed spectra for the HHH configuration of the all-ferric case (M_S = 5/2), and the LLL configuration of the mixed-valent form (M_S = 0/2) are shown for comparison. The resonances around 1500 cm^{-1} characteristic of the pyrazolate ring

are relatively unaffected by change in oxidation state, while the potentially informative Fe–O stretches at ~400 cm^{-1} are beyond the detection limit of 450 cm^{-1}. We therefore focus on the CN^-stretching region around 2000 cm^{-1}. Experimentally, this band is blue shifted by 64 cm^{-1} upon reduction, from 2017 cm^{-1} in the all-ferric form to 2081 cm^{-1} in the mixed-valent analogue. The same trend one can see in the theoretical spectra, with the computed asymmetric C–N stretch shifting by 59 cm^{-1} from 2056 cm^{-1} to 2115 cm^{-1}.

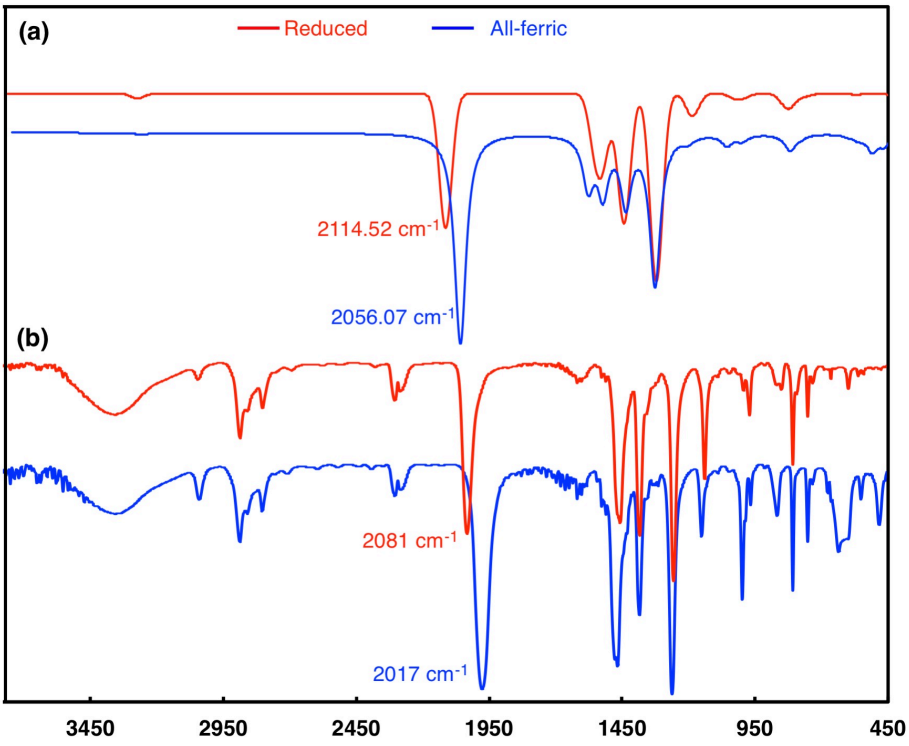


Figure 3.11: Infrared Spectra of $[Fe_3O(NCS)_3]^z$: all-ferric (z = 2–, **blue**) and mixed valence (z = 3–, **red**) spectra: (**a**) the computed spectrum with DFT/OPBE the spectrum with DFT/OPBE correspond to S = 5/2 and M_S = 0/2 states respectively. **(b**) the experimental FTIR spectrum.

Simple arguments based on back-bonding would suggest that the one-electron reduction should lead to the opposite trend *i.e.* a red shift in the C–N vibration, and indeed if we compute the IR spectrum for the HHH configuration of the mixed-valent species (*i.e.* reduction without spin crossover), we find that the C–N stretch is shifted marginally lower in frequency. Thus, it appears that the substantial blue shift in the

C–N stretch is indeed highly characteristic of spin crossover, we note that it has also been observed in $[Fe(phen)_2(NCS)_2]$, where the blue shift is around 60 cm^{-1} for the HS→LS transition. Just like the MB data, our computational analysis confirms that the changes in the IR spectra are entirely consistent with the proposal that all the three Fe centres undergo spin crossover upon one-electron reduction.

3.4 Conclusions

In this chapter, we have explored the electronic structure of a new class of $[Fe_3O(NCS)_3]^z$ triangle in both its all-ferric (z = 2–) and mixed-valent forms (z = 3–). This cluster differs from the well-known carboxylate analogues in that one-electron reduction results in a spin crossover from high- to low-spin at all three metal centres – an unprecedented example of a 'redox cascade'. Our computational work complements crystallography and Mössbauer and IR spectroscopies, providing a consistent picture of the electronic structure changes that take place upon reduction. Our analysis of the structural and spectroscopic data shows that they are consistent only with a spin crossover cascade – the alternative scenario where redox events occur without changes in spin state cannot account for the observed trends. The spin-state energetics remain a challenge for DFT, and the relative energies of the HHH and LLL configurations is strongly dependent on functional, with hybrids such as B3LYP favouring the former. Nevertheless, we can show that the intermediate HHL and HLL states are intrinsically unstable with respect to the HHH and LLL limits, irrespective of the functional used, and this accounts for the cascade nature of the redox event. The instability of the intermediate configurations can be linked to the strong binding of the cluster by the oxo-bridge, which means that characteristic changes in the bond length

at one centre are transmitted to the other two, destabilising them and favouring the further spin crossover.

3.5 References

[1] E. V. Govor, K. Al-Ameed, I. Chakraborty, C. S. Coste, O. Govor, Y. Sanakis, J. E. McGrady and R. G. Raptis, *Angewandte Chemie International Edition* **2017**, *56*, 582-586.

[2] R. D. Cannon and R. P. White, *Progress in Inorganic Chemistry* **1988**, *36*, 195-298.

[3] R. F. Weinland, *Chemiker Zeitung* **1908**, *32*, 812.

[4] R. F. Weinland, *Berichte der Deutschen Chemischen Gesellschaft* **1908**, *41*, 3236.

[5] A. Werner, *Berichte der Deutschen Chemischen Gesellschaft* **1908**, *41*, 2110.

[6] L. A. Welo, *Philosophical Magazine* **1928**, *6*, 481-509.

[7] L. A. Welo, *Physical Review* **1928**, *32*, 320.

[8] L. E. Orgel, *Nature* **1960**, *187*, 504-505.

[9] B. N. Figgis and G. B. Robertson, *Nature* **1965**, *205*, 694-695.

[10] H.-C. Yao, J.-J. Wang, Y.-S. Ma, O. Waldmann, W.-X. Du, Y. Song, Y.-Z. Li, L.-M. Zheng, S. Decurtins and X.-Q. Xin, *Chemical Communications* **2006**, 1745-1747.

[11] C. Benelli, S. Parsons, G. A. Solan and R. E. P. Winpenny, *Angewandte Chemie-International Edition in English* **1996**, *35*, 1825-1828.

[12] S. Karmakar and A. Chakravorty, *Inorganic Chemistry* **1996**, *35*, 1935-1939.

[13] P. Stavropoulos, R. Çelenligil-Çetin and A. E. Tapper, *Accounts of Chemical Research* **2001**, *34*, 745-752.

[14] D. H. R. Barton, J. Boivin, D. Crich and C. H. Hill, *Journal of the Chemical Society-Perkin Transactions 1* **1986**, 1805-1808.

[15] D. H. Doff, N. H. J. Gangas, J. E. M. Allan and J. M. D. Coey, *Clay Minerals* **1988**, *23*, 367-377.

[16] R. W. Wu, M. Poyraz, F. E. Sowrey, C. E. Anson, S. Wocadlo, A. K. Powell, U. A. Jayasooriya, R. D. Cannon, T. Nakamoto, M. Katada and H. Sano, *Inorganic Chemistry* **1998**, *37*, 1913-1921.

[17] T. Nakamoto, M. Hanaya, M. Katada, K. Endo, S. Kitagawa and H. Sano, *Inorganic Chemistry* **1997**, *36*, 4347-4359.

[18] T. Sato, F. Ambe, K. Endo, M. Katada, H. Maeda, T. Nakamoto and H. Sano, *Journal of the American Chemical Society* **1996**, *118*, 3450-3458.

[19] C. C. Wu, S. A. Hunt, P. K. Gantzel, P. Gutlich and D. N. Hendrickson, *Inorganic Chemistry* **1997**, *36*, 4717-4733.

[20] C. Stadler, J. Daub, J. Kohler, R. W. Saalfrank, V. Coropceanu, V. Schunemann, C. Ober, A. X. Trautwein, S. F. Parker, M. Poyraz, T. Inomata and R. D. Cannon, *Journal of the Chemical Society, Dalton Transactions* **2001**, 3373-3383.

[21] J. Overgaard, E. Rentschler, G. A. Timco, N. V. Gerbeleu, V. Arion, A. Bousseksou, J. P. Tuchagues and F. K. Larsen, *Journal of the Chemical Society, Dalton Transactions* **2002**, 2981-2986.

[22] W. M. C. Sameera, D. M. Pinero, R. Herchel, Y. Sanakis, J. E. McGrady, R. G. Raptis and E. M. Zueva, *European Journal of Inorganic Chemistry* **2012**, 3500-3506.

[23] H. N. Miras, I. Chakraborty and R. G. Raptis, *Chemical Communications* **2010**, *46*, 2569-2571.

[24] D. Pinero, P. Baran, R. Boca, R. Herchel, M. Klein, R. G. Raptis, F. Renz and Y. Sanakis, *Inorganic Chemistry* **2007**, *46*, 10981-10989.

[25] L. Cambi and L. Szegö, *Berichte der deutschen chemischen Gesellschaft (A and B Series)* **1931**, *64*, 2591-2598.

[26] L. Cambi and L. Malatesta, *Berichte der deutschen chemischen Gesellschaft (A and B Series)* **1937**, *70*, 2067-2078.

[27] S. N. Datta, C. O. Trindle and F. Illas, *Theoretical and computational aspects of magnetic organic molecules*, Imperial College Press, London, **2014**, p. 1-335.

[28] P. Gütlich and H. Goodwin, *Topics in Current Chemistry* **2004**, *233*, 1-47.

[29] J. A. Real, H. Bolvin, A. Bousseksou, A. Dworkin, O. Kahn, F. Varret and J. Zarembowitch, *Journal of the American Chemical Society* **1992**, *114*, 4650-4658.

[30] S. Zein and S. A. Borshch, *Journal of the American Chemical Society* **2005**, *127*, 16197-16201.

[31] A. Y. Verat, N. Ould-Moussa, E. Jeanneau, B. Le Guennic, A. Bousseksou, S. A. Borshch and G. S. Matouzenko, *Chemistry-a European Journal* **2009**, *15*, 10070-10082.

[32] E. M. Zueva, E. R. Ryabikh and S. A. Borshch, *Inorganic Chemistry* **2011**, *50*, 11143-11151.

[33] E. M. Zueva, E. R. Ryabikh, A. M. Kuznetsov and S. A. Borshch, *Inorganic Chemistry* **2011**, *50*, 1905-1913.

[34] Y. Qi, E. W. Müller, H. Spiering and P. Gütlich, *Chemical Physics Letters* **1983**, *101*, 503-505.

[35] R. Mössbauer, *Zeitschrift für Physik* **1958**, *151*, 124-143.

[36] Q. J. Lawrence, *Physical methods in bioinorganic chemistry spectroscopy and magnetism*, University Science Books, Sausalito (Calif.), **2000**, p. 1-556.

[37] P. Harding, D. J. Harding, R. Daengngern, T. Thurakitsaree, B. M. Schutte, M. J. Shaw and Y. Tantirungrotechai, *Polyhedron* **2012**, *42*, 291-301.

[38] G. te Velde, F. M. Bickelhaupt, E. J. Baerends, C. Fonseca Guerra, S. J. A. van Gisbergen, J. G. Snijders and T. Ziegler, *Journal of Computational Chemistry* **2001**, *22*, 931-967.

[39] S. Zein, S. A. Borshch, P. Fleurat-Lessard, M. E. Casida and H. Chermette, *Journal of Chemical Physics* **2007**, *126*.

[40] A. Klamt and G. Schuurmann, *Journal of the Chemical Society, Perkin Transactions 2* **1993**, 799-805.

[41] S. H. Vosko, L. Wilk and M. Nusair, *Canadian Journal of Physics* **1980**, *58*, 1200-1211.

[42] J. P. Perdew, J. A. Chevary, S. H. Vosko, K. A. Jackson, M. R. Pederson, D. J. Singh and C. Fiolhais, *Physical Review B* **1992**, *46*, 6671-6687.

[43] W. G. Han, T. Liu, T. Lovell and L. Noodleman, *J Comput Chem* **2006**, *27*, 1292-1306.

[44] V. Arcisauskaite, D. Fijan, M. Spivak, C. d. Graaf and J. E. McGrady, *Physical Chemistry Chemical Physics* **2016**, *18*, 24006-24014.

[45] M. Swart, *International Journal of Quantum Chemistry* **2013**, *113*, 2-7.

[46] A. Droghetti, D. Alfè and S. Sanvito, *Physical Review B* **2013**, *87*, 205114.

[47] J. N. Harvey in *DFT Computation of Relative Spin-State Energetics of Transition Metal Compounds*, Springer Berlin Heidelberg, Berlin, Heidelberg, **2004**, pp. 151-184.

[48] Y. Shao, M. Head-Gordon and A. I. Krylov, *The Journal of Chemical Physics* **2003**, *118*, 4807-4818.

[49] A. Domingo, M. Àngels Carvajal and C. de Graaf, *International Journal of Quantum Chemistry* **2010**, *110*, 331-337.

[50] M. Kepenekian, V. Robert, B. Le Guennic and C. De Graaf, *Journal of Computational Chemistry* **2009**, *30*, 2327-2333.

[51] H. Paulsen and A. X. Trautwein in *Density Functional Theory Calculations for Spin Crossover Complexes*, Springer Berlin Heidelberg, Berlin, Heidelberg, **2004**, pp. 197-219.

[52] A. Ghosh and P. R. Taylor, *Current Opinion in Chemical Biology* **2003**, *7*, 113-124.

[53] M. Reiher, O. Salomon and B. Artur Hess, *Theoretical Chemistry Accounts* **2001**, *107*, 48-55.

[54] B. P. Baranwal, S. S. Das, T. Gupta and A. K. Singh, *Progress in Crystal Growth and Characterization of Materials* **2002**, *45*, 147-153.

[55] J. Catterick, P. Thornton and B. W. Fitzsimmons, *Journal of the Chemical Society-Dalton Transactions* **1977**, 1420-1425.

[56] A. N. Georgopoulou, Y. Sanakis, V. Psycharis, C. P. Raptopoulou and A. K. Boudalis, *Hyperfine Interactions* **2010**, *198*, 229-241.

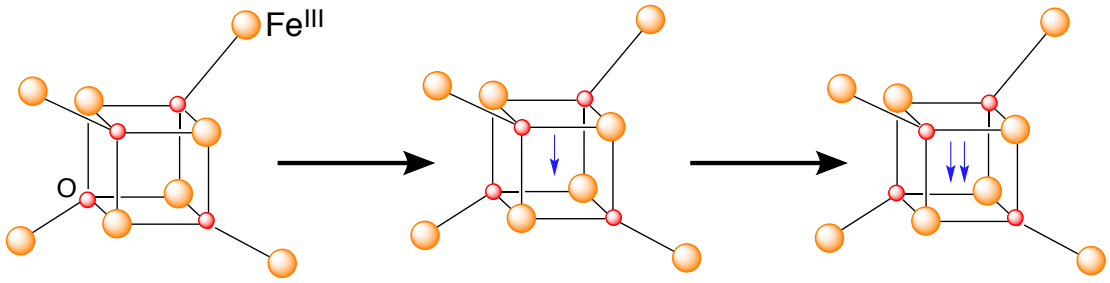
[57] A. K. Pandey, T. Gupta and B. P. Baranwal, *Transition Metal Chemistry* **2004**, *29*, 370-375.

[58] C. Fernandes, E. Stadler, V. Drago, C. J. daCunha and I. H. Kuwabara, *Spectrochimica Acta Part a-Molecular and Biomolecular Spectroscopy* **1996**, *52*, 1815-1821.

4

4 Electronic Structure of a Family of Octanuclear Iron-Oxo Clusters

This chapter contains a detailed discussion of the electronic structure of octuanuclear clusters $[Fe_8(\mu_4\text{-}O)_4(\mu_4\text{-pyrazolato})_{12}Cl_4]^z$ ($[Fe_8]^z$) with z = 0, 1–, 2–, which have a $Fe_8(\mu_4\text{-}O)_4$ cubane core. Mossbauer spectroscopy shows two distinct doublets that correspond to two Fe environments: 6-(cubane) and 5-(outer-cubane) coordination sites. The clusters $[Fe_8]^{0,1-}$ have previously been studied by our group, and here I will elaborate the discussion to include the two-electron mixed valence case $[Fe_8]^{2-}$. A series of spin states have been generated to investigate the effects of the different magnetic parameters on the two-electron localisation/delocalisation. Previous studies on $[Fe_8]^{1-}$ complex are consistent with a redox event where the electron prefers to localised on the cube, however, our DFT analysis show that $[Fe_8]^{2-}$ case is rather more complicated. The magnetic coupling between the cubane-outer Fe ions play crucial roles in determining the stability of the two-electron mixed valence states.



4.1 Introduction

This chapter is closely linked to the preceding one on mixed-valent Fe_3 triangles, in so much as it is also based on iron clusters linked by pyrazolato and oxide ligands. In this

case, however, the cluster architecture is rather more complex, based on a *T*-symmetric cubane-type structure, $[Fe_8(\mu_3\text{-}O)_4(\mu\text{-}pz)_{12}Cl_4]^z$ (pz = pyrazolate ring $C_3H_3N_2^-$), containing eight iron centers (Figure 4.1). Cubane-like structures have been of interest for several decades, primarily because of the role in biochemical redox processes[1-2] such as oxygen evolution,[3-5] and also, more recently, due to their potential in the field of single molecular magnets.[6-8] Like the Fe_3 triangles in Chapter 3, this compound was synthesised in the laboratories of our collaborator, Professor Raphael Raptis[9]. In the neutral complex, $[Fe_8]^0$, eight paramagnetic Fe^{III} ions are linked via oxide and pyrazolato-bridges. The cluster can be thought of as a cubane like-core Fe_4O_4, with the four peripheral Fe atoms connected to the cubane via a single oxo-bridge and capped by chloride ligands. Each of the cubane Fe ions occupies a distorted octahedral environment, while every outer Fe has trigonal bipyramidal coordination. The electrochemistry of this system is remarkably rich, and the molecule is stable in four distinct reduced states, each of which can be isolated and studied *in situ*. Previous work in our group has focused on the electronic structure of the neutral (all-ferric) and one-electron reduced species, $[Fe_8]^{1-}$. In the former, Heisenberg exchange is the dominant factor. while in the latter the key point of interest is the extent to which the “extra” electron is delocalised over the cluster due to double exchange. In this chapter, I will discuss the electronic structure of the doubly-reduced species, $[Fe_8]^{2-}$, where in addition to the Heisenberg and double exchange factors, repulsion between the two itinerant electrons also needs to be considered. This chapter begins with a review of the previous work on the $[Fe_8]^{0/1-}$ clusters, before turning to the new results on the doubly reduced species.

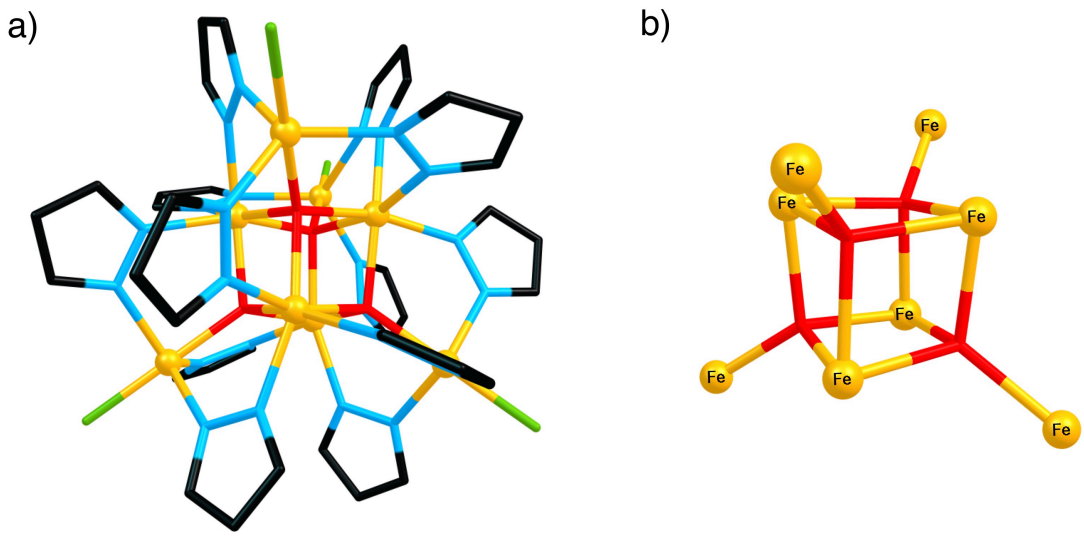


Figure 4.1: Structure of the $[Fe_8(\mu_3\text{-}O)_4(\mu\text{-}pz)_{12}Cl_4]^z$ cluster (**a**) and the Fe_8O_4 core (**b**).

4.1.1 All ferric oxidation state, $[Fe_8]^0$

The electronic structure of the neutral cluster, where all Fe centres are in the ferric (Fe^{III}) oxidation state, was reported in Reference [10]. The magnetic properties of this molecule are dominated by exchange coupling between the individual Fe centres through oxide bridges. The magnetic properties can be interpreted using an isotropic Heisenberg Hamiltonian, where only the spin quantum number *S* is required to describe the magnetic properties of the system.

$$\hat{H} = -J_{ij} \sum \hat{S}_i . \hat{S}_j \qquad 4.1$$

The exchange interaction is represented by the super-exchange coupling constant J_{ij} where $\hat{S}_i$ is the spin angular momentum operator. Noodleman's approach maps the diagonal elements of this Hamiltonian onto the Kohn-Sham eigenvalues in a basis of *Ising* configurations that contain the maximum and minimum projections of the spin angular momentum M_S. The use of only the maximum projections reduces the dimension of the problem from $(2S_i+1)^N = 1679626$ ($S_i = 5/2$ and N=8) to $2^8 = 256$

(either M_S = 5/2 or M_S = –5/2). The magnetic properties of the $[Fe_8]^0$ cluster can be described by two exchange coupling parameters:

$$H = H_{ex} = -J_1 \sum_{i=1}^{4} \sum_{j>i}^{4} S_i S_j - J_2 \sum_{i=5}^{8} \sum_{j=1, j\neq i-4}^{4} S_i S_j \qquad 4.2$$

where J_1 is the inner-inner coupling between the Fe ions within the cubane (Fe_c^{III}–Fe_c^{III}) while J_2 is the inner-outer coupling, Fe_c^{III}–Fe_o^{III}. The coupling between the outer Fe centres was not included in the Hamiltonian due to the large distance between the metal ions. [10]

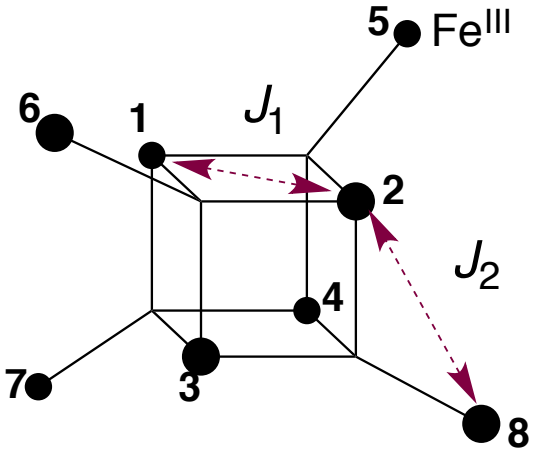


Figure 4.2: the two types of coupling constants

For the $[Fe_8]^0$ oxidation state, three possible configurations were identified (Figure 4.3), where filled and empty circles denote centres with M_S = +5/2 and -5/2, respectively. The energies of these three can be expressed in terms of J_1 and J_2 as shown in Equations 4.3–4.6.

$$E_{HS} = -\frac{150}{4}J_1 - \frac{300}{4}J_2 \qquad 4.3$$

$$E_{BS_1} = -\frac{300}{4}J_1 + \frac{300}{4}J_2 \qquad 4.4$$

$$E_{BS_2} = \frac{50}{4}J_1 + \frac{100}{4}J_2 \qquad 4.5$$

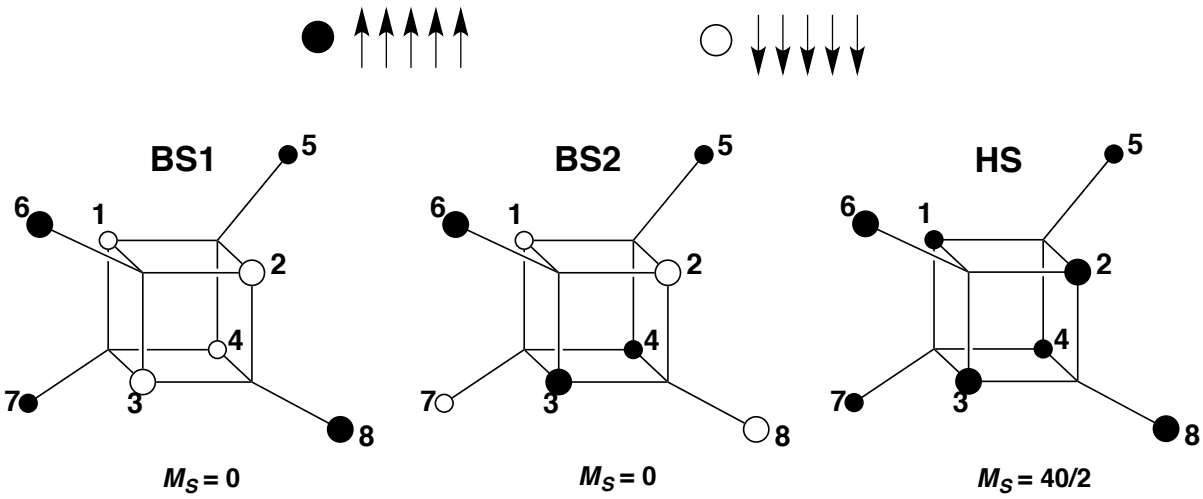


Figure 4.3: the spin states used to calculate the exchange coupling constants

The two *J* values then can be extracted by elimination: $J_1 = -6.3$ cm^{-1} and $J_2 = -52.8$ cm^{-1} which are very good match compared to experimental fitted values ($J_1 = -2.1$ cm^{-1} and -50.6 cm^{-1}). The values indicate that the dominant exchange coupling pathway is between the cubane and outer Fe centres, and that it is antiferromagnetic. The significantly different values of J_1 and J_2 are related to differences in the Fe–O–Fe angles, which are close to 90° for the former but nearer to 120° for the latter.

4.1.2 One-electron mixed valence, $[Fe_8]^{1-}$

An analysis of the 1-electron reduced cluster was presented in reference [11]. While the magnetism of the all-ferric $[Fe_8]^0$ species can be modelled using only exchange coupling parameters (J_1 and J_2) between the localised spin centres, the mixed valence $[Fe_8]^{1-}$ species requires a consideration of double exchange (or, equivalently, the transfer energy t). Since the extent of delocalisaton of itinerant electrons in mixed-valence (MV) species is a central issue in cluster chemistry,[12-13] Robin and Day[14] classified MV compounds into three categories, based on the behavior of the itinerant

electron: localised (Class I); weakly localised (Class II); and delocalised (Class III). Compounds in the final class, where itinerant electron(s) are free to move between metal centres, can be described using the concept of double exchange (B), an additional term in the spin Hamiltonian. The concept of double exchange was first introduced by Zener in 1951 as an attempt to understand the ferromagnetic and conductive properties of a mixed-valence perovskite at room temperature.[15] Later, the mechanism of double exchange was developed by Anderson and Hasegawa [16] and de Gennes[17], and it has since proved to be a vital concept in understanding both the ferromagnetism and high conductivity in class III mixed valence compounds. The textbook example commonly used to explain double exchange is a manganese dimer with two octahedral MV centres, Mn^{III}–O–M^{IV} (ca. Figure 4.4). Electron transfer from oxygen to M^{IV} is accompanied by simultaneous electron transfer from Mn^{III} to the oxygen, $Mn^{III}\rightarrow O\rightarrow M^{IV}$, and in order to maintain the optimal alignment of spins on the two metal centres (i.e. parallel as demanded by Hund's rules) the electrons on adjacent metal centres must also be aligned parallel (i.e. ferromagnetic). Double exchange therefore often works in opposition to exchange coupling, the former favouring ferromagnetic alignment of spins, the latter antiferromagnetic.

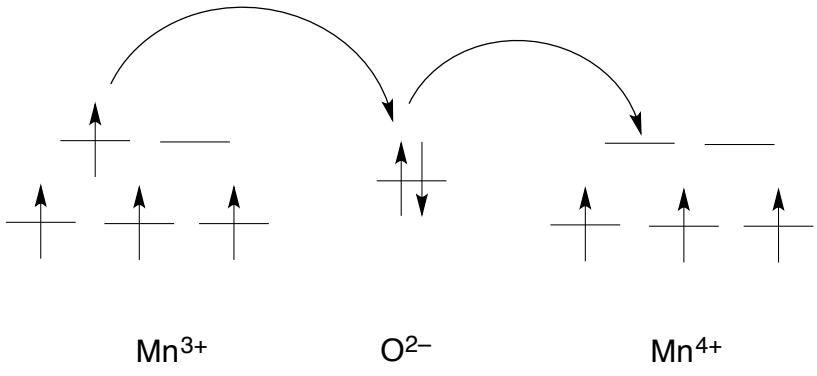


Figure 4.4: Example of double exchange mechanism: the electron from Mn^{3+} simultaneously replaced the oxygen electron that transfer to the low valence centre Mn^{4+}.

The double exchange phenomenon is well-studied in homodinuclear $d^n - d^{n+1}$, A–B dimers, but its extension to polymetallic systems is more challenging. The eigenvalues for such A–B systems have the following analytical formula

$$E_{\pm}(S) = -\frac{1}{2}JS(S+1) \pm \sqrt{\frac{(E_A - E_B)^2}{4} + B^2\left(S+\frac{1}{2}\right)^2} \qquad 4.6$$

where $\mathrm{B} = \mathrm{t}/(2\mathrm{S}^{\mathrm{o}} + 1)$ for $\mathrm{n} < 5$ and where $\mathrm{B} = \mathrm{t}/(2\mathrm{S}^{\mathrm{o}})$ for $\mathrm{n} \geq 5$. While t parameter refers to the transfer energy and the value of $\mathrm{S}^{\mathrm{o}} = \mathrm{S}_{\mathrm{A}} = \mathrm{S}_{\mathrm{B}}$corresponds to the core spin. One can see that the matrix elements of the transfer energy depend only on the total spin.

In reference [19], a Heisenberg Hamiltonian for $[Fe_8]^-$ was developed that contains the exchange coupling parameters discussed previously in the context of the neutral species, J_1 and J_2, and also a transfer term, *t*, which captures the effects of double exchange. The analysis of the exchange interaction is complicated because in principle the cubane-cubane (Fe_c–Fe_c) and cubane-outer (Fe_c–Fe_o) are dependent on oxidation state, and so we might anticipate two distinct parameters for the all-ferric pairs J_1 (Fe_c^{III}–Fe_c^{III}) and J_3 (Fe_c^{III}–Fe_o^{III}) and other two for mixed valence pairs coupling J_2 ($Fe_c^{III/II}$–$Fe_c^{II/III}$) and J_4 ($Fe_c^{III/II}$–$Fe_o^{II/III}$). There are also two possible pathways for delocalisation of the itinerant electron: inner-inner t_1 and inner-outer t_2: transfer between outer Fe centres was again neglected due to the distance between the centres. Finally, a third parameter, $\Delta = E_o - E_c > 0$ (the outer site is energetically less preferable) captures the intrinsic site asymmetry (which simply arises from the fact that the Fe ions in the cubane core, Fe_c, are coordinated differently from those located outside). The additional electron therefore experiences different local crystal fields in different coordinating environment.

The total Hamiltonian can therefore be expressed as follows:

$$\widehat{H} = \widehat{H}_{ex} + \widehat{H}_{tr} \qquad 4.7$$

Where the exchange part, $\widehat{H}_{ex}$, is given by:

$$\widehat{H}_{ex} = -J_{1(2)} \sum_{i=1}^{4} \sum_{j>i}^{4} \hat{S}_i \hat{S}_j - J_{3(4)} \sum_{i=5}^{8} \sum_{j=1, j\neq i-4}^{4} \hat{S}_i \hat{S}_j + \Delta \qquad 4.8$$

And the transfer part, $\widehat{H}_{tr}$, by:

$$H_{tr} = -t_1 \sum_{a=1}^{4} \sum_{b=1 b\neq a}^{4} H_{tr}(a \rightarrow b) - t_2 \sum_{a=5}^{8} \sum_{\substack{b=1, \\ b\neq a-4}}^{4} H_{tr}(a \rightarrow b) \qquad 4.9$$

The computational analysis using DFT involves generating the combinations of local spin states that ensure localisation/delocalization of the itinerant electron on particular site(s), and is very similar to that used in the analysis of spin states in the mixed valence Fe_3 triangles in the previous chapter. The key idea is that starting from a given all-ferric broken-symmetry state, an additional electron with spin-α is confined to centres where the majority-spin vector is β (because all spin-α orbitals on this site are already occupied) and *vice* versa. Figure 4.5 show the flow diagram for generating series of MV states for $[Fe_8]^{1-}$. The spin states that have been chosen to build up the spin Hamiltonian those are either localised (b2,3,7 and a7) and pair-delocalised (b4,5) broken symmetry states where the additional electron is confined either to a single centre or to a pair of adjacent centres. The label b1, for example, identifies the column b and row 1.

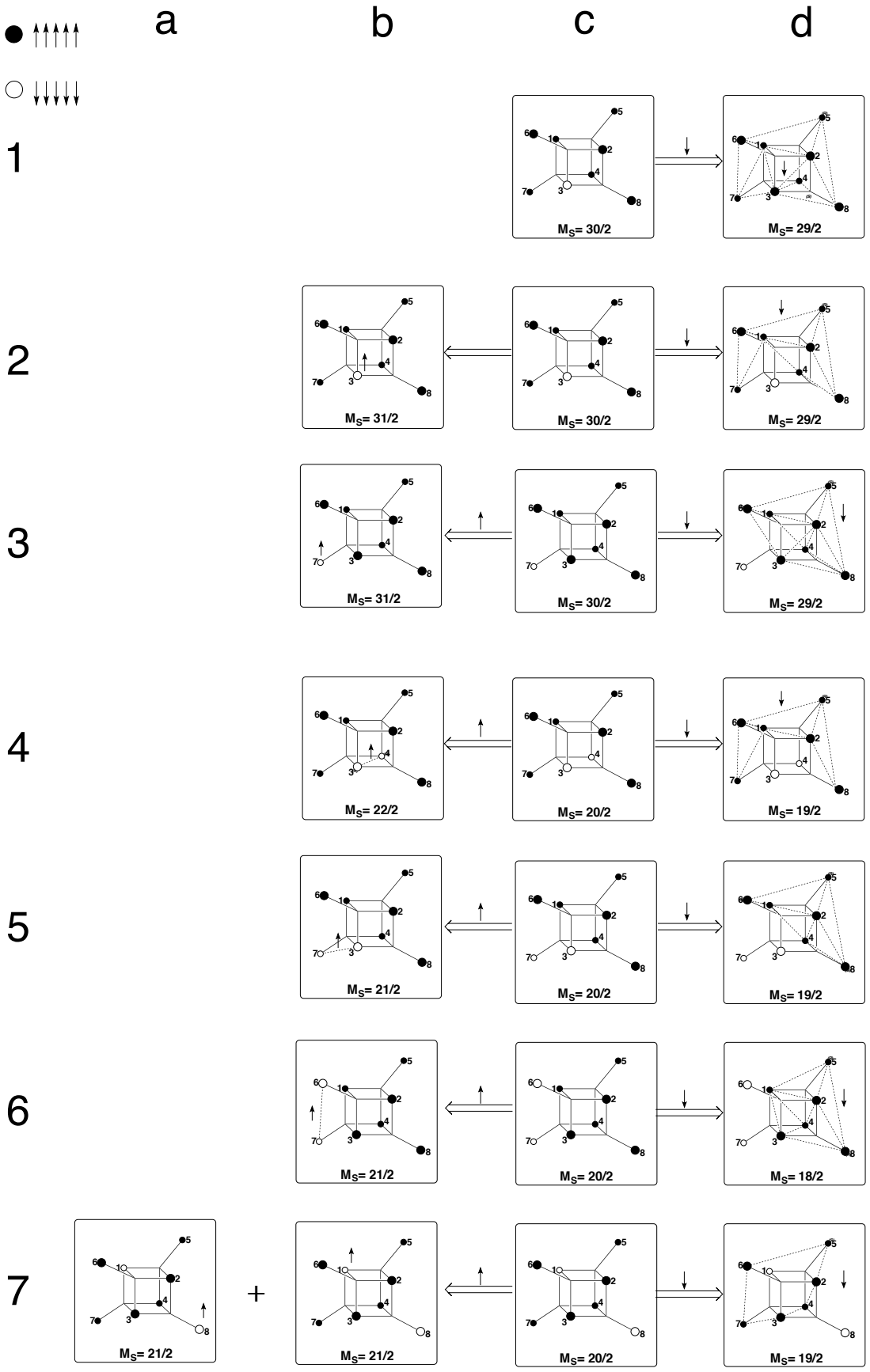


Figure 4.5: Flow diagram for some of possible spin states for $[Fe_8]^{1-}$: the black circles represent the α-majority spin Fe^{III} and the white circles β-majority Fe^{III} centres.

Noodleman's methodology[18] was again used to calculate the exchange coupling, transfer parameters and intrinsic site asymmetry by mapping the diagonal elements of the full spin Hamiltonian onto the Kohn-Sham eigenvalues. In the four localised BS states in Figure 4.5 (b2,3,7 and a7), delocalization is entirely blocked and so the energies of these configurations can be mapped onto the eigenvalues of the exchange-only Hamiltonian, (equation 4.8) giving us four equations:

$$E_{b2} = -\frac{75}{4}J_1 + \frac{60}{4}J_2 - \frac{225}{4}J_3 + \frac{60}{4}J_4 \qquad 4.10$$

$$E_{b3} = -\frac{150}{4}J_1 + \frac{225}{4}J_3 + \frac{60}{4}J_4 + \Delta \qquad 4.11$$

$$E_{b7} = -\frac{75}{4}J_1 + \frac{60}{4}J_2 - \frac{75}{4}J_3 + \frac{60}{4}J_4 \qquad 4.12$$

$$E_{a7} = -\frac{75}{4}J_3 + \frac{60}{4}J_4 + \Delta \qquad 4.13$$

The linear algebraic solution of these equations gives the value of the four parameters $J_1, J_2, J_3,$ and Δ. We note here that there are five unknowns, but J_4 has the same coefficient in the all four equations $(+60/4)$ and so is eliminated in the pairwise subtraction.

The two broken-symmetry states, d4 and d5, can be treated as 'effective dimers' because the itinerant electron is confined to two adjacent metal centres. In the case of d4, the electron is distributed over two cubane centres Fe_c–Fe_c while in d5 the electron is trapped on an Fe_c–Fe_o dimer. For the Fe_c–Fe_c case, the $[2\times2]$ spin Hamiltonian matrix in the basis of pair states, $a^{\uparrow}b$, where the arrow (↑) represents the fact that the itinerant electron can be localised/delocalised on centres a and b, can therefore be expressed as:

$$E_{localization} = \begin{pmatrix} \langle a^{\uparrow} b|\widehat{H}|a^{\uparrow} b\rangle & \langle a^{\uparrow} b|\widehat{H}|ab^{\uparrow}\rangle \\ \langle ab^{\uparrow}|\widehat{H}|a^{\uparrow} b\rangle & \langle ab^{\uparrow}|\widehat{H}|ab^{\uparrow}\rangle \end{pmatrix} \qquad 4.\ 14$$

The diagonal elements correspond to the localised states while the off-diagonal elements correspond to the transfer integrals in the cube t_1.

$$d4: \begin{pmatrix} \frac{25}{4}J_1 + \frac{20}{4}J_2 - \frac{75}{4}J_3 + \frac{60}{4}J_4 & t_1 \\ t_1 & \frac{25}{4}J_1 + \frac{20}{4}J_2 - \frac{75}{4}J_3 + \frac{60}{4}J_4 \end{pmatrix} \qquad 4.\ 15$$

$$E_{BS5_{\pm}} = \frac{25}{4}J_1 + \frac{20}{4}J_2 - \frac{75}{4}J_3 + \frac{60}{4}J_4 \pm t_1 \qquad 4.\ 16$$

For symmetrical clusters, where the exchange part is constant, this simplifies to $t_1 = \frac{E_{BS5_+} - E_{BS-}}{2}$. In the DFT calculations, the difference $E_+ - E_-$ can be approximated as the gap between the Kohn-Sham orbitals formed by symmetric and anti-symmetric combinations of the relevant spin orbitals.

The corresponding analysis for t_2 is complicated because the diagonal elements of the corresponding [2×2] Hamiltonian matrix are not identical, and so the analytical formula has a more complex structure.

$$d5: \begin{pmatrix} -\frac{75}{4}J_1 + \frac{60}{4}J_2 - \frac{125}{4}J_3 + \frac{20}{4}J_4 & t_2 \\ t_2 & -\frac{125}{4}J_3 + \frac{20}{4}J_4 + \Delta \end{pmatrix} \qquad 4.\ 17$$

Nevertheless, mapping the difference in Kohn-Sham eigenvalues onto this formula gives a good approximation for t_2.

As a result of this analysis, the following values for the various parameters were derived:

$$J_1(\mathrm{Fe_c^{III}} - \mathrm{Fe_c^{III}}) = -5.9\ cm^{-1}$$

$$J_2(\mathrm{Fe_c^{III/II}} - \mathrm{Fe_c^{II/III}}) = -10.1\ cm^{-1}$$

$$J_3\ (\mathrm{Fe_c^{III}} - \mathrm{Fe_o^{III}}) = -55.1\ cm^{-1}$$

$$t_1\ (\mathrm{Fe_c^{II/III}} \leftrightarrow \mathrm{Fe_c^{III/II}}) = -1438\ cm^{-1}$$

$$t_2(\mathrm{Fe_c^{II/III}} \leftrightarrow \mathrm{Fe_o^{III/II}}) = 1784\ cm^{-1}$$

$$\Delta = 0.7\ cm^{-1}$$

It is clear that values of the coupling constants J_1 and J_2/J_3, are very similar to those reported formerly in all-ferric species (J_1 and J_2, respectively). Clemente-Juan *et al.* have argued that strength of exchange coupling should be largely independent of oxidation state, and that seems to be the case here.[19] We noted that J_4 is inaccessible from the selection of broken-symmetry BS1-4, but we assume that $J_2 = J_4$.

Experimental magnetic measurements offer two perspectives on the t_2 parameters. The best fit to temperature dependent magnetic measurements up to 300 K (Figure 4.6a) gives $t_2 = 1750$ cm^{-1}, in excellent agreement with the computed value of 1784 cm^{-1}. In contrast, the best fit to magnetic data at very low temperature and extremely high pulse magnetic field (Figure 4.6b) are obtained when cubane-outer electron transfer is ignored entirely ($t_2 = 0$). This suggests that significant vibronic coupling, not included in our model, drives localization of the electron and hence quenching of t_2, at low temperature.

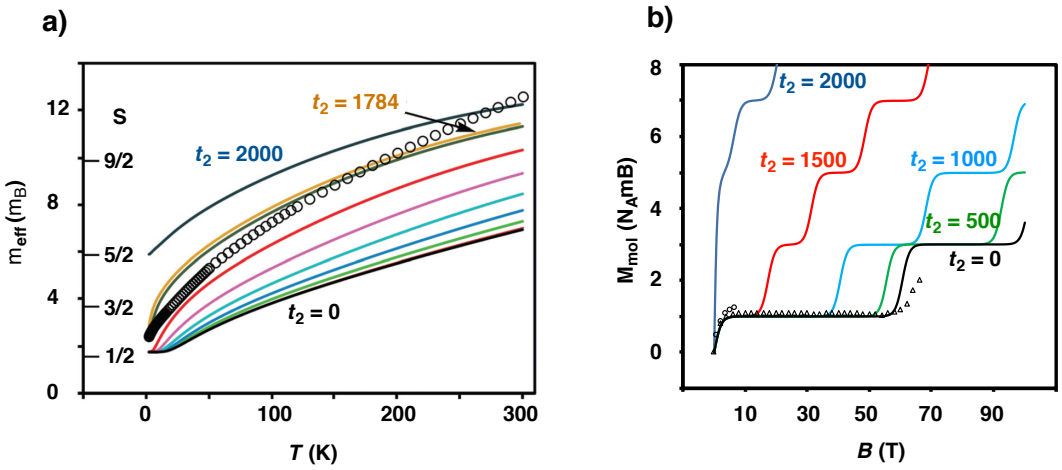


Figure 4.6: the magnetic measurements for [Fe8]$^{1-}$: (**a**) The temperature dependent. (**b**) The field dependent magnetism.

4.1.3 Results: Electronic structure of the two-electron mixed valence, $[Fe_8]^{2-}$

The purpose of this chapter is to extend our analysis of mixed-valence Fe_8 clusters to the 2-electron reduced state. The construction of a spin Hamiltonian for such a system, with two itinerant electrons, is extremely challenging simply because it contains many independent parameters. In addition to the exchange and transfer terms described above, we need also to consider Hubbard-like terms describing electrostatic repulsions between itinerant electrons. At this point, identifying a suitable Hamiltonian to map onto the DFT-computed energies has not proven possible, so we restrict the discussion here to a qualitative one, where we investigate factors that influence the relative stabilities of the various broken-symmetry states.

The key concept applied here is again the idea that by starting from a given all-ferric configuration, the position and degree of delocalization of any additional electrons can be controlled by manipulation of spins. In Figure 4.7, column b, we show a range of available high-spin and broken-symmetry states for the all-ferric cluster. The black circles represent Fe^{III} ion (d^5) with all five electrons have majority spin α (M_S = 5/2), while the white circles represent the same centres with all five electrons have β spin (M_S = –5/2). The all-ferric states are arranged in order of decreasing stability, with the most antiferromagnetic (M_S = 0) at the top. Columns a, c, and d represent the three possible alignments of spin for the two additional electrons starting from the all-ferric reference.

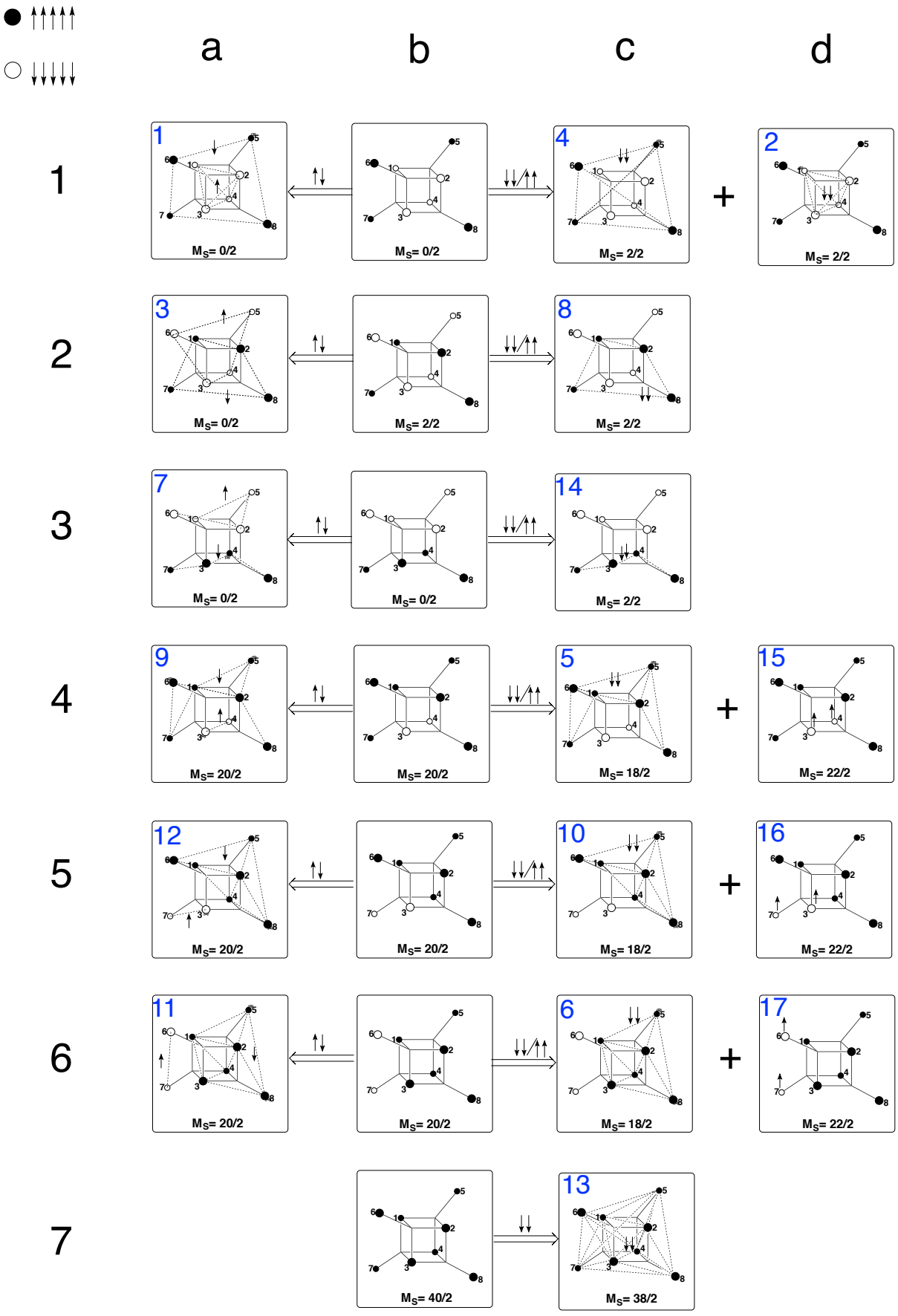


Figure 4.7: spin state tree diagram, the black circles represent spin 5-spin “up” electrons, while the white circles represent five” down” spin. The numbers in blue represent ascending energy order.

The extra electrons can be: (i) both spin-α (column c), (ii) both spin-β (column d) or (iii) one spin-α and one spin-β (column a). The relative energies and spin densities of all these states are collected in Table 4.1, where the designation a1, for example, identifies the column and row in Figure 4.7. The ranking of each broken-symmetry state in terms of relative stability is shown by the blue number in the corner of each square.

Comparison of the spin states in Figure 4.7 and Table 4.1, clearly reveals that there are many factors which determine the relative stabilities of the spin states. The strong antiferromagnetic coupling that dominates both the neutral and one-electron reduced clusters is clearly still important here; the two most stable states, a1 and d1, are derived from the most stable all-ferric case, b1, and therefore have the maximum number of antiferromagnetic coupling pathways ($-12J_2$).Looking further down the list of broken-symmetry states, it is clear that there is a broad correlation between the stability of the doubly reduced configurations and the stability of the all-ferric parent. The exceptions to this general rule offer some insight into the more subtle factors. For example, c1 is less stable than a2, despite the latter having a less optimal alignment of spin vectors (the exchange part of the Hamiltonian gives $-4J_2$ rather than $-12J_2$). In c1, however, the two itinerant electrons are confined to the outer Fe centres, and so we anticipate that double exchange will make only a very minor contribution (outer-outer double exchange was entirely neglected in analysis of the one-electron reduced species[11]). An additional factor to consider in this analysis is the potential impact of repulsion between the two itinerant electrons. This will be minimised in cases where the two electrons are orthogonal to each other in the sense that they are delocalised over mutually exclusive subsets of atoms.

Table 4.1: Relative energies and Mulliken spin densities for spin states listed in Figure 4.7

	S	E(eV)	Fe1	Fe2	Fe3	Fe4	Fe5	Fe6	Fe7	Fe8
a1	0	0.00	-3.944	-3.944	-3.947	-3.947	3.928	3.928	3.946	3.946
d1	(2/2)	0.12	-3.781	-3.781	-3.781	-3.781	3.996	3.996	3.996	3.996
a2	0	0.25	3.941	3.941	-3.941	-3.941	-3.958	-3.958	3.958	3.958
c1	(2/2)	0.48	4.035	4.035	4.038	4.037	-3.832	-3.825	-3.798	-3.799
c4	(18/2)	0.53	3.973	3.973	-3.990	-3.990	3.966	3.966	3.934	3.934
c6	(18/2)	0.54	3.967	3.910	3.967	3.910	-3.991	4.019	4.019	-3.991
a3	0	0.56	3.981	3.981	-3.981	-3.981	3.987	3.987	-3.987	-3.987
c2	(2/2)	0.57	4.026	4.026	-3.794	-3.794	-3.817	-3.817	4.017	4.017
a4	(20/2)	0.70	4.039	4.039	-3.768	-3.768	4.014	4.014	4.024	4.024
c5	(18/2)	0.70	4.008	3.939	-3.991	3.943	4.012	3.955	3.942	-4.015
a6	(20/2)	0.80	4.035	4.044	4.035	4.044	-3.815	4.054	4.054	-3.815
a5	(20/2)	0.86	4.052	4.032	-3.796	4.042	4.042	4.031	4.032	-3.807
c7	(38/2)	1.16	4.051	4.051	4.051	4.051	4.044	4.044	4.044	4.044
c3	(2/2)	1.17	4.037	4.037	-3.825	-3.826	4.033	4.034	-3.805	-3.805
d4	(22/2)	1.71	4.084	4.086	-3.395	-3.138	4.031	4.047	4.030	4.026
d5	(22/2)	1.78	4.079	4.043	-3.145	4.054	4.051	4.037	4.049	-3.300
d6	(22/2)	1.78	4.067	4.055	4.067	4.055	-3.263	4.066	4.066	-3.264

This is necessarily the case for the states in column a where the itinerant electrons have opposite spins, and it is striking that a1-3 are considerably more stable than b1-3 and d1-3. At the opposite extreme, repulsion is maximised in states where the two electrons are confined to two atoms, as in d4, d5 and d6, which are the least stable of all the configurations shown here. We note that cases where both electrons are confined to a single atom (not shown in Figure 4.7) are dramatically less stable.

4.2 Conclusions

In this chapter, we have analyzed the electronic structure of the $[Fe_8]^{2-}$ cluster, and placed it in the context of previous work on the $[Fe_8]^{0}$ and $[Fe_8]^{1-}$ analogues. The inner-outer antiferromagnetic coupling seems to remain the dominant factor controlling the electronic stability in all three clusters. Nevertheless, additional factors including double exchange and repulsions between itinerant electrons play a role in determining the relative stabilities of the $[Fe_8]^{2-}$ spin states. In the future, we hope to convert these qualitative observations regarding stability into a quantitative mapping onto an appropriate spin Hamiltonian.

4.3 Computational Details

For these calculations on $[Fe_8]^{2-}$, the pure OPBE functional was used with polarised double-zeta (DZP) quality basis sets for the main group atoms and polarised triple zeta (TZP) for Fe. The frozen core approximation was employed to reduce the computational cost of the calculations. All these calculations were carried out using the ADF2013.02 code. The broken symmetry states were generated by single point calculations on the optimised HF (M_S = 38/2). Since the Fe_8 cluster is characterised by a robust geometry and stays unchanged upon the reduction, we have found geometry optimizations has minor effect on the stability order of the spin states, therefore we have run single point calculations to generate BS states that fail to pass the geometry optimization test.

Generating the spin states required to work out all the introduced parameters is not a straightforward procedure, since it requires monitoring the symmetry of the molecules and the symmetry of the electronic distribution. In broken symmetry states, the electron distribution has lower symmetry than the nuclei (the electronic symmetry

of the H_2 molecule is $D_{\infty h}$; however, the electronic symmetry for the broken symmetry state is C_{2v}). Upon reaching a particular nuclear symmetry, the software would frequently distribute the electron density accordingly, producing a non-desired spin state. To overcome this complication, one must ensure that the computational software is commanded to ignore the nuclear symmetry. Furthermore, the large number of possible spin states requires careful selection of the minimal basis of states that be used to solve the simultaneous equations that reveal all the required magnetic parameters.

4.4 References

[1] K. Tagawa and D. I. Arnon, *Nature* **1962**, *195*, 537-543.

[2] S. Niu and T. Ichiye, *Journal of the American Chemical Society* **2009**, *131*, 5724-5725.

[3] A. Pichon, *Nat Chem* **2015**, *7*, 465-465.

[4] C. Philouze, G. Blondin, S. Menage, N. Auger, J. J. Girerd, D. Vigner, M. Lance and M. Nierlich, *Angewandte Chemie-International Edition in English* **1992**, *31*, 1629-1631.

[5] S. Paul, F. Neese and D. A. Pantazis, *Green Chemistry* **2017**, *19*, 2309-2325.

[6] C. Bosch-Navarro, E. Coronado, C. Marti-Gastaldo, B. Rodriguez-Gonzalez and L. M. Liz-Marzan, *Advanced Functional Materials* **2012**, *22*, 979-988.

[7] S. Cardona-Serra, J. M. Clemente-Juan, E. Coronado, C. Marti-Gastaldo and E. Navarro-Moratalla, *European Journal of Inorganic Chemistry* **2013**, 1903-1909.

[8] H.-L. Tsai, C.-I. Yang, W. Wernsdorfer, S.-H. Huang, S.-Y. Jhan, M.-H. Liu and G.-H. Lee, *Inorganic Chemistry* **2012**, *51*, 13171-13180.

[9] R. G. Raptis, I. P. Georgakaki and D. C. R. Hockless, *Angewandte Chemie-International Edition* **1999**, *38*, 1632-1634.

[10] P. Baran, R. Boča, I. Chakraborty, J. Giapintzakis, R. Herchel, Q. Huang, J. E. McGrady, R. G. Raptis, Y. Sanakis and A. Simopoulos, *Inorganic Chemistry* **2008**, *47*, 645-655.

[11] E. M. Zueva, R. Herchel, S. A. Borshch, E. V. Govor, W. M. C. Sameera, R. McDonald, J. Singleton, J. Krzystek, Z. Travnicek, Y. Sanakis, J. E. McGrady and R. G. Raptis, *Dalton Transactions* **2014**, *43*, 11269-11276.

[12] J. Kübler, *Theory of Itinerant Electron Magnetism*, Oxford University Press, **2000**, p. 494.

[13] B. Bechlars, D. M. D'Alessandro, D. M. Jenkins, A. T. Iavarone, S. D. Glover, C. P. Kubiak and J. R. Long, *Nature Chemistry* **2010**, *2*, 362-368.

[14] M. B. Robin and P. Day, *Advances in Inorganic Chemistry and Radiochemistry* **1968**, *10*, 247-422.

[15] C. Zener, *Physical Review* **1951**, *82*, 403-405.

[16] P. W. Anderson and H. Hasegawa, *Physical Review* **1955**, *100*, 675-681.

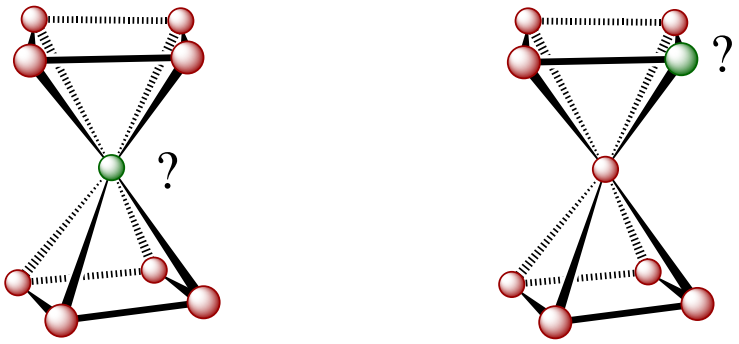
[17] P. G. de Gennes, *Physical Review* **1960**, *118*, 141-154.

[18] L. Noodleman, *The Journal of Chemical Physics* **1981**, *74*, 5737-5743.

[19] J. M. Clemente-Juan, J. J. Borrás-Almenar, E. Coronado, A. V. Palii and B. S. Tsukerblat, *Inorganic Chemistry* **2009**, *48*, 4557-4568.

5 Analysis of Site Preferences in Heterometallic Enneanuclear [$Fe_{9-x}Ni_x$] Clusters

In this chapter, we discuss site preferences in a family of heterometallic enneanuclear clusters of general form [$Fe_{9-x}Ni_x$]. The synthesis and measurements of these clusters was done by our collaborators in Athens led by Dr Yiannis Sanakis. The clusters in question have two distinct coordination sites – one 8-coordinate site (the central position of the cluster) and eight 6-coordinate (octahedral) sites at the periphery.



X-ray crystallography is unable to distinguish the Ni^{II} and Fe^{II} ions in these clusters, leaving their distribution over the different sites undetermined. ^{57}Fe Mössbauer spectroscopy suggests that the Fe centres might preferentially occupy the central site, although the interpretation of this data is unclear. We attempt to resolve this question by performing density functional calculations on a series of clusters M@M'$_8$, where M and M' can be any one of the metals, Ni, Fe, Zn, Mn. The computed relative energies of the different metal clusters are consistent with the preliminary conclusions from the

Mössbauer study, in so much as clusters are more stable when the Fe occupies the 8-coordinate site, but a detailed analysis suggests that the driving force is the large ligand field stabilisation energy (LFSE) of the Ni^{II} ions for the 6-coordinate sites: the Fe^{II} ions, in contrast, do not have a strong preference and simply fill the vacancies left after all Ni^{II} ions have been complexed. This work has been published recently in Dalton Transactions.[1]

5.1 Introduction

5.1.1 Site Preferences of Transition Metal Ions

The issue of site preference of transition metal ions is a classic problem in solid-state inorganic chemistry,[2-6] perhaps the most commonly cited example being the structure of the normal and inverse spinels. The spinels have the general formula AB_2X_4, where A and B can be element of d- or f-block metal ions and X is commonly an oxide ion, although it can also be any of the chalcogenide or halide ions. In the prototypical spinel structure, A is normally a divalent cation while B is trivalent, and in a *normal* spinel, the A cation occupies the tetrahedral sites and the B cations occupy the octahedral ones, $(A^{2+})^{Tet}(B^{3+})_2{}^{Oct}O_4$. In the *inverse spinel* structure, in contrast, the B cations occupy tetrahedral sites and half of the octahedral sites, the other half being occupied by the A cation. $(B^{3+})^{Tet}(A^{2+}B^{3+})_2{}^{Oct}O_4$. Site preferences are typically interpreted using ligand field stabilisation energy (LFSE) arguments, wherein the cation with the greater potential LFSE will occupy the octahedral site where the ligand field is intrinsically stronger. The two common textbook examples are the inverse spinel $Fe^{II}Fe_2{}^{III}O_4$ and its normal counterpart $Mn^{II}Mn_2{}^{III}O_4$. In latter, the LFSE for the octahedral site is 0 and $-0.6\Delta_o$ for Mn^{II} and Mn^{III} respectively, which means that the normal spinel is highly

preferable, (*i.e* Mn^{III} will be more stable than Mn^{II} in the octahedral site) For the $Fe^{II}Fe_2^{III}O_4$ compound, in contrast, the LFSE is $-0.4\Delta_o$ for Fe^{II} but 0 for the Fe^{III} ion. This means exchanging Fe^{II} for Fe^{III} in the octahedral site will result in a net gain in stabilisation energy, and hence magnetite, Fe_3O_4, prefers the inverse spinel structure. In the context of this study, the inverse spinel structure of trevorite, $NiFe_2O_4$, is particularly relevant. The very strong LFSE of Ni^{II} in the octahedral coordination provides a strong driving force that controls the Ni^{II} and Fe^{II} distribution over the 8- and 6-coordinate sites. Similar factors drive the structural chemistry of more complex phases such as the Brownmillerite phase $Ca_2Cr_xFe_{2-x}O_5$. The Cr^{III} (d^3) LFSE is much greater than that of Fe^{III} (d^5), forcing all the chromium ions to occupy the octahedral sites. The iron ions then fill the tetrahedral sites and remainder of octahedral ones.

The issue of site preference is much less studied in molecules than in solids, simply because a ligand coordination sphere is typically more flexible than an oxide lattice, allowing ions to deform the coordination environment to attain an optimal coordination geometry. Nevertheless, the distribution of ions over competing sites plays an important role in biochemistry, where heteronuclear clusters are vital building blocks in many enzyme active sites. For example, the $CaMn_4$ motif is responsible for the water oxidation in oxygenic photosynthesis and the distribution of Ca and Mn ions appears to play a key role in reactivity.[7] Similarly, Fe/(Mo, V, Fe)-based machineries are used for nitrogen fixation[8] while purple acid phosphatases and metallothioneins for heavy metal binding.[9] Of most direct relevance to this work are the Fe/Ni hetero-metallic clusters in [NiFe] hydrogenases[10] and the Ni-[Fe-4S] carbon monoxide dehydrogenases.[11-16] Heterometallic clusters are also becoming increasingly important in single molecular magnets,[17-25] and so the task of establishing well-

defined coordination geometries for the metal ions and a model to clarify structure-function relationships is an important goal.

5.1.2 Homogenous and Heterogeneous Enneanuclear Clusters: a Summary of the Experimental Data.

In recent years, our collaborators in Athens have synthesised a series of homometallic enneanuclear clusters with the general formula $M_9^{II}(\mu_4\text{-}OH)_2(O_2CMe)_8(py_2CO_2)_4$ where $[py_2CO_2]^{2-}$ is the dianion of the gem-diol form of di-2-pyridyl ketone. M^{II} is one of Fe^{II}, Co^{II} or Ni^{II}.[25-31] (Figure 5.1)

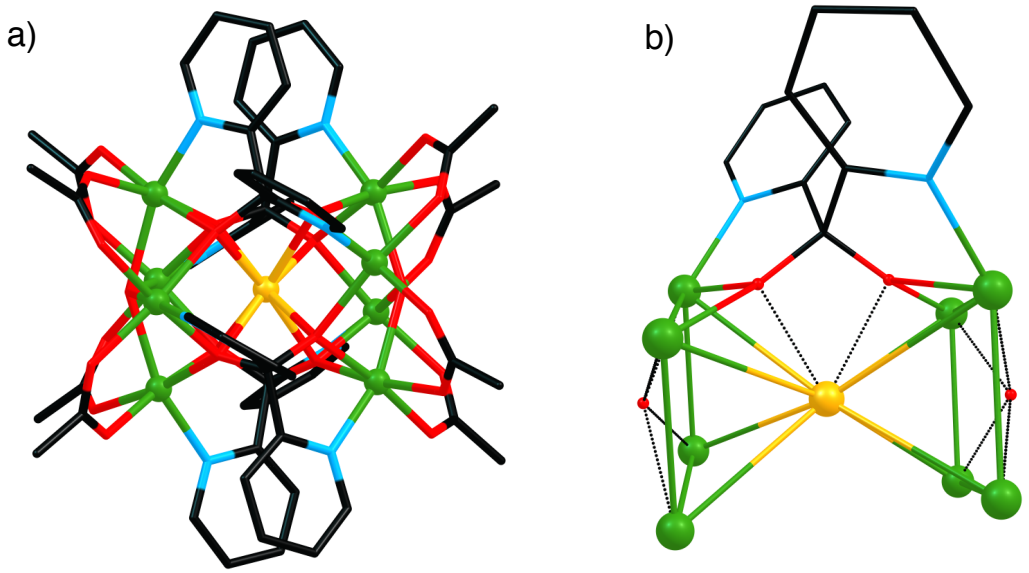


Figure 5.1: (a) Schematic representation of the ennea-nuclear molecular cluster (the hydrogens are removed for clarity), the atomic colours are: green; 6-coordinate metal site, yellow; 8-coordinated metal ion, red; oxygen, blue; nitrogen, grey; carbon. (b) Square antiprism pyramidal metallic core. The coordination mode of $py_2CO_2^{2-}$ ligand, 12 of them with 8 acetate ligands surrounding the square antiprism pyramidal core to make the structure of a. The dashed bonds imply week ligand-metal interactions.

The nine metals are distributed between two distinct sites: eight occupy 6-coordinate (octahedral) sites at the bases of two square pyramidal M_4 units while the ninth occupies an 8-coordinate apex site, linking the two square antiprisms. The cluster framework is highly adaptable, and $\mu_4\text{-}OH^-$ ligands can be replaced by $\mu_4\text{-}N_3^-$ or by μ_4-

NCO^-either via self-assembly or by ligand exchange. Moreover, in the [Ni^{II}_9] case, the acetate ligands can be substituted by pivalates. The switch from μ_4-OH^- ligands to μ_4-N_3^- or by μ_4-NCO^- causes the magnetic coupling to switch from antiferromagnetic to ferromagnetic, at least in the [Fe^{II}_9], [Co^{II}_9] and [Ni^{II}_9] clusters.[28-30]

More recently, our collaborators have succeeded in synthesising four distinct isostructural heterometallic clusters [$Fe_{9-x}{}^{II}Ni^{II}_x(\mu_4\text{-}OH)_2(O_2CMe)_8(py_2CO_2)_4$] (**2**-**5**) with different Ni/Fe ratios, as determined by comparing the intensities from X-ray fluorescence spectroscopy. Alongside the Fe_9 and Ni_9 homo-nuclear cases, **1** and **6**, respectively, these clusters form a continues series with varying Ni/Fe composition. The average values of x in heterometallic clusters **2** - **5** found in this way are:

1 [$Fe_9{}^{II}(\mu_4\text{-}OH)_2(O_2CMe)_8(py_2CO_2)_4$]

2 [$Fe_{8.0}{}^{II}Ni^{II}_{1.0}(\mu_4\text{-}OH)_2(O_2CMe)_8(py_2CO_2)_4$]

3 [$Fe_{2.98}{}^{II}Ni^{II}_{6.02}(\mu_4\text{-}OH)_2(O_2CMe)_8(py_2CO_2)_4$]

4 [$Fe_{1.54}{}^{II}Ni^{II}_{7.46}(\mu_4\text{-}OH)_2(O_2CMe)_8(py_2CO_2)_4$]

5 [$Fe_{1.19}{}^{II}Ni^{II}_{7.81}(\mu_4\text{-}OH)_2(O_2CMe)_8(py_2CO_2)_4$]

6 [$Ni^{II}_9(\mu_4\text{-}OH)_2(O_2CMe)_8(py_2CO_2)_4$]

The structures of these compounds can all be refined using the same space group (P4/nnc), with very similar unit cell dimensions, and the geometries are very similar to those of the homometallic analogues. However, the distribution of the two metal ions over the two competing positions (eight octahedral off-centre and one in the centre of $[M^{II}_9(py_2CO_2)_4]^{10+}$ core) cannot be determined by X-ray measurements because the scattering factors of Fe and Ni are too similar. The X-ray fluorescence spectroscopy

is insensitive to the coordination number or geometry, and so we are left with Mössbauer spectroscopy as the only handle able to distinguish between two sites.

Figure 5.2 shows the ^{57}Fe Mössbauer spectra of four enneanuclear clusters, labelled **1**-**5**. The positions of the absorption lines are consistent with high-spin Fe^{II}, and each of the five spectra show two doublets, almost superimposed on each other, which are assigned to 6 and 8-coordinate sites. The difference between the two is most apparent on the left-hand side of the superimposed doublets. One doublet (the blue line) with Mössbauer shift (δ) and quadrupole splitting (ΔE_Q), of 1.23 mm/s and 2.57 mm/s respectively, has been assigned to the 6-coordinate Fe ($Fe^{(6)}$) site while the lower intensity doublet at δ = 1.35 mm/s and ΔE_Q= 3.14 mm/s has been assigned to the 8-coordinate Fe ($Fe^{(8)}$) doublet.[29-30] It is immediately apparent from the changes in spectra across the series **1-5** that as the proportion of Fe in the cluster decreases (1>2>3>4>5), the relative intensity of the peak assigned to the 8-coordinate site increases relative to that assigned to the 6-coordinate alternative. Thus, on a purely qualitative level, it appears that at low Fe concentration, binding at the 8-coordinate site is preferred. Of course, our attention here is drawn to the Fe ions because we have a direct experimental handle on their distribution, but the same data set could be summarised equally well by the statement that Ni accumulates preferentially in the 6-coordinate sites, with the Fe ions simply filling the remaining available sites. A key objective in this chapter will be to establish which of the two ions is primarily responsible for the observed distribution. Before tackling this problem, however, we note that the analysis of site preferences rests entirely on the validity of the Mössbauer assignments. These are based primarily on the spectrum of homonuclear **1** where the 8-coordinate site is observed only as a small shoulder at ~3 mm/s; the other

component of the doublet is buried under the much more intense peak from the 6-coordinate Fe centres. Thus, the first goal of our computational work is to validate the assignment of the Mössbauer spectrum, and establish the origin of the different parameters for the two types of site.

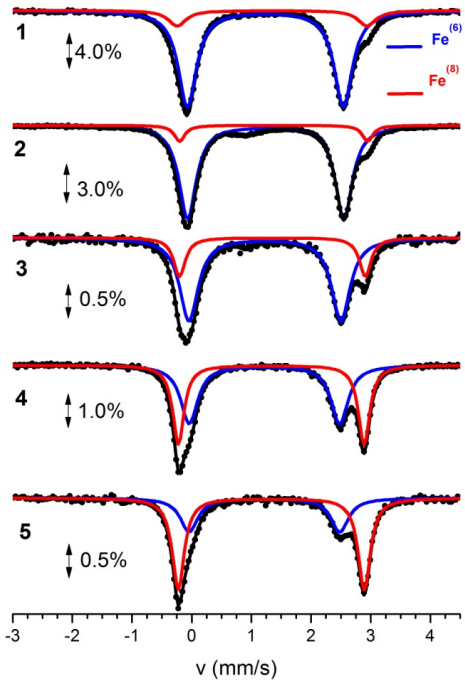


Figure 5.2: Mössbauer spectra of 1-5 compounds, the black colour refers to the experimental data while the red and blue coloured peaks corresponds to the theoretical fitted data, the red and blue signify 6- and 8-coordinated Fe respectively. These spectra measured by Sanakis et al at Demokritos.

5.2 Computational Details

All the molecular geometries in this chapters are optimised using the pure density functional OPBE,[32] as implemented in ADF 2013 package,[33] and a polarised triple-zeta (TZP) Slater-type basis set. In all cases a ferromagnetic alignment of spins was imposed (the sum of $S = 1$ for each Ni, $S = 2$ for Fe and $S = 0$ for Zn). In principle, the issue of site preference could be addressed simply by comparing the energies of two isomers of, for example, $FeNi_8(\mu_4\text{-}OH)_2(O_2CMe)_8(py_2CO_2)_4$, one with the Fe ion in the central 8-coordinate site and the other with it in a basal 6-coordinate site. In practice,

however, this always leads to intractable problems with self-consistent field convergence, probably as a result of the inevitable near degeneracies of occupied and virtual orbitals in low-symmetry coordination sites. We have therefore adopted an alternative strategy based entirely on high-symmetry (D_4) M@M'$_8$ clusters. We introduce here the shorthand notation M@M'$_8$ where M represents the metal in the 8-coordinate site and M' the metals in the 6-coordinate sites. Whilst SCF convergence in these cases is not trivial, it is tractable and leads to chemically reasonable Mulliken spin densities on both Fe^{II} and Ni^{II} ((1.52 ± 0.03) (Ni^{II} S = 1), 3.73 ± 0.03 (Fe^{II}, S = 2)).

The Mössbauer parameters were calculated using precisely the same methodology described in Chapter 3, where we employed the experimental calibration developed by Noodleman and co-workers based on the electron density at the nucleus. [34] To ensure comparability of the gradient α in the correlation used to calculate the isomer shift, we follow Noodleman's protocol: *i.e.* , the a density functional VWN-PW91,[35-36] a polarised triple-zeta all-electron basis and the COSMO solvation model (ε = 32.7).[37] The isomer shift, δ, is calculated from the computed electron density at the nucleus, $\rho(0)$, using $\delta = \alpha\rho(0) + C$ where fitting parameters α and C are the gradient and the intercept, respectively, of the plot of density *vs* experimental isomer shift for a range of compounds (see the computational details of Chapter 3).

5.3 Results and Discussion

5.3.1 Mössbauer Spectroscopy

The computed Mössbauer parameters for the D_4-symmetric clusters Fe@Ni_8 and Ni@Fe_8 are summarised in Table 5.1 below, along with the homonuclear case Fe@Fe_8 (cluster **1**). The experimental data, where available, is shown in parenthesis.

Table 5.1: The computed Mössbauer parameters: isomer shift δ, the electric field gradient components,(V_{XX}, V_{ZZ}, V_{ZZ}), and quadrupole splitting (ΔE) for M@M'8 clusters, where M and M' represents the 8- and 6-coordinated metals respectively. The measured values are presented between the parenthesis.

	coordination number	δ /(mm/s)	V_{xx} (a.u)	V_{yy} (a.u)	V_{zz} (a.u)	ΔE_Q /(mm/s)
Mn@Mn_8	8 6		–0.20 +0.15	–0.20 +0.25	+0.40 –0.39	
Fe@Ni_8	8	1.26 (*1.33*)	+0.78	+0.78	–1.56	2.53 (*3.12*)
Fe@Fe_8	6	1.23 (*1.23*)	–0.57	–0.87	+1.44	2.34 (*2.62*)
	8	1.33 (*1.35*)	+0.83	+0.83	–1.66	2.69 (*3.18*)

We have introduced the basic features of Mössbauer spectroscopy in the Chapter 3, but here we extend the discussion to include the quadrupole splitting, calculated using the equations below.

$$\Delta E_Q = \frac{eQV_{ZZ}(1+\eta^2/3)^{1/2}}{2} \qquad 5.1$$

$$\eta = (V_{xx} - V_{yy})/V_{zz} \quad (0 \leq \eta \leq 1). \qquad 5.2$$

The chemically important component of this is the electric field gradient, *V*, at the nucleus (denoted EFG), which interacts with the nuclear quadruple moment (Q) to split

each Mössbauer signal into a doublet. Q can be either positive or negative, depending on whether the charge distribution at the nucleus is prolate (egg-like shape, positive Q) or oblate (disc-like, negative Q). The value of Q a fundamental property of every isotope, so the quadrupole interaction is a function of the EFG. The EFG at the nucleus is determined by the anisotropy of the electron density at the Mössbauer nucleus itself and also by the adjacent charge densities (*i.e* the bonded atoms, ligands, electrons etc), the combination of which generates a local electric field. The derivative of this field in 3 directions constitutes the EFG tensor, which is very sensitive to very small changes in local or environmental effects such as oxidation state and spin state, coordination geometry. In Cartesian space, relative to the molecular frame (or any arbitrary frame), the EFG tensor has nine components:

$$EFG = \begin{pmatrix} V_{xx} & V_{xy} & V_{xz} \\ V_{yx} & V_{yy} & V_{yz} \\ V_{zx} & V_{xx} & V_{zz} \end{pmatrix} \qquad 5.3$$

If the matrix is symmetric, $V_{uv} = V_{vu}$, with $u \in$ (x,y,z) then the matrix becomes diagonalizable

$$EFG = \begin{pmatrix} V_{XX} & 0 & 0 \\ 0 & V_{YY} & 0 \\ 0 & 0 & V_{ZZ} \end{pmatrix} \qquad 5.4$$

$$|V_{ZZ}| \geq |V_{YY}| \geq |V_{XX}|$$

$$\eta = (V_{XX} - V_{YY})/V_{ZZ}$$

The EFG tensor is traceless ($V_{XX} + V_{YY} + V_{ZZ} = 0$), and as a result the trace can be fully specified using only two parameters, V_{ZZ} and η. A positive value of V_{ZZ} means an oblate charge distribution while a negative sign indicates elongation prolate density.

The computed Mössbauer parameters in Table 5.2 reproduce the experimental data for Fe@Fe_8 (cluster 1) with encouraging accuracy: the computed isomer shift and quadrupole splittings at the 8-coordinate site are higher than the corresponding 6-coordinate site by 0.1 mm/s and 0.35 mm/s respectively compared to values of 0.12 mm/s and 0.56 mm/s from experiment. Thus, the assignments upon which the remainder of the chapter is based seem secure. Having established a mapping between experiment and theory, it is interesting to explore the origins of the different quadrupole splittings for the 8- and 6-coordinate sites. As noted above, there are in principle two important components to the EFG: (1) the anisotropy of the electron density of the metallic d orbital (*valence*) and (2) the surrounding ligand electric field (*lattice*). [38] In Fe^{II}, the valence anisotropy arises from the sixth d electron in the high-spin configuration. We have therefore computed the EFG for the isovalent manganese cluster, Mn@Mn_8 where the d^5 density is isotropic, allowing the lattice effects to dominate the EFG. The components of the EFG for Mn@Mn_8 are uniformly small, whether at the 8- or 6-coordinate site, suggesting that it is the valence contribution from the sixth d electron that dominates the properties of the Fe clusters. Making the assumption that the lattice effects are approximately constant for Mn@Mn_8 and Fe@Fe_8, we can estimate the valence contribution to the EFG in the latter by subtracting off the values of V_{xx}, V_{yy}, V_{zz} for Mn@Mn_8 (*i.e.* $V_{valence} = V_{total} - V_{lattice}$). In the case of the 8-coordinate site, the minority-spin(β) electron on the Fe is localised in the d_{z^2} orbital, which is aligned along the 4-fold symmetry axis, Figure 5.3, leading to one large negative component of $V_{valence}$($V_{zz} \sim -2.0$) and hence a large negative ΔE_Q. The electron density is isotropic in the x and y directions, leading to $V_{xx} = V_{yy} \sim 1.0$. The parameters for the 6-coordinate iron sites are less easy to interpret

because there are 8 such sites and the electrons occupy different linear combinations of the t_{2g} orbitals on these sites. However, a large positive V_{zz} and two different perpendicular components clearly reflect the fact that the Fe^{II} ions do not lie on a symmetry axis (~ 0.9, ~ –0.6).

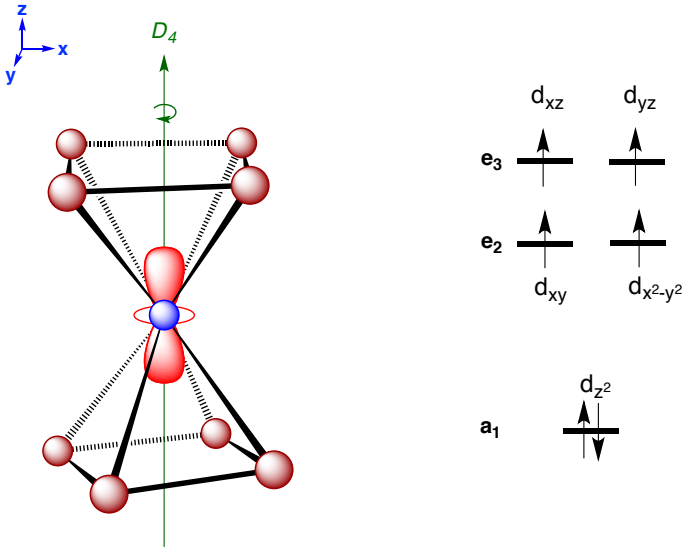


Figure 5.3: (left) $FeNi_8$ core, the brown and blue coloured balls represents Ni (6-coordinate) and Fe (8-coordinate) ions respectively, the 4-fold axis goes through the $\mathbf{d_{z^2}}$ orbital on the Fe ion. (right) The Ligand field splitting pattern of d orbitals on the central 8-coordinate metal ion.

The key experimental data relating to the site preferences are summarised in Table 5.2. The Fe/Ni ratio (left column, from X-ray fluorescence spectroscopy) and the ratio of Fe in the 8/6-coordinate sites (right column, obtained from Mössbauer spectroscopy). In the homometallic case (cluster **1**), the ratio $A_{(8)}/A_{(6)}$ of 0.11 reflects the statistical certainty that the 8- and 6-coordinate sites occur in a 1:8 ratio (1/9 = 0.11), and if the Fe ions had no site preference then the ratio would remain at 0.11 across the entire series **1**-**5**.

Table 5.2: X-ray fluorescence(XRF) and Mössbauer spectroscopy for **1-5** samples, the Fe/Ni determined by XRF. Mössbauer parameters Isomer shift, quadrupole splitting, $\mathbf{\Delta E_Q}$ and the hyperfine coupling constant $A_{(8)}/A_{(6)}$ represent the area under the peak for 8-coordinates site. The numbers between parenthesis are the estimated uncertainty of the last digit.

	XRF	**Mössbauer**				
	Fe:Ni ratio	**Doublet**	**δ (mm/s)**	**ΔE_Q (mm/s)**	**Γ (mm/s)**	**A/A_{tot}**
1	9.00:0.00	I ($Fe^{(6)}$)	1.23(1)	2.62(1)	0.36	0.90
		II ($Fe^{(8)}$)	1.35(3)	3.18(4)	0.28	0.10
2	8.0(3):1.0(3)	I ($Fe^{(6)}$)	1.24(1)	2.62(1)	0.34	0.90
		II ($Fe^{(8)}$)	1.37(3)	3.15(4)	0.22	0.10
3	2.98(8):6.02(8)	I ($Fe^{(6)}$)	1.24(1)	2.56(2)	0.32	0.78
		II ($Fe^{(8)}$)	1.36(1)	3.13(2)	0.20	0.22
4	1.54(5):7.46(5)	I ($Fe^{(6)}$)	1.22(1)	2.52(2)	0.36	0.52
		II ($Fe^{(8)}$)	1.33(1)	3.11(2)	0.24	0.48
5	1.19(3):7.81(3)	I ($Fe^{(6)}$)	1.22(2)	2.52(3)	0.34	0.34
		II ($Fe^{(8)}$)	1.33(1)	3.12(1)	0.24	0.66

In fact the ratio actually increases substantially at higher concentrations of Ni (in clusters **4** and **5** in particular), indicating that when Fe is in low abundance, it accumulates in the 8-coordinate sites. In summary, we have two key pieces of information that we seek to understand: The X-ray fluorescence spectroscopy shows that Ni accumulates in the cluster in preference to Fe and the ^{57}Fe Mössbauer spectroscopy tells us that the Fe accumulates preferentially in the 8-coordinate central site.

5.3.2 Isodesmic Reaction Analysis

As noted in the discussion of computational details, convergence difficulties have made it impossible to tackle the problem of site preference directly by comparing the energies of two isomers of the same stoichiometry (for example, $Fe@Ni_8$ and $Ni@Ni_7Fe$): the SCF of one isomer or the other always fails to converge. Instead, we tackle the problem indirectly by considering the following isodesmic reaction:

$$M@M_8 + 8M'@M'_8 \rightarrow 9M@M'_8$$

The difference between reactants and products represents the (hypothetical) energy of formation of the heterometallic cluster, $M@M'_8$ where metal M is definitely in the central 8-coordinate site and M' definitely in the 6-coordinate site, from a mixture of homometallic clusters of the same overall composition. In the latter case, the distribution of metals across the 8- and 6-coordinate sites occurs in a statistical 1:8 ratio. In this way, we require only clusters with D_4 point symmetry, where convergence has proved more tractable. A negative value for the reaction energy (as defined above) indicates that having M in the 8-coordinate site and M' in the 6-coordinate site is more favorable than the statistical average. Conversely, a positive reaction energy implies the opposite, that occupation of the 8-coordinate site by M is less favourable than the statistical average. The reaction energy, ΔE, against overall composition for the four clusters $Fe@Fe_8$, $Fe@Ni_8$, $Ni@Fe_8$ and $Ni@Ni_8$ is summarised in Figure5.4 (note that the reaction energy for homometallic clusters is necessarily zero as the reactant and the produce are identical).

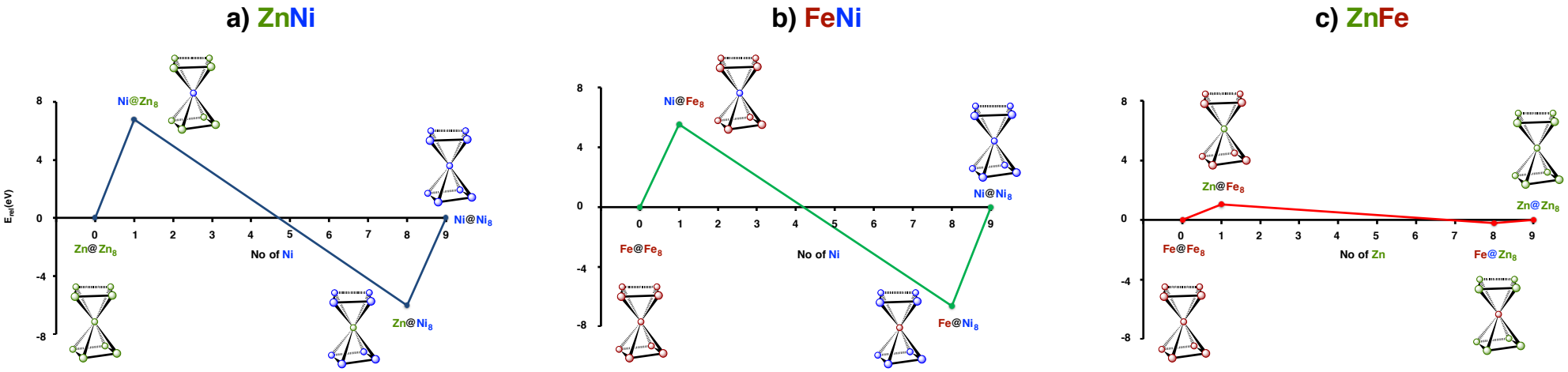


Figure 5.4: Relative energies diagrams. Each of the points on these diagrams represents the formation energy of $M@M_8 + 8M'@M'_8 \rightarrow 9M@M'_8$ reaction, e.g the $NiFe_8$ point is the energy of $Ni@Ni_8 + 8Fe@Fe_8 \rightarrow 9Ni@Fe_8$ reaction. While $Fe@Fe_8$ point refers to the homogenous reaction $Fe@Fe_8 + 8Fe@Fe_8 \rightarrow 9Fe@Fe_8$. Negative values indicate that $M@M'_8$ is more stable than the statistical average, while points above the horizontal lines indicate that $M@M'_8$ is less. The lines colours are: blue; Ni/Zn, green; Ni/Fe, red; Fe/Zn.

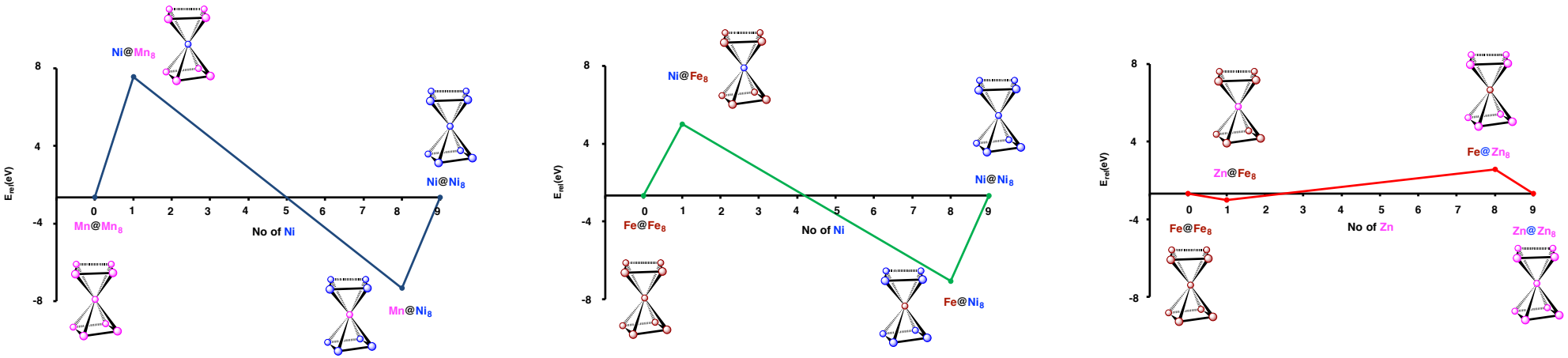


Figure 5.5: Formation reaction energies of $M@M_8 + 8M'@M'_8 \rightarrow 9M@M'_8$. Negative values indicate that $M@M'_8$ is more stable than the statistical average, while points above the horizontal lines indicate that $M@M'_8$ is less. The lines colours are: blue; Ni/Zn, green; Ni/Fe, red; Fe/Zn.

The large negative reaction energy for $Fe@Ni_8$ (–6.6 eV) and the large positive energy for $Ni@Fe_8$ (+5.5 eV) both indicate very clearly that the 8- and 6-coordinate sites are preferentially occupied by the Fe^{II} and Ni^{II} respectively, precisely as the analysis of the experimental Mössbauer peak intensities indicates. This observation does not, however, establish whether this distribution of ions is driven by the preference of Fe^{II}, the preferences of Ni^{II}, or a combination of the two. Looking closely at the geometrical configuration of the ions in both coordination sites, it seems likely that the occupancy of the 6-coordinates site is more energetically significant: the uniformly long bond lengths at the 8-coordinate site (>2.25 Å) compared to those at the 6-coordinate sites (2.0 - 2.1 Å, with the exception of those to the μ_4- bridging ligand which are relatively long) suggest that the ligand field at the octahedral site will be much stronger. This means the octahedral sites are ideally suited to a d^8 metal ion (Ni^{II}) with the potential for a substantial ligand field stabilization energy (LFSE). Typical values of the ligand-field splitting parameter, Δ_{oct}, for divalent first row transition metals with moderate- to weak-field ligands (NH_3, H_2O) are of the order of 9000 cm^{-1} (≈ 1.1 eV), giving a LFSE of $1.2 \times \Delta_{oct} \approx 1.3$ eV for a Ni^{II} ion and $0.4 \times \Delta_{oct} \approx 0.4$ eV for Fe^{II}. The isodesmic reaction $Fe@Fe_8 + 8\ Ni@Ni_8 \rightarrow 9\ Fe@Ni_8$, involves the exchange of eight Fe^{II} ions for eight Ni^{II} in the octahedral sites, giving an approximate estimate for ΔE of $8 \times (-1.3 + 0.4) = -7.2$ eV. This compares favourably with the computed value of –7.4 eV in Figure 5.5(a), indicating that the magnitude of ΔE is broadly consistent with the hypothesis that the greater LFSE available to Ni^{II} is the dominant factor in determining the site preferences. To further test this hypothesis, we have performed two parallel series of calculations, where either of the two ions, Fe or Ni, is replaced by a ligand-field neutral Zn^{II} (d^{10}) cation (Figure 5.4a and c, respectively). The most important

feature is that the Ni/Zn series is almost superimposed on that for the original Ni/Fe series while on the other hand the Fe/Zn series (red line) is very different, with reaction energies close to zero. These observations show that the 6- and 8-coordinate sites do not effectively differentiate Fe^{II} from Zn^{II}, and therefore that the electronic properties of Fe are not main factor controlling the Ni/Fe allocation over the two sites. In contrast, Ni^{II} and Zn^{II} are strongly differentiated, and it is the former ion that controls the observed chemistry. The corresponding plots where another ligand-field-neutral ion, Mn^{II}, is used in place of Zn^{II} tell a very similar story, with a negative energy for $Mn@Ni_8$ and positive energy for $Ni@Mn_8$. The value of –7.0 eV for the former is substantially lower than that for $Zn@Ni_8$ (–6.0eV), probably because the Mn^{II} ion is larger than Zn^{II}, and therefore binds more strongly in the 8-coordinate site where the bond lengths are long. Ultimately, the isodesmic reaction energies summarised in Figures 5.4 and 5.5 show conclusively that Fe^{II} does preferentially enter the 8-coordinate sites, as observed experimentally, but also that the preference is driven by the strong ligand field stabilization of the Ni^{II} ions in the octahedral sites. The Fe^{II} ions, in contrast, have no significant site preference and simply fill the sites left vacant once the available Ni^{II} ions have been accommodated in their preferred sites.

5.4 Conclusions

Five enneanuclear clusters, with different Ni/Fe ratios, have been synthesised and studied by our collaborators using a combination of Mössbauer spectroscopy, X-ray crystallography and X-ray fluorescence (XRF) spectroscopy. XRF has established the Ni:Fe ratio in each cluster and X-ray crystallography has shown that the clusters are isostructural, but has not been able to distinguish Fe from Ni, and hence establish how the metal ions are distributed between the 6- and 8-coordinate sites of the cluster.

Mössbauer spectroscopy suggests, however, that the Fe ions tend to accumulate preferentially in the central 8-coordinate state, from which we can deduce that Ni is found in greater abundance in the 6-coordinate sites. We have employed density functional theory to investigate the origin of these site preferences.

Our initial objective was to validate the assignment of the Mössbauer peaks and to explore the role of the anisotropy of the electric field from the iron d electrons on the quadrupole splitting. The calculations confirm the assignment, clearly differentiating 6- and 8-coordinate sites. The sixth (minority spin) electron on the high spin Fe^{II} ion is responsible for the anisotropy, and when Fe occupies the 8-coordinate site there is a clear correlation between the identity of the doubly occupied d orbital (d_{z^2}, aligned along the 4-fold axis) and the electric field gradient tensor, which is also axially symmetric.

Our second objective was to explore the origins of the site preferences. SCF convergence problems frustrated all attempts to make a direct comparison of two isomers of a given composition, so we consider instead isodesmic reactions $M@M_8 + 8M'@M'_8 \rightarrow 9M@M'_8$. The large negative and positive energies for $Fe@Fe_8 + 8Ni@Ni_8 \rightarrow 9Fe@Ni_8$ and $Ni@Ni_8 + 8Fe@Fe_8 \rightarrow 9Ni@Fe_8$ respectively, confirm the preference of Fe and Ni for the 8- and 6-coordinate sites, respectively, but this data alone does not allow us to identify which of the two ions dominates the trend. Isovalent substitution with either Zn^{II} or Mn^{II} (both ligand-field neutral) shows conclusively that it is the Ni^{II} that plays the dominant role, the ligand-field stabilisation of the d^8 configuration providing a strong preference for octahedral coordination. The emphasis of the experimental data is firmly on Fe rather than Ni simply because it is the distribution of Fe that we can measure directly via Mössbauer spectroscopy: we are effectively blind

to the Ni ions, and can only infer their position by assuming that they occupy the sites that Fe does not. Nevertheless, it becomes clear from our analysis that the Fe^{II} ions are largely spectators in the coordination chemistry: they simply fill all the remaining vacancies in the cluster after the much more selective Ni^{II} ions have taken up their preferred positions in the octahedral sites.

5.5 References

[1] A. N. Georgopoulou, K. Al-Ameed, A. Boudalis, D. F. Anagnostopoulos, V. Psycharis, J. E. McGrady, Y. Sanakis and C. P. Raptopoulou, *Dalton Transactions* **2017**, *46*, 12835-12844.

[2] C. Jiang, *Acta Materialia* **2007**, *55*, 4799-4806.

[3] C. Jiang and B. Gleeson, *Scripta Materialia* **2006**, *55*, 433-436.

[4] D. M. P. Mingos and L. Zhenyang, *Comments on Inorganic Chemistry* **1989**, *9*, 95-122.

[5] A. R. Rossi and R. Hoffmann, *Inorganic Chemistry* **1975**, *14*, 365-374.

[6] Y. Wang, H. Su, L. Ren, S. Malola, S. Lin, B. K. Teo, H. Häkkinen and N. Zheng, *Angewandte Chemie International Edition* **2016**, *55*, 15152-15156.

[7] Y. Umena, K. Kawakami, J. R. Shen and N. Kamiya, *Nature* **2011**, *473*, 55-65.

[8] Y. Hu and M. W. Ribbe, *Coordination Chemistry Reviews* **2011**, *255*, 1218-1224.

[9] M. Capdevila, R. Bofill, O. Palacios and S. Atrian, *Coordination Chemistry Reviews* **2012**, *256*, 46-62.

[10] Y. Montet, P. Amara, A. Volbeda, X. Vernede, E. C. Hatchikian, M. J. Field, M. Frey and J. C. FontecillaCamps, *Nature Structural Biology* **1997**, *4*, 523-526.

[11] L. K. Blusch, O. Mitevski, V. Martin-Diaconescu, K. Propper, S. DeBeer, S. Dechert and F. Meyer, *Inorganic Chemistry* **2014**, *53*, 7876-7885.

[12] B. Das, H. Daver, A. Singh, R. Singh, M. Haukka, S. Demeshko, F. Meyer, G. Lisensky, M. Jarenmark, F. Himo and E. Nordlander, *European Journal of Inorganic Chemistry* **2014**, *2014*, 2204-2212.

[13] E. V. Eames, R. H. Sanchez and T. A. Betley, *Inorganic Chemistry* **2013**, *52*, 5006-5012.

[14] T. M. Powers, N. N. X. Gu, A. R. Fout, A. M. Baldwin, R. H. Sanchez, D. M. Alfonso, Y. S. Chen, S. L. Zheng and T. A. Betley, *Journal of the American Chemical Society* **2013**, *135*, 14448-14458.

[15] C. M. Zall, L. J. Clouston, V. G. Young, K. Y. Ding, H. J. Kim, D. Zherebetskyy, Y. S. Chen, E. Bill, L. Gagliardi and C. C. Lu, *Inorganic Chemistry* **2013**, *52*, 9216-9228.

[16] S. J. Tereniak, R. K. Carlson, L. J. Clouston, V. G. Young, E. Bill, R. Maurice, Y. S. Chen, H. J. Kim, L. Gagliardi and C. C. Lu, *Journal of the American Chemical Society* **2014**, *136*, 1842-1855.

[17] A. M. Ako, I. J. Hewitt, V. Mereacre, R. Clerac, W. Wernsdorfer, C. E. Anson and A. K. Powell, *Angewandte Chemie-International Edition* **2006**, *45*, 4926-4929.

[18] R. Bagai and G. Christou, *Chemical Society Reviews* **2009**, *38*, 1011-1026.

[19] G. Aromi and E. K. Brechin, Struct. Bonding(Berlin), **2006**, p. 1-67.

[20] C. J. Milios, A. Vinslava, W. Wernsdorfer, A. Prescimone, P. A. Wood, S. Parsons, S. P. Perlepes, G. Christou and E. K. Brechin, *Journal of the American Chemical Society* **2007**, *129*, 6547-6561.

[21] J. D. Rinehart, M. Fang, W. J. Evans and J. R. Long, *Nature Chemistry* **2011**, *3*, 538-542.

[22] R. J. Blagg, C. A. Muryn, E. J. L. McInnes, F. Tuna and R. E. P. Winpenny, *Angewandte Chemie-International Edition* **2011**, *50*, 6530-6533.

[23] Y. Z. Zheng, E. M. Pineda, M. Helliwell and R. E. P. Winpenny, *Chemistry-a European Journal* **2012**, *18*, 4161-4165.

[24] M. Affronte, A. Ghirri, S. Carretta, G. Amoretti, S. Piligkos, G. A. Timco and R. E. P. Winpenny, *Applied Physics Letters* **2004**, *84*, 3468-3470.

[25] T. C. Stamatatos, C. P. Raptopoulou, S. P. Perlepes and A. K. Boudalis, *Polyhedron* **2011**, *30*, 3026-3033.

[26] A. Tsohos, S. Dionyssopoulou, C. P. Raptopoulou, A. Terzis, E. G. Bakalbassis and S. P. Perlepes, *Angewandte Chemie-International Edition* **1999**, *38*, 983-985.

[27] G. S. Papaefstathiou, S. P. Perlepes, A. Escuer, R. Vicente, M. Font-Bardia and X. Solans, *Angewandte Chemie-International Edition* **2001**, *40*, 884-886.

[28] G. S. Papaefstathiou, A. Escuer, R. Vicente, M. Font-Bardia, X. Solans and S. P. Perlepes, *Chemical Communications* **2001**, 2414-2415.

[29] A. K. Boudalis, B. Donnadieu, V. Nastopoulos, J. M. Clemente-Juan, A. Mari, Y. Sanakis, J. P. Tuchagues and S. P. Perlepes, *Angewandte Chemie-International Edition* **2004**, *43*, 2266-2270.

[30] A. K. Boudalis, Y. Sanakis, J. M. Clemente-Juan, B. Donnadieu, V. Nastopoulos, A. Mari, Y. Coppel, J. P. Tuchagues and S. P. Perlepes, *Chemistry-a European Journal* **2008**, *14*, 2514-2526.

[31] G. S. Papaefstathiou, A. K. Boudalis, T. C. Stamatatos, C. J. Milios, C. G. Efthymiou, C. P. Raptopoulou, A. Terzis, V. Psycharis, Y. Sanakis, R. Vicente, A. Escuer, J. P. Tuchagues and S. P. Perlepes, *Polyhedron* **2007**, *26*, 2089-2094.

[32] N. C. Handy and A. J. Cohen, *Molecular Physics* **2001**, *99*, 403-412.

[33] A. 2013, *SCM, Theoretical Chemistry, Vrije Universiteit, Amsterdam, The Netherlands,* http://www.scm.com/.

[34] W. G. Han, T. Q. Liu, T. Lovell and L. Noodleman, *Journal of Computational Chemistry* **2006**, *27*, 1292-1306.

[35] J. P. Perdew, J. A. Chevary, S. H. Vosko, K. A. Jackson, M. R. Pederson, D. J. Singh and C. Fiolhais, *Physical Review B* **1992**, *46*, 6671-6687.

[36] S. H. Vosko and L. Wilk, *Physical Review B* **1980**, *22*, 3812-3815.

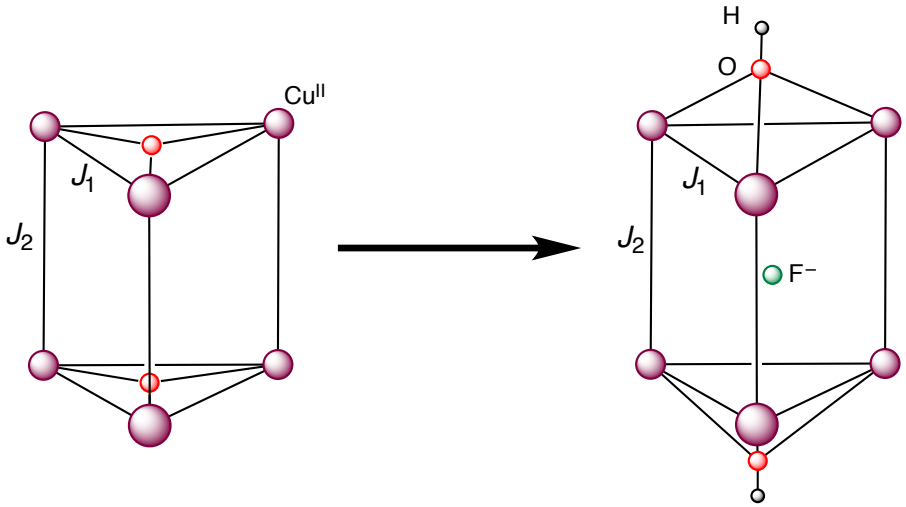
[37] A. Klamt and G. Schuurmann, *Journal of the Chemical Society-Perkin Transactions 2* **1993**, 799-805.

[38] P. Gutlich, E. Bill and A. X. Trautwein, *Mossbauer Spectroscopy and Transition Metal Chemistry Fundamentals and Applications*, Springer, Springer-Verlag Berlin Heidelberg **2011**, p. 1-539.

6

6 A Trigonal Prismatic Cu_6-pyrazolato Complex Containing a μ_6-F Ligand

The work detailed in this section has been published in Dalton Trans.[1] Raptis and co-workers synthesised a Cu_6-cage containing an endohedral fluoride ion – this compound is very similar to a number of cages that the group have studied previously,[2] except for the presence of fluoride ion trapped inside the prismatic Cu_6-cage. Our aim was to investigate the impact of the fluoride ion magnetic exchange interactions J_1 and J_2, within and between the copper triangles. The study concluded that while F^- ion has no effect on J_2, it does affect the values of J_1 by inflating the cluster and causing deviation of Cu-O-Cu bond angles from their ideal values.



6.1 Introduction to the Experimental Data

In previous work, our collaborator, Professor Raphael Raptis, succeeded in synthesizing and measuring the magnetic and electrochemical properties of {$Cu_3(\mu_3$-O)(μ-4-R-pz)$_3$}$_2$(3,5-Ph_2-4-R´-pz)$_3$,[Cu_6O_2], (Figure 6.1, [PPN] [Cu_6O_2], R = R´ = H, [PPN] = bis(triphenylphospine)iminium cation).[3] The analysis of the magnetic data of [Cu_6O_2], showed that the coupling between the two triangles, J_2, and within the triangles, J_1, was antiferromagnetic but the latter was about 15 times stronger.[2] More recently, Raptis and his co-workers explored the reaction between [Cu_6O_2] and [Fc][PF_6] and managed to isolate crystals of {$Cu_3(\mu_3$-OH)(μ-pz)$_3$}$_2$(μ-3,5-Ph_2pz)$_3$(μ_6-F),}, [Cu_6(OH)$_2$F]. This cluster is structurally similar to [Cu_6O_2] except that it contains an encapsulated (μ_6-F) fluoride ion inside the Cu_6 prism and the bridging ligand in the triangle is hydroxide instead of oxide ion (Figure 6.1).

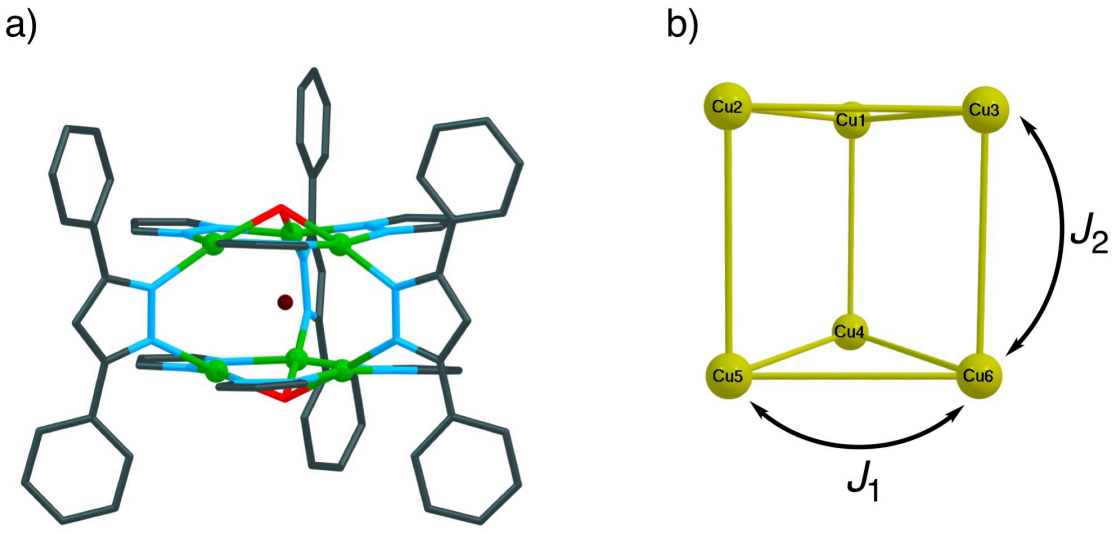


Figure 6.1: (**a**) Molecular structure of [Cu_6(OH)$_2$F]. The coloured balls are: copper; green, nitrogen; cyan, oxygen; red, flouride; purple, carbon; black. (**b**) prismatic Cu_6 cage.

The coordination of fluoride in the cluster is rather unusual: fluoride tends to form bonds with the alkali and alkaline earth metals due to their high coordination number[4-

6] and its bonding to transition metals is less common.[7-8] Cu–F bonds are generally unusual and occur mainly in compounds of Cu^{III} such as K_3CuF_6[7] and Cu^{II}–F and Cu^{III}–F in aryl fluorinating intermediates.[8] In biology, fluorides are known to couple with trinuclear copper complexes to block the process of the electron transfer in laccases. [9]

Figure 6.2 shows the temperature dependence of the effective magnetic moment, μ, and magnetization isotherms, M of $[Cu_6(OH)_2F]$. At room temperature, the effective magnetic moment is μ = 3.67 μ_B, dropping to 2.36 μ_B linearly at 50 K before decrease rapidly to 0.64μ_B at 1.9K. Considering the values of μ at 50 K, 2.36 μ_B is much lower than the theoretical value (4.24μ_B), obtained using the spin only formula with g= 2, for six coupled Cu^{II} ions, implying the presence of strong antiferromagnetic coupling. The qualitative interpretation of the magnetic moments suggests that the coupling on each μ_3-OH-Cu_3 fragment is strongly antiferromagnetic, resulting in a local state for each Cu_3 triangle S = 1/2. Weak antiferromagnetic coupling between the triangles produces two states (singlet and triplet). The effective magnetic moment for the two independent triangles with S = 1/2, estimated to be 2.45$_{\mu B}$ with g = 2, is in much better agreement with the observed μ at 50 K.

$$\begin{aligned} \mathrm{H} = &-J_1(\mathrm{S}_1.\mathrm{S}_2 + \mathrm{S}_2.\mathrm{S}_3 + \mathrm{S}_1.\mathrm{S}_3 + \mathrm{S}_4.\mathrm{S}_5 + \mathrm{S}_5.\mathrm{S}_6 + \mathrm{S}_4.\mathrm{S}_6) \\ &-J_2(\mathrm{S}_1.\mathrm{S}_4 + \mathrm{S}_2.\mathrm{S}_5 + \mathrm{S}_3.\mathrm{S}_6) + \mu_B g \sum_{i=1}^{6} \boldsymbol{B}.\boldsymbol{S}_i \\ &+d_{12}.(\mathrm{S}_1 \times \mathrm{S}_2) + \mathrm{d}_{23}.(\mathrm{S}_2 \times \mathrm{S}_3) + \mathrm{d}_{31}.(\mathrm{S}_1 \times \mathrm{S}_3) \\ &+\mathrm{d}_{45}.(\mathrm{S}_4 \times \mathrm{S}_5) + \mathrm{d}_{56}.(\mathrm{S}_5 \times \mathrm{S}_6) + \mathrm{d}_{46}.(\mathrm{S}_4 \times \mathrm{S}_6) \end{aligned} \qquad 6.1$$

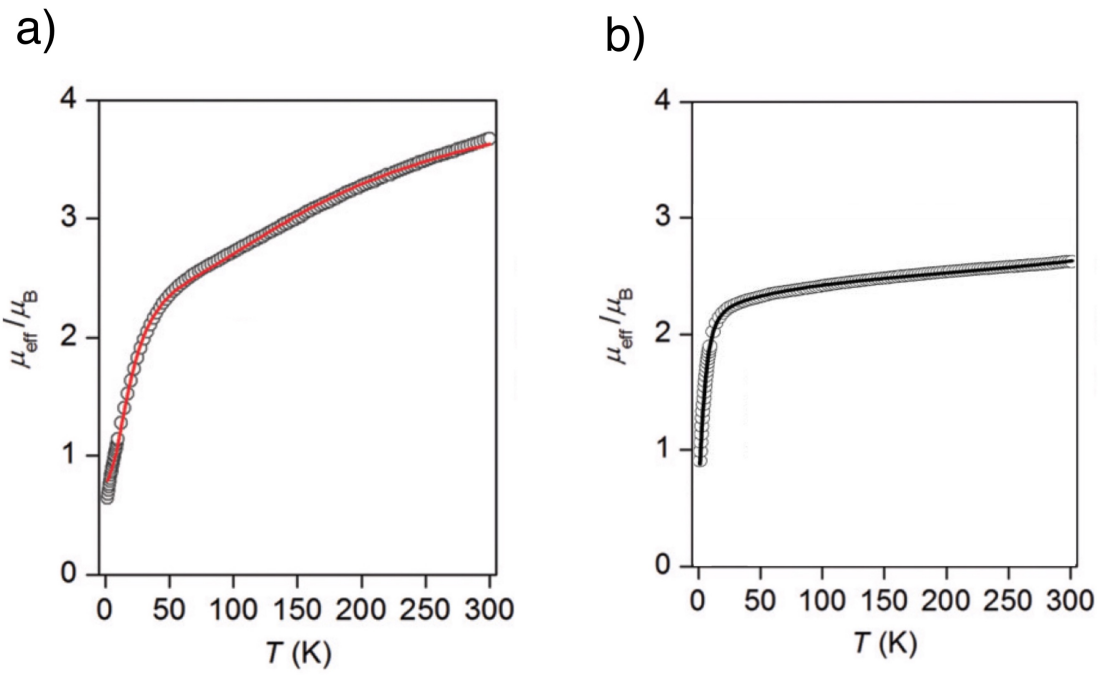


Figure 6.2: The measured plots of the temperature-dependence of effective magnetic moments: (**a**) $[Cu_6(OH)_2F]$ and (**b**) $[Cu_6O_2]$.

The magnetic data was fitted to the spin Hamiltonian in the Equation 6.1, where J_1 and J_2 represent the exchange coupling constants for intra- and inter-triangular coupling, respectively. Antisymmetric exchange $\boldsymbol{d}_{ij}$ vectors between individual pairs (S_i and S_j) were also taken into account.[10] The best-fit values for exchange coupling, obtained by fitting the magnetic data to Equation 6.1 with an isotropic $g = 2.1$(the value used for $[Cu_6O_2]$ [2]), resulted in values of $J_1 = -147$ cm^{-1}, $J_2 = -35$ cm^{-1}, and $|d_z|$ = 30.2 cm^{-1}. In comparison with the fitted parameters for $[Cu_6O_2]$ (J_1(av) = –675 cm^{-1}, J_2 = –26 cm^{-1}, g = 1.95 and $|d_z|$ = 30.0 cm^{-1}), it is clear that while J_2 and $|d_z|$ values are similar. J_1 for $[Cu_6(OH)_2F]$ is significantly reduced.

Geometrical changes in open/shell polynuclear compounds are often reflected in their isotropic coupling constants, J, such that their sign and magnitude give us key information on the topology of the magnetically interacting centres. General relationship relating structure and magnetic coupling have been established in di- and

tri-nuclear clusters, $M_2(\mu_2\text{-O})$ and $M_3(\mu_3\text{-O})$, M = Cu and Fe,[11-14] where the M-O-M angle and *J* values are linearly correlated. However, in larger clusters, simple magnetostructural relationships are not so straightforward and the use of predetermined descriptors to predict magnetic properties is a challenging task.[15] (Our purpose in this chapter is to explore the reasons for this reduction in J_1).

6.2 Computational Details

The Amsterdam density functional ADF2013 code, which uses Slater-type functions, was employed to run all the calculations in this chapter. We used the well-known hybrid DFT, B3LYP, to do the calculations for all of the structures in this report. Polarised triple and double zeta basis sets were used for Cu and the main group atoms respectively. We replaced all phenyl fragments shown in Figure 6.1a with hydrogen atoms.

The broken symmetry, BS, approach developed by Noodleman has become common to deal with these issues.[16-17] In this approach, the energy eigenvalues of the non-relativistic Kohn-Sham Hamiltonian can be mapped onto the diagonal elements of Heisenberg-Dirac-Van-Vleck (HDVV) Hamiltonian, which is expressed in Equation 6. 2.

$$H = -J_{ij} \sum_{i>j} S_i . S_j \qquad 6.\ 2$$

Where *J* is the exchange coupling between magnetic centres *i* and *j*. We run a series of single point calculations to obtain BS states starting from the HS optimised geometry. The spin pattern of the HS state was $|\alpha\alpha\alpha\alpha\alpha\alpha\rangle$ ($M_S = 3$) while the BS ones were $|\alpha\alpha\alpha\alpha\alpha\beta\rangle$ ($M_S = 2$), $|\alpha\alpha\alpha\alpha\beta\beta\rangle$ ($M_S = 1$) and $|\alpha\alpha\alpha\beta\beta\beta\rangle$ ($M_S = 0$). However, *J* values generated by this method are generally overestimated, and Ruiz and co-

workers have proposed spin unprojected approach that avoids the double counting of the non-dynamical correlation, which already has been taken into consideration in the unrestricted DFT solution.[18-19] They proposed a 'pairwise' for polymetallic species, given by Equation 6. . In this form, the computed energies are mapped on to the eigenvalues of the Heisenberg Hamiltonian, instead of the diagonal elements.

$$E_{HS} - E_{BS} = -J_{ij}(2S_iS_j + S_i) \qquad 6.3$$

6.3 Discussion

We follow the computational procedures established in the study of $[Cu_6O_2]$ [(see the computational part of more detail). The Heisenberg spin Hamiltonian used is given Equation 6. 4.

$$\mathrm{H} = -J_1(\mathrm{S}_1.\mathrm{S}_2 + \mathrm{S}_2.\mathrm{S}_3 + \mathrm{S}_1.\mathrm{S}_3 + \mathrm{S}_4.\mathrm{S}_5 + \mathrm{S}_5.\mathrm{S}_6 + \mathrm{S}_4.\mathrm{S}_6) \\ -J_2(\mathrm{S}_1.\mathrm{S}_4 + \mathrm{S}_2.\mathrm{S}_5 + \mathrm{S}_3.\mathrm{S}_6) \qquad 6.4$$

We have calculated *J* values using both the Noodleman and Ruiz formulas (Equation 6. 4 and Equation 6.3). We confirmed, that the computed J_{ij}, particularly with B3LYP, using Equation 6. 3 give good agreement with the experiment.[18, 20-25] They are also smaller by a factor of 2 than the values calculated using Equation 6. 4. The computed coupling constants J_1 and J_2 are –130 cm^{-1} and –51 cm^{-1}, respectively, which agree nicely with the fit to the experimental data –151 cm^{-1} and –47 cm^{-1}. Moreover, these *J* values are substantially lower than those reported previously for J_1 for $[Cu_6O_2]$ (calculated: J_1 = –390 cm^{-1} J_2 = –40 cm^{-1} *vs.* measured J_1 = –630 cm^{-1} J_2 = –44 cm^{-1}) [*].

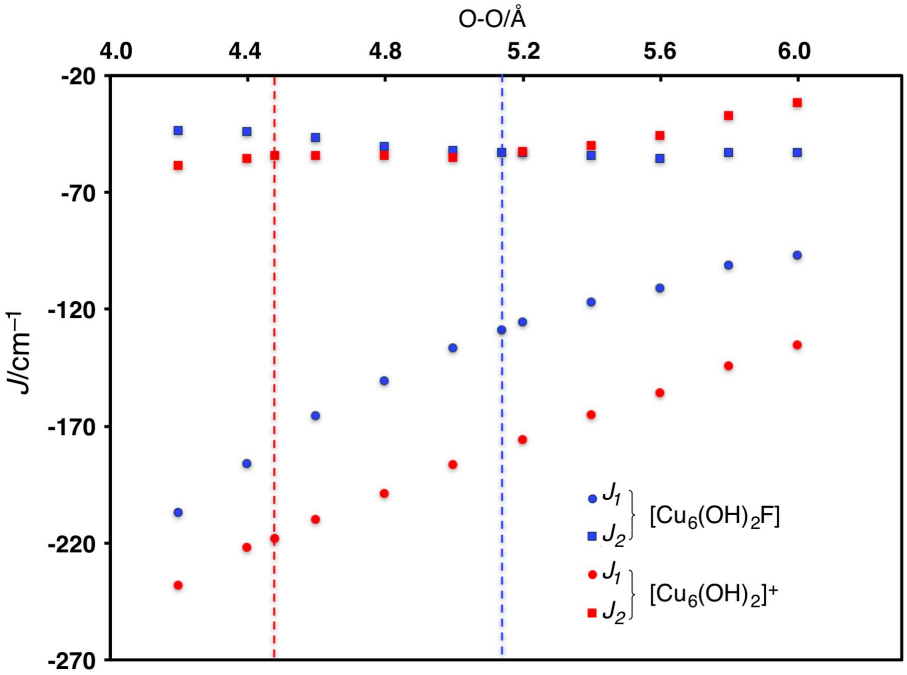


Figure 6.3: Exchange Coupling correlation showing the dependence of J_1 and J_2 on the separation between the two O centres for $[Cu_6(OH)_2F]$, and the corresponding species where the fluoride ion has been removed ($[Cu_6(OH)_2]$). Vertical lines show the optimised O–O separations with (5.14 Å) and without (4.48 Å) fluoride ion.

So what, then, is the origin of the very different J_1 values in $[Cu_6O_2]$ and $[Cu_6(OH)_2F]$? It seems unlikely that the presence of a fluoride ion in the middle of the copper prism opens up new pathways to couple the two triangles directly since the F–Cu vectors are orthogonal to the magnetic orbitals of Cu ($d_{x^2-y^2}$ in the local coordinate system). Nevertheless, removing the fluoride, without allowing the structure to relax, changes the coupling constants J_1 and J_2 to –146 cm^{-1} and –71 cm^{-1}, respectively: J_1 in particular is substantially reduced in magnitude (Figure 6.3). When the fluoride free structure is allowed to relax, the O–O distance is reduced from 5.14 Å to 4.48 Å (dashed lines), corresponding to reduction in the distance between the Cu_3 planes.

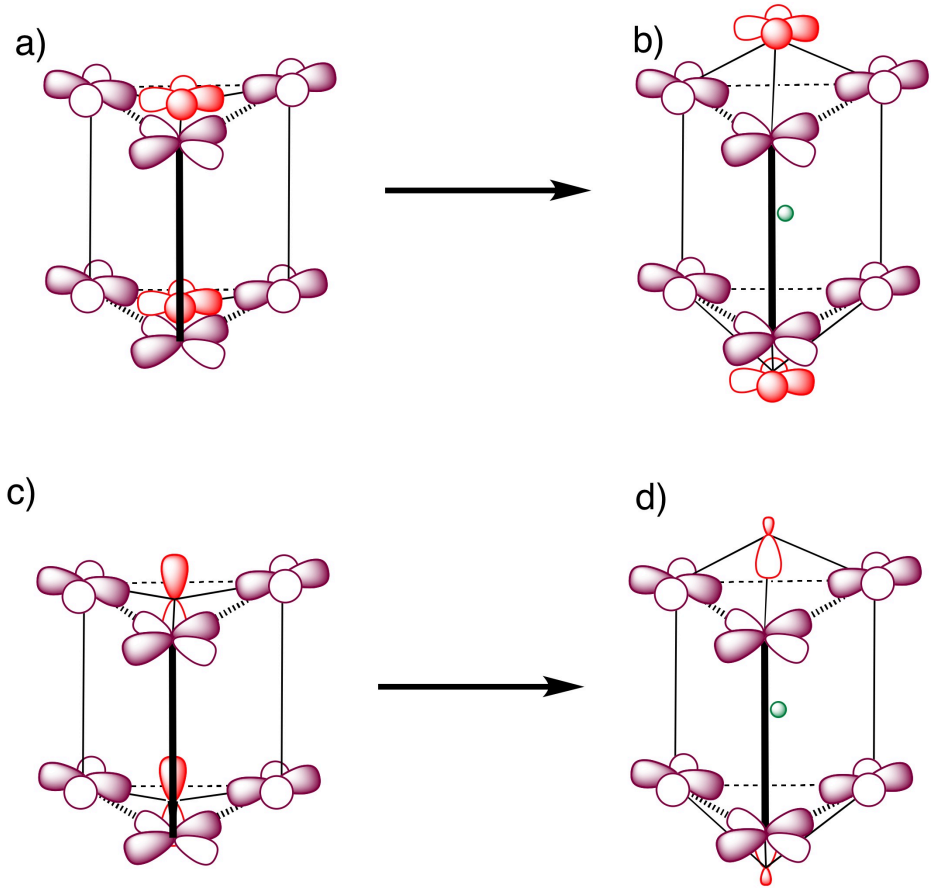


Figure 6.4: Magnetic orbitals $\boldsymbol{d_{x^2-y^2}}$ of the metals and $\boldsymbol{p}$ orbitals of the oxygen atom. (a) and (b) show the interaction of copper $\boldsymbol{d_{x^2-y^2}}$ orbital with the $\boldsymbol{p_x}$ and $\boldsymbol{p_y}$ of the oxygen in $[Cu_6O_2]$ and $[Cu_6(OH)_6F]$ respectively, while (c) and (d) shows the contributions of the oxygenic $\boldsymbol{p_z}$ in the same interactions.

This has been the further increasing in the magnitude of antiferromagnetic J_1 to ~ –220 cm^{-1}, thus, the value of J_1 is directly correlated with the planarity of the Cu_3 rings, and so the primary role of the fluoride is to repel the μ_3-hydroxyl groups out of the Cu_3 plane, enhancing the pyramidality at each triangle. As the $Cu_3(\mu_3\text{-OH})$ triangles become more planar the, oxygen p orbitals and copper magnetic orbitals overlap more effectively (Figure 6.4).

Reducing J_1 is clearly due to the axial deformation of the planar triangles to the pyramidal configuration.[1] However, the inter-triangle coupling, J_2, seems unaffected by the Cu-O-Cu angle changes. The recalculated eigenvalues of the spin Hamiltonian

using the coupling constant J_1 and J_2 values appropriate to $[Cu_6(OH)_6F]$ (J_1 = –150 cm^{-1} and J_2 = –30 cm^{-1}) and $[Cu_6O_2]$ (J_1 = –600 cm^{-1} and J_2 = –30 cm^{-1}) complexes are shown Figure 6.5c and d respectively. The eigenvalue spectrum can be understood if we consider first, the effect of the large J_1 in each triangle (Figure 6.5a). This splits the 2^3 = 8 configuration into a quintet and 2 degenerate doublets, the spectrum between them being 3*J*. If we then couple the *S* =1/2 states of the 2 triangles (2*J*), we get near quadruply-degenerate singlets and triples. Likewise, coupling of two 3/2 triplets states gives states with *S* = 3 ,2, 1 and 0. In the limit that $J_1>>J_2$, these state lie in 6 J_1 above the ground state. Finally, coupling of ½ on one triangle with *S* = 3/2 on the other will give near-degenerate states with S = 2 and *S* = 1. In the limit of $J_1>>J_2$, these states will lie on $3J_1$ above the ground state.

If J_1 is large, only the levels *S* = 0/*S* = 1 manifold are populated even at 300 K, and so the plateau happens at 2.4 MB. The experiment is therefore insensitive to the J_1, because we cannot accurately place the *S* =1,2 manifold at $3J_1$. For J_1= –150, in contrast, there is plateau around 2.4 for T<100 K but then μ starts to rise due to population of the *S* = 1 and *S* = 2 states which now lie at 500 cm^{-1} (Figure 6.5c) (*vs.* 1700 cm^{-1} for J_1= –650 cm^{-1} (Figure 6.5d)). Therefore, the rise in the μ in the range 100<T<300 is apparent in the experimental plot allow us to accurately plane the *S* = 1 and 2 states, and so determine J_1. If we reduce J_1 to –30 cm^{-1}, Figure 6.5b, the entire manifold of states collapses to a narrow band, and the value of μ approaches the spin-only value for six independent *S* = 1/2 centres of 4.24 μ_B.

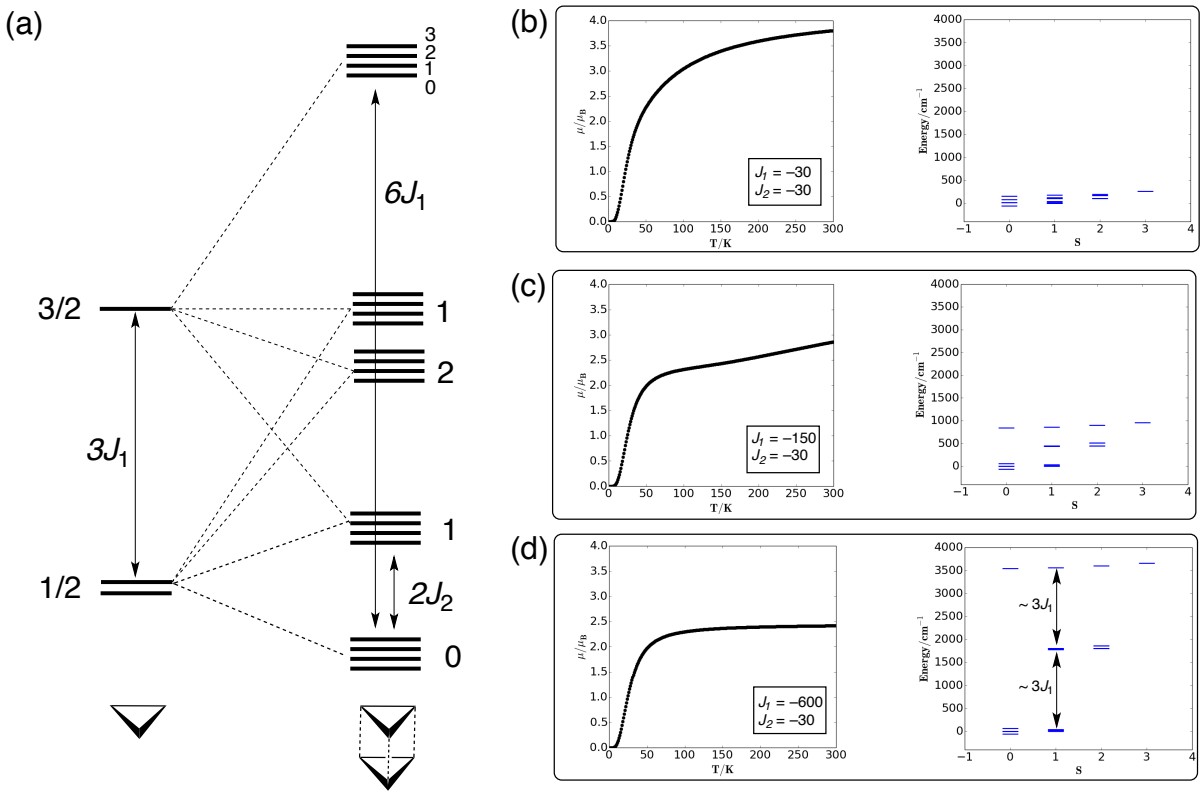


Figure 6.5: (a) the energy levels for single and two coupled Cu^{II}_3 triangles. (b, c, d) the computed magnetic moments with their corresponding eigenvalues spectra.

6.4 Conclusions

Cu_6 prismatic cage has been synthesised by our collaborators (Professor Raphael Raptis group), similar to the $[Cu_6O_2]$ cluster studies previously, except that it contains fluoride ion trapped in the middle and the two capped oxygens are replaced by hydroxides. Our computed coupling constants confirm that coupling between the metal ions is antiferromagnetic, consistent with the experimental data.

The fluoride ion has no direct effect on the inter-triangular coupling. but, presence of the negative charged fluoride results in expansion of the distance between the hydroxyl groups, reduced planarity of the $Cu_3(OH)$ triangle and so to a noticeable decrease in intra-triangular magnetic coupling J_1.

6.5 Appendix: Spin Hamiltonian Code:

In order to reconstruct the magnetic functions from computed *J* values, we have written a python code that generate the energy levels, their spin state and their corresponding eigenvectors based on spin only(isotropic) spin Hamiltonian. The spin Hamiltonian for such system is

$$H_{iso} = -2J\hat{S}_1.\hat{S}_2$$

The code works as follows:

1. Input: the parameters that are required to construct the wavefunction
    a. List of the magnetic pairs
    b. *J* value of each pair (or any identical list of pairs)
    c. The spin quantum number, *S*, for each paramagnetic centre
    d. Number of paramagnetic centres in the system

The code generates all possible configurations, in case of systems with identical spin, *S*, on each centre, there would be all the possible configuration will be for such systems $S' = (2S_{Tot} + 1)^N$ such configuration, where *N* is number of the paramagnetic centres. For our example, where N = 2 and $S_{Tot} = 1$ ($S = \frac{1}{2}$ for each metal ion) $\psi_1 = \left|\frac{1}{2}, \frac{1}{2}\right\rangle$; $\psi_2 = \left|-\frac{1}{2}, -\frac{1}{2}\right\rangle$; $\psi_3 = \left|\frac{1}{2}, -\frac{1}{2}\right\rangle$; $\psi_4 = \left|-\frac{1}{2}, \frac{1}{2}\right\rangle$.

2. The second step is the construction of the matrix elements, for example.

$$\langle\psi_1|-2J\widehat{S_1}.\widehat{S_2}|\psi_1\rangle = \left\langle\frac{1}{2}, \frac{1}{2}\right|-2J\left(\hat{S}_{x1}.\hat{S}_{x2} + \hat{S}_{y1}.\hat{S}_{y2} + \hat{S}_{z1}.\hat{S}_{z2}\right)\left|\frac{1}{2}, \frac{1}{2}\right\rangle$$

$$= -2J\left\langle\frac{1}{2}, \frac{1}{2}\right|\hat{S}_{x1}.\hat{S}_{x2} + \hat{S}_{y1}.\hat{S}_{y2}\left|\frac{1}{2}, \frac{1}{2}\right\rangle - 2J\left\langle\frac{1}{2}, \frac{1}{2}\right|\hat{S}_{z1}.\hat{S}_{z2}\left|\frac{1}{2}, \frac{1}{2}\right\rangle$$

$$= -J\left\langle\frac{1}{2}, \frac{1}{2}\right|\hat{S}_{1+}.\hat{S}_{2-} + \hat{S}_{-}.\hat{S}_{+}\left|\frac{1}{2}, \frac{1}{2}\right\rangle - 2J\left\langle\frac{1}{2}, \frac{1}{2}\right|\hat{S}_{z1}.\hat{S}_{z2}\left|\frac{1}{2}, \frac{1}{2}\right\rangle$$

$$= 0 - 2(\frac{1}{2}.\frac{1}{2})J = -\frac{J}{2}$$

where

$$\hat{S}_z \left|\pm\tfrac{1}{2}\right\rangle = \pm\tfrac{1}{2}\left|\pm\tfrac{1}{2}\right\rangle$$
$$\hat{S}_\pm \left|\pm\tfrac{1}{2}\right\rangle = A_\pm \left|\tfrac{1}{2}\pm 1\right\rangle$$
$$A_\pm = \sqrt{s(s+1) - m_s(m_s \pm 1)}$$

3. The result of the spin Hamiltonian matrix is the following

$$\begin{array}{c|cccc} & |\psi_1\rangle & |\psi_2\rangle & |\psi_3\rangle & |\psi_4\rangle \\ \hline \langle\psi_1| & -\frac{J}{2} - E & 0 & 0 & 0 \\ \langle\psi_2| & 0 & -\frac{J}{2} - E & 0 & 0 \\ \langle\psi_3| & 0 & 0 & -\frac{J}{2} - E & -J \\ \langle\psi_4| & 0 & 0 & -J & -\frac{J}{2} - E \end{array}$$

4. Diagonalization of the matrix yield the eigenvalues and eigenvectors. The code not only matches each of these eigenvalues to their corresponding m_s values, but also categorises them to their corresponding spin quantum numbers (S).
5. The last stage involves the insertion of values of M_S and their corresponding eigenvalues into Van Vleck's equation to calculate and plot the magnetic susceptibility (and therefore the magnetic moment on range of temperature).

$$\chi_M = \frac{N\beta^2 g^2}{3kT} \frac{\sum_S S'(S'+1)(2S'+1)(E^1_{S'} - E^2_{S'})\exp\left(-\frac{\mathrm{E}^0_\mathrm{n}}{kT}\right)}{\sum_S S'(S'+1)(2S'+1)\exp\left(-\frac{\mathrm{E}^0_\mathrm{n}}{kT}\right)}$$

Figure 6.6: shows a flow chart that the summarises of the code algorithm:

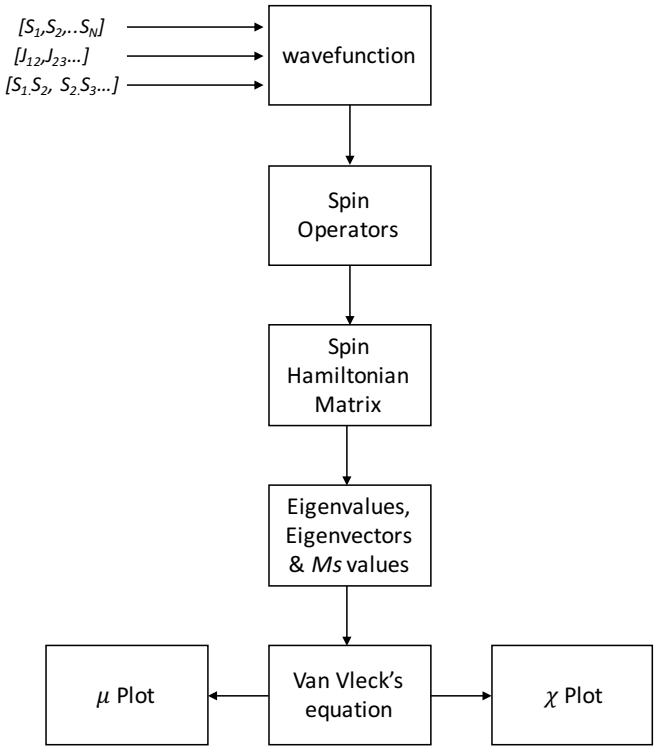


Figure 6.6: the main steps of the spin Hamiltonian code.

6.6 References

[1] L. Mathivathanan, K. Al-Ameed, K. Lazarou, Z. Travnicek, Y. Sanakis, R. Herchel, J. E. McGrady and R. G. Raptis, *Dalton Transactions* **2015**, *44*, 20685-20691.

[2] E. M. Zueva, M. M. Petrova, R. Herchel, Z. Travnicek, R. G. Raptis, L. Mathivathanan and J. E. McGrady, *Dalton Transactions* **2009**, 5924-5932.

[3] G. Mezei, M. Rivera-Carrillo and R. G. Raptis, *Dalton Transactions* **2007**, 37-40.

[4] S. Wuttke, A. Lehmann, G. Scholz, M. Feist, A. Dimitrov, S. I. Troyanov and E. Kemnitz, *Dalton Transactions* **2009**, 4729-4734.

[5] C. Knapp, E. Lork, P. G. Watson and R. Mews, *Inorganic Chemistry* **2002**, *41*, 2014-2025.

[6] F. Q. Liu, A. Kuhn, R. Herbstirmer, D. Stalke and H. W. Roesky, *Angewandte Chemie-International Edition in English* **1994**, *33*, 555-556.

[7] T. V. Popova and N. V. Aksenova, *Russian Journal of Coordination Chemistry* **2003**, *29*, 743-765.

[8] Y. D. Ye, S. D. Schimler, P. S. Hanley and M. S. Sanford, *Journal of the American Chemical Society* **2013**, *135*, 16292-16295.

[9] K. P. Kepp, *Inorganic Chemistry* **2015**, *54*, 476-483.

[10] R. Boca and R. Herchel, *Coordination Chemistry Reviews* **2010**, *254*, 2973-3025.

[11] C. Canada-Vilalta, T. A. O'Brien, E. K. Brechin, M. Pink, E. R. Davidson and G. Christou, *Inorganic Chemistry* **2004**, *43*, 5505-5521.

[12] S. M. Gorun and S. J. Lippard, *Journal of the American Chemical Society* **1985**, *107*, 4568-4570.

[13] S. M. Gorun, G. C. Papaefthymiou, R. B. Frankel and S. J. Lippard, *Journal of the American Chemical Society* **1987**, *109*, 4244-4255.

[14] A. Riisio, M. M. Hanninen and R. Sillanpaa, *European Journal of Inorganic Chemistry* **2012**, 1048-1053.

[15] E. Ruiz, *Principles and Applications of Density in Inorganic Chemistry Ii* **2004**, *113*, 71-102.

[16] L. Noodleman, *Journal of Chemical Physics* **1981**, *74*, 5737-5743.

[17] L. Noodleman and E. R. Davidson, *Chemical Physics* **1986**, *109*, 131-143.

[18] E. Ruiz, J. Cano, S. Alvarez and P. Alemany, *Journal of Computational Chemistry* **1999**, *20*, 1391-1400.

[19] E. Ruiz, J. Cano, S. Alvarez, A. Caneschi and D. Gatteschi, *Journal of the American Chemical Society* **2003**, *125*, 6791-6794.

[20] E. Ruiz, P. Alemany, S. Alvarez and J. Cano, *Journal of the American Chemical Society* **1997**, *119*, 1297-1303.

[21] E. Ruiz, P. Alemany, S. Alvarez and J. Cano, *Inorganic Chemistry* **1997**, *36*, 3683-3688.

[22] E. Ruiz, J. Cano, S. Alvarez and P. Alemany, *Journal of the American Chemical Society* **1998**, *120*, 11122-11129.

[23] E. Ruiz, C. de Graaf, P. Alemany and S. Alvarez, *Journal of Physical Chemistry A* **2002**, *106*, 4938-4941.

[24] A. Rodriguez-Fortea, P. Alemany, S. Alvarez and E. Ruiz, *European Journal of Inorganic Chemistry* **2004**, 143-153.

[25] E. Ruiz, S. Alvarez, J. Cano and V. Polo, *Journal of Chemical Physics* **2005**, *123*.

---

[*] Our calculated J_1 value for structure 1 smaller than what was reported in the previous papers where the calculations have been done by Gaussian functions.